

Evaluation, Improvement and Development of Density-Functional
Tight-Binding Parameters for Simulations of Materials

(物質のシミュレーションのための密度汎関数強結合法のパラメータ
の評価、改良および開発)

Aulia Sukma Hutama

Table of Contents

Table of Contents.....	ii
Chapter 1 General Introductions	1
Chapter 2 Theoretical Background	6
2.1 Basic principles of quantum chemical calculation	6
2.1.1 The Schrödinger equation	6
2.1.2 Born-Oppenheimer approximation	8
2.2 Overview of <i>ab initio</i> wave function methods to solve Schrödinger wave equation.....	9
2.3 Density Functional Theory	10
2.3.1 Hohenberg-Kohn theorems	10
2.3.2 Kohn-Sham equation.....	12
2.3.3 Exchange-correlation functional	13
2.4 Density-Functional Tight-Binding	17
2.4.1 Tight-binding method	17
2.4.2 Second order DFTB (DFTB2)	18
2.4.3 Improvement of DFTB	22
2.4.3.1 Spin-polarized DFTB	22
2.4.3.2 Third order DFTB (DFTB3)	23
2.4.3.3 Long-range corrected DFTB (LC-DFTB).....	24
2.4.4 Parameterization in DFTB	25
2.4.4.1 Introduction to DFTB parameters	25
2.4.4.2 Currently available DFTB2 parameters	31

**Chapter 3 Coupled Cluster and Density Functional Studies of Atomic Fluorine
Chemisorption on Coronene as Model Systems for Graphene Fluorination.....34**

3.1	Introduction	34
3.2	Computational methodology	36
3.3	Results and discussion.....	40
3.3.1	PEC scans at the B3LYP/cc-pVDZ level of theory	40
3.3.2	B3LYP/cc-pVDZ optimized geometries.....	42
3.3.3	Single point energies along the partially frozen PEC obtained with various DFT and WFT methods.	47
3.3.4	Spin-polarized vs spin-unpolarized DFTB calculations.	53
3.3.5	Origin of the incorrect dissociation limit in pure, hybrid, and approximate DFT methods.	54
3.3.6	Potential energy curves from DFTB+ <i>U</i> calculations.....	58
3.3.7	Fitting C–F repulsive potential from the potential energy curves	60
3.4	Summary	67

**Chapter 4 Density Functional Studies of Atomic Oxygen and Nitrogen Interactions
with Coronene as Model for Graphene Functionalization70**

4.1	Introduction	70
4.2	Computational details and model systems	71
4.3	Results and discussions	74
4.3.1	Oxygen adsorption on coronene computed at B3LYP/cc-pVDZ level of theory	74
4.3.2	PBE and DFTB2 calculations of the interactions of oxygen with coronene	79
4.3.3	Interactions of atomic nitrogen and coronene computed at various DFT levels of theory ..	83
4.3.4	Interaction energies on the dissociation limit of the coronene-O and coronene-N PECs....	86

4.4	Summary	90
Chapter 5	Long-Range and Short-Range Zr–Zr DFTB2 Repulsive Potential for Interaction in Bulk Zirconium	92
5.1	Introduction	92
5.2	Parameterization procedures and computational details	92
5.3	Results and Discussions	97
5.3.1	DFT testing set	97
5.3.2	DFTB2 results	101
5.3.2.1	Polynomial fitted repulsive potential	101
5.3.2.2	PSO repulsive potentials	107
5.4	Discussions	117
5.5	Summary	119
Chapter 6	Summary and Outlook.....	121
References.....		123
Appendix.....		138
A	Zr electronic parameters	138
Acknowledgements		140
List of Publications		141

Chapter 1 General Introductions

In general terms, theoretical chemistry is a branch of chemistry that attempts to give explanations of the phenomena that occur in chemical experiments. Along with the development of chemical science, theoretical chemistry in modern days is required to observe and explain chemical systems and phenomena at the atomic or molecular level, since the properties of matter at the atomic or molecular level are not directly observable through experiments in the laboratory. Additionally, by studying the matter at atomic and molecular level, one can predict the properties of materials at macroscopic level for further understanding and application of materials. Developments of good theoretical methods thus become necessary to study the properties of matter at the atomic and molecular level.

The development of modern quantum mechanics in the early 20th century, including the Schrödinger equation [1] and Dirac's theory of electron [2] has allowed the application of quantum mechanics (QM) to the chemical systems; as such those methods were applicable for predicting chemical properties elucidated from atomistic level. The quantum mechanical role here is the treatment of the electron in the chemical system explicitly where we know that atoms and molecules contain particles known as "electron". Many people coined the combination of QM and chemistry as "quantum chemistry".

However, the enduring challenge of quantum chemistry is the fact that the Schrödinger equation, which governs electronic structure dynamics and properties, cannot be solved readily. This equation can only be solved analytically for the hydrogen atom or hydrogen like ions that contain only one electron. For atoms and molecules that have more than one electron, this equation is analytically nearly impossible to solve. This leads to a number of approximations to date that tries to approximate the exact solution of the

Schrodinger equation for many electron systems, such as the Hartree-Fock method.

In the earliest days of theoretical and quantum chemistry, approximate solutions to the Schrödinger equation had to be obtained using paper and pencil, with only little help from manual calculators, since the computational resources were not sufficiently available at that time. As the time went by, the rapid development of computational resources became apparent. Nowadays, many chemical or physics systems can be modeled *in silico* via computer codes that are programmed using the algorithms and theories from multidisciplinary fields such as mathematics, physics, chemistry and computer science. However, although the computers speed grows exponentially over time [3], increasing number of atoms or electrons in systems do not scale proportionally to the computational time.

Time scale

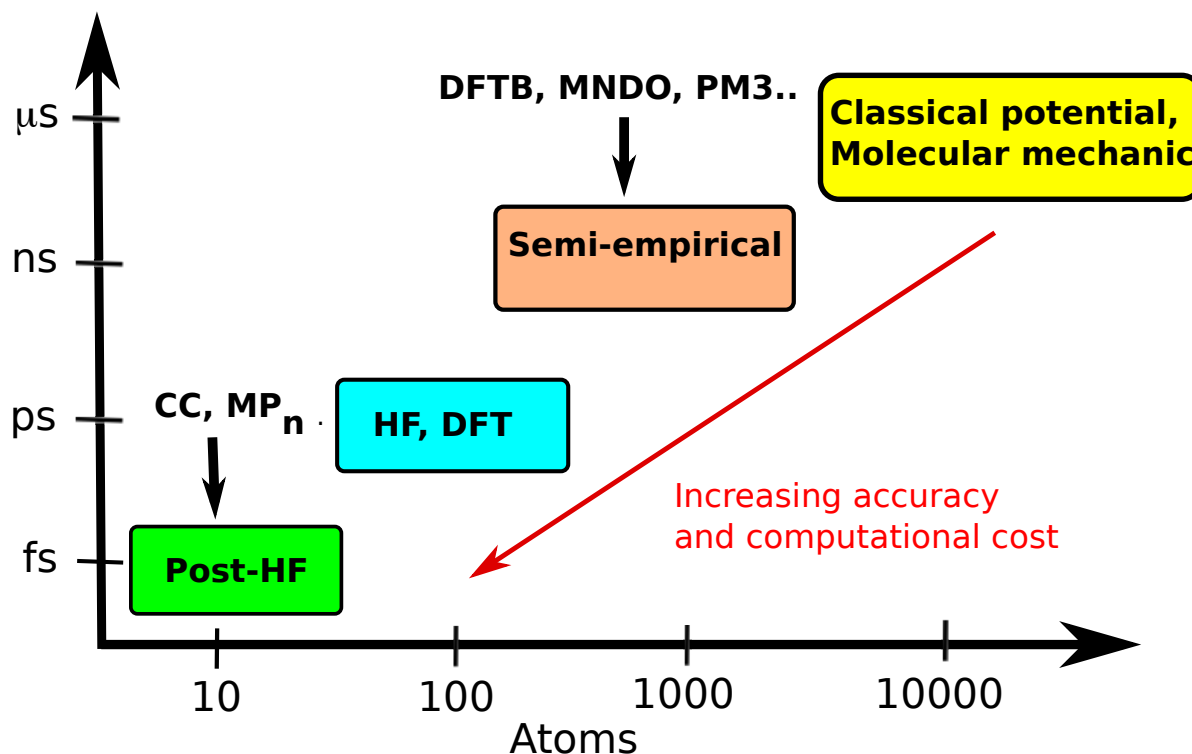


Figure 1.1 Scheme of methods in computational chemistry.

The method for computer simulation is usually chosen to have affordable

computational cost while retaining the accuracy of the simulation methods. Methods for computer simulation trade-off between the simulation timescale and system size is shown in Figure 1.1. Empirical methods with fitted potentials, such as the molecular mechanics (MM) method, can treat chemical systems on the scale of up to 10^{10} atoms. A drawback of that method is that the electronic interactions are not explicitly included in the potentials; therefore some properties involving changes in electronic structure such as bond breaking events cannot be described using the MM method. On the other hand, electronic structure methods such as density functional theory (DFT) have become the standard workhorse in computational chemistry or material science, but suffer from limitation of the system size. The computational time of DFT scales approximately cubic with the number of electrons in the systems, limiting computational time for research communities with medium sized computational facility.

One particular method, the so-called density-functional tight-binding DFTB [4–6] method, bridges the gap between classical MM and DFT-type electronic structure theory. It allows longer simulations time and larger, more adequate model systems for simulation of nanometer-sized clusters with QM treatment of electrons. However, since DFTB is also a semi-empirical method, it requires parameterization of intermolecular interactions.

The main motivation of the current project is to develop DFTB parameters that have not been reported thus far in the literature. Additionally, some existing parameters may lack universal transferability; therefore, they should be tuned based on our needs. Our main goal is to use the parameter sets reported in this thesis for simulation of interesting and useful materials.

Among those useful materials are graphene [7] and solid oxide-fuel cells

(SOFCs) [8]. In this work, we developed the DFTB parameters for the purpose of simulation of oxide transport in SOFCs and the functionalizing of graphene. Zirconia (ZrO_2) is one of the most important oxide materials with a wide range of applications. The bulk phase is commonly used for refractory and structural materials [9], while surface applications such as support material for catalysis [10] are increasing rapidly. A prominent use of zirconia is in the field of energy conversion, where it is typically doped with around 8% of yttria (Y_2O_3) to form yttria-stabilized zirconia (YSZ) and used as the oxide-ion conducting electrolyte in SOFCs [8,11]. Our interest in graphene functionalization comes from its zero band gap (Figure 1.2(a)), and the functionalization of graphene, for example using F atom, will open the graphene band gap, (Figure 1.2(b)) allowing it for electronic materials applications.

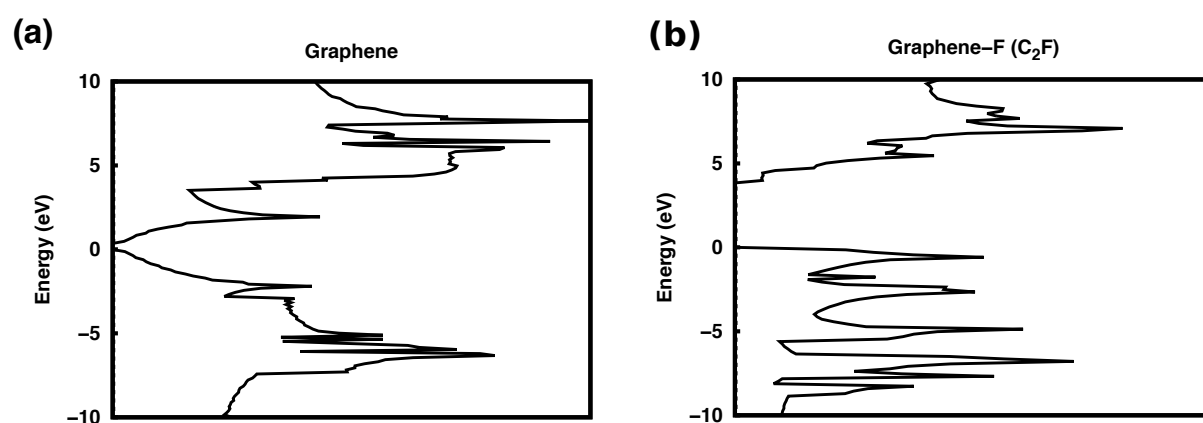


Figure 1.2 Calculated density of states (DOS) at Perdew-Burke-Ernezhoff (PBE) level of theory of (a) graphene and (b) graphene-F with F/C ratio of 50%. The Fermi level is shifted to zero.

The first part of this thesis reports the results from established electronic structure theory such as DFT and coupled cluster (CC) theory as well as DFTB with already published parameters. The results of these calculations will be used as the reference for the development and possible improvement of the DFTB parameters. In this part, we do not only use the calculations as the DFTB reference data but also we established some results that has not been reported before, such as the self-interaction effects on F atom adsorption on

graphene model (Chapter 3), a possible mechanism of O atom adsorption and migration on graphene model and potential energy curve of N atom adsorption on graphene model (Chapter 4).

The second part (Chapter 5) of this thesis reports the development of repulsive potentials for materials simulations. Here, we report the early stage of the development of the DFTB parameters for simulation of YSZ-based SOFCs materials. In this chapter, a number Zr – Zr repulsive parameterization schemes are reported.

Finally, general conclusions and future prospects are presented in Chapter 6.

Chapter 2 Theoretical Background

This chapter will provide explanation about the methods used in this thesis.

2.1 Basic principles of quantum chemical calculation

Quantum chemical calculation is based mainly on the Schrödinger equation and Born-Oppenheimer approximation.

2.1.1 The Schrödinger equation

The underlying postulate of quantum mechanics is contained in the Schrödinger wave equation, formulated as,

$$i \frac{\partial \Psi(\mathbf{r}, t)}{\partial t} = \hat{H} \Psi(\mathbf{r}, t) \quad (2.1).$$

\hat{H} is the Hamiltonian operator that is composed of two components, the kinetic and potential energy operator. Kinetic energy operator is defined as $-\frac{1}{2m} \nabla^2$ and potential energy operator is the potential function of the position and time of $V(\mathbf{r}, t)$. The variables \mathbf{r} and t denote position and time, respectively. Eq. (2.1) can be written into,

$$i \frac{\partial \Psi(\mathbf{r}, t)}{\partial t} = \left(-\frac{1}{2m} \nabla^2 + V(\mathbf{r}, t) \right) \Psi(\mathbf{r}, t) \quad (2.2).$$

The equation, known as time-dependent Schrödinger equation, is a general equation for the various systems. The operand, $\Psi(\mathbf{r}, t)$ is called wave function, which is a solution of the Schrödinger equation. Physically, $\Psi(\mathbf{r}, t)$ is meaningless, however Ψ contains all of the information contained in the system is represented by the function the wave and by Max Born interpretation, the square gives the probability to find particle at certain position.

By the quantum mechanics postulates, the wave function must satisfy these conditions.

1. The wave function must have a finite value since the wave function describe the

probability of a particle at a certain range.

2. The wave function must be single-valued, because it is not possible that a particle have 2 different existences in the same space and time.
3. The wave function must be continuous and differentiable for all orders

Although time-dependent Schrödinger equation is general and applicable for any system-containing particle, many systems do not contain time variables upon observation. In such case, the Schrödinger equation can be formulated into a time-independent Schrödinger equation as follows,

$$E\Psi(\mathbf{r}) = \hat{H}\Psi(\mathbf{r}) \quad (2.3)$$

or

$$E\Psi(\mathbf{r}) = \left(-\frac{1}{2m}\nabla^2 + V(\mathbf{r})\right)\Psi(\mathbf{r}) \quad (2.4)$$

with \mathbf{r} is the spatial coordinate in the space for the particle(s) and E is the total energy for the system. In linear algebra terminology, time-independent Schrödinger equation is an eigenvalue problem where the term E is the eigenvalue and $\Psi(\mathbf{r})$ is the eigenvector.

For the application in chemical systems for atoms or molecules, in general there are 5 contributions of energy in the Hamiltonian, namely: the kinetic energy of the electrons; the kinetic energy of the nuclei; the nuclei and electrons Coulomb attractive potential energy; the electron-electron Coulomb repulsive potential energy of the electron-electron; and the nucleus-nucleus Coulomb repulsive potential. In such, with the systems containing N number of electrons and Q number the Hamiltonian can be written as

$$\hat{H} = -\sum_{n=1}^N \frac{1}{2} \nabla_n^2 - \sum_{q=1}^Q \frac{1}{2M_q} \nabla_q^2 - \sum_{n=1}^N \sum_{q=1}^Q \frac{Z_q}{r_{nq}} + \sum_{n < m=1}^N \frac{1}{r_{nm}} + \sum_{q < r=1}^Q \frac{Z_q Z_r}{R_{qr}} \quad (2.5)$$

with subscripts n, m are the indices for the electrons; q, r are the indices for the nuclei. From

Eq. (2.5), the first, third and fourth term on the right-hand side can be specified as electronic Hamiltonian i.e.

$$\hat{H}_e = - \sum_{n=1}^N \frac{1}{2} \nabla_n^2 - \sum_{n=1}^N \sum_{q=1}^Q \frac{Z_q}{r_{nq}} + \sum_{n < m=1}^N \frac{1}{r_{nm}} \quad (2.6)$$

while the second term on the right-hand side can be considered as nuclear kinetic energy operator \hat{T}_N and fifth term on the right-hand side can be considered as the nuclear potential energy operator \hat{V}_N . Therefore the total Hamiltonian can be separated into electronic and nuclear contribution

$$\hat{H} = \hat{H}_e + \hat{T}_N + \hat{V}_N \quad (2.7)$$

and Schrödinger equation can be written as,

$$E(\mathbf{R}, \mathbf{r})\Psi(\mathbf{R}, \mathbf{r}) = (\hat{H}_e + \hat{T}_N + \hat{V}_N)\Psi(\mathbf{R}, \mathbf{r}) \quad (2.8).$$

In this case, the wave function and energy is a function of the position of the electrons, \mathbf{r} and the nuclei positions, \mathbf{R} . The classification for this electron and nucleus contribution will be the basis foundation of Born-Oppenheimer approximation that will be explained in the next section.

2.1.2 Born-Oppenheimer approximation

Born-Oppenheimer approximation is based on the fact that there is high ratio between the mass of the nucleus and the mass of the electron, which is about two thousand to one in an example case of hydrogen atom. This has the consequence that the movements of electrons are much faster compared to the nucleus. With this assumption, electrons are considered to move in the fixed nuclei and the movements of nuclei are considered to be zero. This assumption has consequence that $\hat{T}_N = 0$. This will lead the Schrödinger equation to be

$$E(\mathbf{R}, \mathbf{r})\Psi(\mathbf{R}, \mathbf{r}) = (\hat{H}_e + \hat{V}_N)\Psi(\mathbf{R}, \mathbf{r}) \quad (2.9).$$

2.2 Overview of *ab initio* wave function methods to solve Schrödinger wave equation

Due to the nature complexity of the Schrödinger equation, it can only be solved analytically for hydrogen or hydrogen-like atom that only contain one electron since the electron-electron interactions (fourth term on the right-hand side in Eq. (2.5)) have no definite solution with current mathematical method. With this condition, people developed methods to make the approximation of Schrödinger equation solution for many-electron systems. A number of approximated methods are available to the date to solve the Schrödinger equation for extended systems.

One of the established methods is known as Hartree-Fock (HF) method. In HF method, the ground state of electronic wave function can be expressed in the single Slater determinant satisfying the Pauli principle for N -number of electron basis function

$$\Psi = |\varphi_1(\mathbf{r}_1)\varphi_2(\mathbf{r}_2)\cdots\varphi_N(\mathbf{r}_N)| \quad (2.10).$$

By solving the Hartree-Fock equation obtained through variational principle, (see ref. [12] for the derivation and total equation) the best wave function can be obtained. The HF method assumes that the electrons move in mean field created by other electrons, hence the solution of Hartree-Fock equation can only be solved iteratively in self-consistent field manner. The advantage of HF is that many-electron system problems can be reduced to set of one-electron problems that are solvable for real systems. However, one drawback for HF is the lacks of electron correlations. The HF methods account for about 99% of the total energy. The electron correlation contributes the remaining 1%, which is important for chemical and physical properties of a system.

Several methods were developed after HF to overcome the problem in HF. These

methods, called post-HF basically calculate the electron correlation contribution e.g. via perturbation theory such as n -th order Møller-Plesset perturbation theory (MPn) [13], additional of more Slater determinants such as configuration interaction (CI) [14] and constructing exponential operator for the many-electron wave function (coupled cluster, CC) [15]. While the performances of these methods are satisfactory to describe geometric and energetic properties within chemical accuracy, they demanded more computational effort with increasing number of electron i.e., the scaling is $O(n^4)$ for HF, $O(n^5)$ for second order Moller-Pesset perturbation theory (MP₂) and $O(n^7)$ for coupled cluster with singly, doubly and noniterative triple excitation (CCSD(T)) with number of atomic basis function n , hence the usages of their method are not beyond geometry optimization with less than a hundred of electrons. With this situation, one can use the density functional theory as described in the next section for calculation of extended systems (large molecule, solid state systems, etc.).

2.3 Density Functional Theory

Density functional theory (DFT) is a formalism of Schrödinger equation which is based on the density $\rho(\mathbf{r})$. The density itself is a function of the vector position \mathbf{r} , which is interpreted as the probability for finding electron at \mathbf{r} , from normalized wave function $\Psi(\mathbf{r})$

$$\rho(\mathbf{r}) = |\Psi(\mathbf{r})|^2 = \Psi^*(\mathbf{r})\Psi(\mathbf{r}) \quad (2.11).$$

The asterisk indicates complex conjugate. The integration of density with respect to spatial coordinate will yield the total number of electron N , that is

$$\int \rho(\mathbf{r})d\mathbf{r} = N \quad (2.12).$$

2.3.1 Hohenberg-Kohn theorems

DFT formulation is based on theorems proposed by Kohn and Hohenberg (HK) [16] that will not be proved here. The first theorem, called existence theorem, stated

that there is a unique correspondence between the electronic density of the ground state and potential. The consequence is that the expectation value of the energy is a unique functional form ground state electronic density (Eq (2.13)).

$$\langle E \rangle = \langle \Psi^* | \hat{H} | \Psi \rangle \equiv \int a(\mathbf{r}) \rho(\mathbf{r}) d\mathbf{r} = a[\rho] \quad (2.13)$$

The second HK theorem is called variational theorem. This theorem states that there is only one function of the density $\rho(\mathbf{r})$ which will minimize $E[\rho]$ at corresponding potential. From the HK theorems, one can write total ground-state energy, $E_0[\rho]$ of an N -electron system under an external potential $V_{ext}(\mathbf{r})$

$$E_0[\rho] = T[\rho] + \int V_{ext}(\mathbf{r}) \rho(\mathbf{r}) d\mathbf{r} + J[\rho] + E_{NC}[\rho] \quad (2.14).$$

The first term on the right-hand side in Eq. (2.14), $T[\rho]$ is the kinetic energy of N -interacting electron gas. The classical Coulomb energy, $J[\rho]$, has the form

$$J[\rho] = \frac{1}{2} \int \int \frac{\rho(\mathbf{r}) \rho(\mathbf{r}')}{|\mathbf{r} - \mathbf{r}'|} d\mathbf{r} d\mathbf{r}' \quad (2.15)$$

and the $E_{NC}[\rho]$ term is the non-classical electron-electron interaction energy. Since only $V_{ext}(\mathbf{r})$ that depends on the system, we can write the total energy with the term of universal functional

$$E_0[\rho] = \int V_{ext}(\mathbf{r}) \rho(\mathbf{r}) d\mathbf{r} + F_{HK}[\rho] \quad (2.16)$$

where $F_{HK}[\rho]$ is a universal functional of electron density

$$F_{HK}[\rho] = T[\rho] + \int V_{ext}(\mathbf{r}) \rho(\mathbf{r}) d\mathbf{r} + J[\rho] + E_{NC}[\rho] \quad (2.17).$$

One of the issues connecting the DFT is that nobody knows the exact functional form $F_{HK}[\rho]$, especially the $T[\rho]$ and $E_{NC}[\rho]$ term. Many approximations for the functional have been proposed, however the accuracy for the applications in chemistry is not

sufficient. In the modern day application of DFT, we use the method proposed by Kohn-Sham that will be explained in the next section.

2.3.2 Kohn-Sham equation

In the aforementioned section, the problem is that we do not know the exact form of the universal functional. Kohn and Sham proposed a novel procedure in their seminal 1965 paper [17]. They first suggested that electron density $\rho(\mathbf{r})$ could be defined as normalized Kohn-Sham orbital $\Phi_i(\mathbf{r})$, that is

$$\rho(\mathbf{r}) = \sum_{i=1}^N |\Phi_i(\mathbf{r})|^2 \quad (2.18).$$

The basic foundation of Kohn-Sham theory is that the N -electron system can be described in an N non-interacting electron system with the Hamiltonian

$$\hat{H}_{KS} = \hat{T}_s + \hat{V}_{KS} \quad (2.19)$$

with \hat{T}_s is the non-interacting kinetic energy (first term on the right-hand side of Eq. (2.5)) and \hat{V}_{KS} is the so-called Kohn-Sham potential. From the first HK theorem we obtain

$$E_{KS}[\rho] = T_s[\rho] + \int V_{KS}(\mathbf{r})\rho(\mathbf{r})d\mathbf{r} \quad (2.20).$$

In order to derive the Kohn-Sham potential, we turn to an N interacting electron system with the external potential $V_{ext}(\mathbf{r})$. The total energy is therefore is written in Eq. (2.14). By adding and subtracting the right hand side of Eq. (2.14), with $T_s[\rho]$ we obtain

$$E_0[\rho] = T_s[\rho] + T[\rho] + \int V_{ext}(\mathbf{r})\rho(\mathbf{r})d\mathbf{r} + J[\rho] + E_{NC}[\rho] - T_s[\rho] \quad (2.21)$$

which we introduce the definition of exchange-correlation energy $E_{XC}[\rho]$ as

$$E_{XC}[\rho] = T[\rho] + E_{NC}[\rho] - T_s[\rho] \quad (2.22).$$

Since the optimal density ρ_0 defined by (from second HK theorem)

$$\delta E_0[\rho]|_{\rho=\rho_0} = 0 \quad (2.23)$$

is non-interacting v-representable, we also have a unique potential $V_{KS}(\mathbf{r})$ with

$$\delta E_{KS}[\rho]|_{\rho=\rho_0} = 0 \quad (2.24).$$

Therefore, by comparing the result, we can rewrite the Kohn-Sham potential as

$$V_{KS}(\mathbf{r}) = V_{ext}(\mathbf{r}) + \int \frac{\rho_0(\mathbf{r}')}{|\mathbf{r} - \mathbf{r}'|} d\mathbf{r}' + V_{XC}[\rho_0](\mathbf{r}) \quad (2.25)$$

with

$$V_{XC}[\rho_0](\mathbf{r}) = \frac{\delta E_{XC}[\rho]}{\delta \rho(\mathbf{r})} \quad (2.26).$$

From the variational principle with the constraint that Kohn-Sham orbitals are orthogonal, i.e.

$$\int \Phi_i^*(\mathbf{r}) \Phi_j(\mathbf{r}) d\mathbf{r}' = \delta_{ij} \quad (2.27)$$

we obtain the Kohn-Sham equation

$$\left[-\frac{1}{2} \nabla^2 + V_{ext}(\mathbf{r}) + \int \frac{\rho_0(\mathbf{r}')}{|\mathbf{r} - \mathbf{r}'|} d\mathbf{r}' + V_{XC}[\rho_0](\mathbf{r}) \right] \Phi_i(\mathbf{r}) = \varepsilon_i \Phi_i(\mathbf{r}) \quad (2.28)$$

where ε_i is a Lagrange multiplier from condition described in Eq. (2.28), or in physical meaning, ε_i is an orbital energy from Kohn-Sham orbital Φ_i . Like HF theory, the Kohn-Sham potential depends on the solution of Kohn-Sham equation. Therefore, the Kohn-Sham equation also has to be solved iteratively like solving Fock equation.

2.3.3 Exchange-correlation functional

The Kohn-Sham equation and the total energy DFT equation still leave us the unknown terms $E_{XC}[\rho]$ and $V_{XC}[\rho](\mathbf{r})$, albeit have already been defined, due to non-classical interpretation of those terms. Approximating the best exchange-correlation is the main challenge in DFT for few decades. Here, we make a brief review of the common DFT exchange-correlation functional available in the literature.

The first approximation is called local density approximation (LDA), which is the

simplest approximation. The considered approximation here is that the exchange-correlation energy at the point \mathbf{r} equals to the exchange-correlation energy of the homogenous electron gas that has uniform density at the point \mathbf{r} . The formulation of LDA exchange-correlation can be expressed as

$$E_{XC}^{LDA}[\rho] = \int \epsilon_{XC}[\rho(\mathbf{r})]\rho(\mathbf{r})d\mathbf{r} \quad (2.29)$$

where $\epsilon_{XC}[\rho(\mathbf{r})]$ is a exchange-correlation function of the density. In the last equation, it is assumed that the exchange-correlation energy density is pure local, which is the exchange-correlation namesake. The $\epsilon_{XC}[\rho(\mathbf{r})]$ can be separated linearly into contribution of exchange and correlation linearly

$$\epsilon_{XC}[\rho(\mathbf{r})] = \epsilon_X[\rho(\mathbf{r})] + \epsilon_C[\rho(\mathbf{r})] \quad (2.30).$$

While the exchange term $\epsilon_X[\rho(\mathbf{r})]$ can take the form from homogenous electron gas [18]

$$\epsilon_X[\rho(\mathbf{r})] = -\frac{3}{4}\left(\frac{3}{\pi}\rho\right)^{1/3} \quad (2.31)$$

the exact form of the correlation energy $\epsilon_C[\rho(\mathbf{r})]$ is not figured out. Some approximations that were parameterized based on the Quantum-Monte-Carlo calculations including Vosko-Wisk-Nursair (VWN) [19], Perdew-Zunger (PZ) [20] and Perdew-Wang (PW92). The performances of LDA, especially for geometry and vibrational frequency are usually good. However, LDA is known for problem for some energetic properties, such as overestimation of binding energy and underestimation of reaction barrier.

Since LDA ignores the inhomogeneity of the density, it is possible to extend the exchange-correlation functional by inclusion of the gradient of the density. The second exchange-correlation approximation is generalized gradient approximation (GGA), which is derived by this concept. GGA exchange correlation functional is written as

$$E_{XC}^{GGA}[\rho] = \int \epsilon_{XC}[\rho(\mathbf{r}), \nabla\rho(\mathbf{r})]\rho(\mathbf{r})d\mathbf{r} \quad (2.32).$$

Probably most widely used GGA exchange-correlation functional is combination between exchange functional of Becke 88 [21] with correlation functional of either Lee-Yang-Parr (LYP) [22] or Perdew 86 (P86) [23] as well as the standalone exchange-correlation functional of Perdew-Burke-Ernzerhof (PBE) [24,25]. Inclusion of the density gradient in general leads to better energetic properties compared to LDA while keeping similar accuracy with LDA for geometry.

Another approximation for the exchange-correlation functional is to mix the HF exchange part with a certain portion of DFT exchange or correlation. One of the most popular hybrid functionals is the B3LYP [22,26]. The exchange-correlation energy of B3LYP has the form

$$E_{XC}^{B3LYP} = (1 - a)E_X^{LDA} + aE_X^{HF} + bE_X^{B88} + cE_C^{LYP} + (1 - c)E_C^{LDA} \quad (2.33)$$

with $a=0.20$, $b=0.72$ and $c=0.81$. B3LYP combines the exact HF exchange with LDA (typically VWN) [19] exchange and correlation energy, Becke 88 [21] exchange energy and LYP correlation energy [22]. This hybrid functional demonstrates outstanding performance for prediction of important properties of small organic molecules.

The LDA and GGA functionals, often called local or semilocal functionals show good performance for the ground state properties. However, they fail some kinds of properties, like the underestimation of HOMO-LUMO gap and underestimation of reaction barrier. This failure is attributed to the so called self-interaction error (SIE), also known as delocalization error [27]. The SIE can be removed by eliminating the SIE orbital by orbital, suggested by Perdew *et al.* [20]. However, this approach requires higher computational cost. The other way to remove the SIE in DFT calculations while maintaining its Hartree-Fock-like

computational cost and scaling behavior is the use of range-separated functionals [28,29]. In such methods, usually termed LC-DFT, the Coulomb operator in the exchange functional is divided into short-range and long-range contributions, which are smoothly connected by using a switching function, $\zeta(r)$ as follows

$$\frac{1}{r_{12}} = \frac{\zeta(\omega r_{12})}{r_{12}} + \frac{1 - \zeta(\omega r_{12})}{r_{12}} \quad (2.34)$$

The first and second terms on the right-hand side are the contribution to short-range and long-range interactions, respectively. Switching function, $\zeta(\omega r_{12})$, can take the form of either error function, $1 - \text{erf}(\omega r_{12})$, or exponential function $\exp(-\omega r_{12})$. The ω term in the switching function is the weight of mixing of HF exchange part and r_{12} is the interelectronic distance. The short-range term is the contribution from DFT exchange and the long-range term is the contribution from HF exchange. The range-separated exchange-correlation energy can then be written as

$$E_{XC}^{RS-DFT} = E_X^{SR-DFT} + E_X^{LR-HF} + E_C^{DFT} \quad (2.35).$$

With E_X^{SR-DFT} and E_X^{LR-HF} are the DFT and HF exchange energy that already included their respective range-separated operator. Some exchange-correlation functional of this class are LC- ω PBE [29,30], LC-BLYP [21,22,31] and CAM-B3LYP [32], that has slightly different form

$$E_{XC}^{CAM-B3LYP} = [1 - (\alpha + \beta)]E_X^{B88} + \alpha E_X^{HF} + \beta(E_X^{SR-B88} + E_X^{LR-HF}) + E_C^{B3LYP} \quad (2.36).$$

With the optimized parameter $\alpha = 0.19$ and $\beta = 0.49$.

The choice of exchange-correlation functional is up to the user for what of system and properties he/she wants to examine. For finite molecular system, one tends to use hybrid functional since it has excellent geometry and energy description performance. However, pure DFT exchange-correlation functionals are more preferred for periodic solid-state

systems since calculation of Hartree-Fock exchange is more computationally expensive in periodic solid-state systems. The range-separated DFT is notoriously useful for the calculations of systems on excited states or systems with high delocalized state, like in conjugated polymers. The successful applications of DFT for modeling from molecules to materials have grown rapidly in nearly five decades. This is proven by how Walter Kohn was awarded with Nobel Prize in Chemistry in 1998, which is for his discovery of DFT.

2.4 Density-Functional Tight-Binding

Albeit the successful application of DFT for modeling materials, it still has the drawback, especially of community that would like to perform large-scale quantum mechanics based molecular dynamic simulation (QM/MD). While high accurate and efficient QM/MD method based on DFT such as Car-Parrinello MD (CPMD) [33] is available, this method also has limitation for the size of systems; hence it is not fully applicable for the extended systems either with long time simulation. Frauenheim *et al.* developed the method that mimics DFT methods with much less computational effort. This method is called density-functional tight-binding (DFTB) [4,5], which is the central method that is used in present work. The following sections are devoted to give the explanation of this method.

2.4.1 Tight-binding method

Before getting further to the DFTB, we first briefly discuss the tight-binding method as the framework of the DFTB. In tight-binding method, atoms are considered to be isolated; therefore the electrons are not considered to delocalize other than the neutral atom they should belong to. The electronic wave function can be written as the linear combination of pseudoatomic orbital ϕ_μ

$$\Psi_i = \sum_{\mu} c_{i\mu} \phi_{\mu}(\mathbf{r} - \mathbf{R}_{\alpha}) \quad (2.37)$$

where \mathbf{R}_{α} is the position of the center of orbital μ . The total energy of tight-binding method is

$$E^{TB} = \sum_i \varepsilon_i + \frac{1}{2} \sum_{\alpha, \beta} V^{rep}(\mathbf{R}_{\alpha} - \mathbf{R}_{\beta}) \quad (2.38).$$

ε_i is the eigenvalue of the orbital Ψ_i obtained by solving the secular equation

$$|\mathbf{H} - \varepsilon \mathbf{S}| = 0 \quad (2.39)$$

where the elements of Hamiltonian matrix \mathbf{H} and overlap matrix \mathbf{S} are

$$H_{\mu\nu} = \langle \phi_{\mu} | \hat{H} | \phi_{\nu} \rangle, \quad (2.40)$$

$$S_{\mu\nu} = \langle \phi_{\mu} | \phi_{\nu} \rangle$$

with

$$\hat{H} = \left[-\frac{1}{2} \nabla^2 + V(\mathbf{r}) \right] \quad (2.41).$$

Note that the $V(\mathbf{r})$ term is arbitrary potential that is usually fitted to some experimental quantity. The second term on the right-hand side of Eq. (2.38), $V^{rep}(\mathbf{R}_{\alpha} - \mathbf{R}_{\beta})$, is the short range distance dependent repulsive potential between atom α and β . In order to determine the total tight-binding energy, the Hamiltonian matrices, the overlap matrices and the repulsive potential need to be determined. In the semi-empirical TB, they are usually determined by fitting to some experimental quantity. A more precise tight binding approximation can be parameterized from DFT.

2.4.2 Second order DFTB (DFTB2)

DFTB takes the approximation of total DFT energy using the density fluctuation $\delta\rho(\mathbf{r})$ around reference density $\rho_0(\mathbf{r})$ i.e.,

$$\rho(\mathbf{r}) = \rho_0(\mathbf{r}) + \delta\rho(\mathbf{r}) \quad (2.42)$$

Substitution of Eq. (2.42) to DFT total energy and expansion via Taylor series leads to

$$\begin{aligned}
E[\rho_0(\mathbf{r}) + \delta\rho(\mathbf{r})] &= \sum_i^{occ} n_i \int \Psi_i^*(\mathbf{r}) \left[-\frac{1}{2}\nabla^2 + V_{ne} + \int \frac{\rho_0(\mathbf{r}')}{|\mathbf{r} - \mathbf{r}'|} d\mathbf{r}' + \mathbf{v}_{xc}[\rho_0(\mathbf{r})] \right] \Psi_i(\mathbf{r}) d\mathbf{r} \\
&\quad - \frac{1}{2} \iint \frac{\rho_0(\mathbf{r})\rho_0(\mathbf{r}')}{|\mathbf{r} - \mathbf{r}'|} d\mathbf{r}d\mathbf{r}' - \int \mathbf{v}_{xc}[\rho_0(\mathbf{r})] \rho_0(\mathbf{r}) d\mathbf{r} + \mathbf{E}_{xc}[\rho_0(\mathbf{r})] + E_{nn} \\
&\quad + \frac{1}{2} \iint \left[\frac{1}{|\mathbf{r} - \mathbf{r}'|} + \frac{\partial^2 \mathbf{E}_{xc}[\rho(\mathbf{r})]}{\partial \rho(\mathbf{r}) \partial \rho(\mathbf{r}')} \Big|_{\rho_0(\mathbf{r}), \rho_0(\mathbf{r}')} \right] \delta\rho(\mathbf{r}) \delta\rho(\mathbf{r}') + \dots \quad (2.43)
\end{aligned}$$

with V_{ne} and E_{nn} refer to attractive electron-nuclei and repulsive nuclei-nuclei Coloumb interaction, respectively. The first line of Eq. (2.43) is the zeroth order term E_0 defined as band structure energy E_{BS} , the second line is defined as repulsive energy E_{rep} and the third line is the second-order expansion of total energy with respect to charge fluctuation. This term is often called self-consistent charge (SCC) energy E_{SCC} . Band structure and SCC energy are often classified as DFTB electronic energy. By the definition of the energies, Eq. (2.43) can be rewritten as

$$\begin{aligned}
E^{DFTB2} &= E_0 + E_{rep} + E_2 \\
&= E_{BS} + E_{rep} + E_{SCC} \\
&= \sum_i^{occ} n_i \varepsilon_i + E_{rep} + \frac{1}{2} \sum_{\alpha\beta}^N \gamma_{\alpha\beta} \Delta q_\alpha \Delta q_\beta \quad (2.44).
\end{aligned}$$

From Eq. (2.44), the first term on the r.h.s. is the summation of orbital energy ε_i over all occupied orbital Ψ_i . E_{rep} term accounts for the core-core interaction and contribution from exchange-correlation energy and other contributions in the form of a set of distance dependent pairwise potential $V_{\alpha\beta}^{rep}(\mathbf{R}_{\alpha\beta})$, that is

$$E_{rep} = \frac{1}{2} \sum_{\alpha,\beta} V_{\alpha\beta}^{rep}(\mathbf{R}_{\alpha\beta}) \quad (2.45)$$

The E_{SCC} term can be simply explained as the contribution of charge-charge interactions energy of the systems. However, its form is quite complex. Here, we explained the summarized of the E_{SCC} that is widely used for DFTB2 method. If the reader is interested in the derivation, please refer to the review in [34]. The Δq_α is the charge fluctuation of a neutral atom, q_α^0 , calculated using Mulliken population analysis

$$\Delta q_\alpha = \sum_i n_i \sum_{\mu, \nu \in \alpha} c_{\mu i} c_{\nu i} S_{\mu\nu} - q_\alpha^0 \quad (2.46)$$

The γ function is a distance dependent function with two limiting cases. If the interatomic distance is large, the value is proportional to $\frac{1}{|\mathbf{r}-\mathbf{r}'|}$ where the exchange-correlation term vanishes. If the interatomic distance is small, i.e. $|\mathbf{r}-\mathbf{r}'| \rightarrow 0$, the function is on-site repulsion. When $\alpha = \beta$, the γ function can be approximated as Hubbard parameter U_α .

In DFTB, the orbital Ψ_i is written in the form of LCAO (Eq. (2.37)) using the minimal basis set i.e. only valence electrons are considered like in tight binding method; hence its namesake. The pseudoatomic orbitals are determined by solving Kohn-Sham like equation self-consistently usually using LDA or PBE exchange-correlation functional

$$\left[-\frac{1}{2} \nabla^2 + V_{ne}(\mathbf{r}) + \int \frac{\rho_0(\mathbf{r}')}{|\mathbf{r}-\mathbf{r}'|} d\mathbf{r}' + V_{XC}(\mathbf{r}) + V_{conf}(\mathbf{r}) \right] \phi_\mu(\mathbf{r}) = \varepsilon_\mu \phi_\mu(\mathbf{r}) \quad (2.47)$$

The Kohn-Sham-like equation (Eq. (2.47)) contains additional terms $V_{conf}(\mathbf{r})$ in order to mimic the environment in molecules or solids. The detailed description of the confining potential will be explained in the next section.

Having determined the best orbital, the Hamiltonian and overlap matrix element ($H_{\mu\nu}^0$ and $S_{\mu\nu}$) can be determined using two-center approach, neglecting the crystal field terms $\langle \phi_\mu | V_\gamma | \phi_\nu \rangle$ and three-center terms. The overlap matrix element can be calculated in a

straightforward way (second line of Eq. (2.40)). For the Hamiltonian matrix element, there are 2 approaches used in current DFTB, the first is called potential superposition, i.e.

$$H_{\mu\nu}^0 = \begin{cases} \varepsilon_\mu & \text{if } \mu = \nu \\ \langle \phi_\mu | \hat{T} + V[\rho_0^\alpha] + V[\rho_0^\beta] | \phi_\nu \rangle & \text{if } \alpha \neq \beta \\ 0 & \text{otherwise} \end{cases} \quad (2.48)$$

and the other is called density superposition

$$H_{\mu\nu}^0 = \begin{cases} \varepsilon_\mu & \text{if } \mu = \nu \\ \langle \phi_\mu | \hat{T} + V[\rho_0^\alpha + \rho_0^\beta] | \phi_\nu \rangle & \text{if } \alpha \neq \beta \\ 0 & \text{otherwise} \end{cases} \quad (2.49).$$

The diagonal Hamiltonian matrix elements, $H_{\mu\mu}^0 = \varepsilon_\mu$, are usually obtained by solving the KS like equation, Eq. (2.47), without confining potential, i.e. $V_{conf}(\mathbf{r}) = 0$. Therefore the diagonal Hamiltonian matrix element can be obtained from standard DFT atomic calculation.

Like in DFT, in order to obtain the best molecular orbital Ψ_i , the DFTB total energy should be minimized. In DFTB, the variational parameter is the atomic orbital coefficient c_μ , like in the tight-binding theory. Minimizing the total DFTB energy with respect to the atomic orbital coefficient will result in the secular equation

$$\sum_i c_{i\mu} (H_{\mu\nu} - \varepsilon_i S_{\mu\nu}) = 0 \quad \forall \mu, i \quad (2.50)$$

with

$$H_{\mu\nu} = H_{\mu\nu}^0 + \frac{1}{2} S_{\mu\nu} \sum_\xi (\gamma_{\alpha\xi} + \gamma_{\beta\xi}) \Delta q_\xi \quad (2.51).$$

The atomic orbital coefficient $c_{i\mu}$ and Mulliken charge depend on each other. Therefore the secular equation must be solved self-consistently.

In DFTB, it is possible to compute only the first two terms on the right-hand side of Eq. (2.44). Such a method is often called as non-SCC DFTB (NCC-DFTB) or DFTB1.

NCC-DFTB has much lower computational cost compared to SCC-DFTB (DFTB2) due to only one time diagonalization to solve the eigenvalue problem (i.e. the second term on the right-hand side of Eq. (2.51) equals to zero and $H_{\mu\nu} = H_{\mu\nu}^0$). NCC-DFTB works well for a system that has no or small charge-charge interaction, for example, the homonuclear systems and hydrocarbon systems. However, for the description of systems with strong charge-charge interaction, such as for polar molecules, it fails to describe the charge transfer correctly. Therefore, for systems that are polar or have large differences of electronegativity among their atoms, it is highly advised to use the DFTB2 method.

2.4.3 Improvement of DFTB

2.4.3.1 Spin-polarized DFTB

DFTB2 calculations can be performed via spin-polarized scheme and non-spin-polarized scheme since DFTB allows fractional occupation number (there is no spin polarization scheme in DFTB1). DFTB uses so called spin coupling constant to describe difference between up and down population as well as the charge differences between spin up and spin down obtained from Mulliken population. In spin-polarized DFTB scheme, there is additional term in the total energy definition, i.e. for sDFTB2

$$E_{sDFTB2} = E_{H0} + E_{SCC} + E_{rep} + E_{spin} \quad (2.52)$$

where the definition of E_{spin} is [35,36]

$$E_{spin} = \frac{1}{2} \sum_A^N \sum_{l \in A} \sum_{l' \in A} p_{Al} p_{Al'} W_{All'} \quad (2.53)$$

where the p_{Al} are differences between spin up and down Mulliken populations on atom A with angular momentum l . These values are calculated self-consistently. The constants $W_{All'}$ are defined by

$$W_{All'} = \frac{1}{2} \left(\frac{\partial \mathcal{E}_{l\uparrow}}{\partial n_{l\uparrow}} - \frac{\partial \mathcal{E}_{l\downarrow}}{\partial n_{l\downarrow}} \right) \quad (2.54)$$

where the $n_{l\uparrow}$ and $n_{l\downarrow}$ are the atomic occupation numbers for spin up and down, respectively. $\mathcal{E}_{l\uparrow}$ is the Kohn-Sham eigenvalues for spin up orbital. The value of $W_{ll'}$ is equal to $W_{l'l}$, becoming the elements of a symmetric matrix \mathbf{W} . The schematics of matrix \mathbf{W} can be shown in Eq. (2.55), and the values of $W_{ll'}$ for Ni as an example are listed in Table 2.1.

$$\mathbf{W} = \begin{bmatrix} W_{ss} & W_{sp} & W_{sd} \\ W_{ps} & W_{pp} & W_{pd} \\ W_{ds} & W_{dp} & W_{dd} \end{bmatrix} \quad (2.55)$$

Table 2.1 Spin coupling constant $W_{All'}$ for Ni atom computed using PBE functional. The values are taken from ref. [35].

$W_{ll'}$	s	p	d
s	-0.016	-0.012	-0.003
p	-0.012	-0.022	-0.001
d	-0.003	-0.001	-0.018

2.4.3.2 Third order DFTB (DFTB3)

DFTB2 is the approximation from DFT from up to second order Taylor expansion of the reference density. Expansion of Eq. (2.43) to the third order will yield the definition of total energy

$$E^{DFTB3} = E^{DFTB2} + E_3 \quad (2.56).$$

The third order energy is defined as [6]

$$E_3 = \frac{1}{3} \sum_{ab} \Delta q_a^2 \Delta q_b \Gamma_{ab} \quad (2.57)$$

with Hubbard derivative Γ defined as

$$\begin{aligned}
\Gamma_{ab} &= \frac{\partial \gamma_{ab} \partial U_a}{\partial U_a \partial q_a} \Big|_{q_a^0} \quad \text{with } a \neq b \\
\Gamma_{ba} &= \frac{\partial \gamma_{ab} \partial U_b}{\partial U_b \partial q_b} \Big|_{q_b^0} \quad \text{with } a \neq b \\
\Gamma_{aa} &= \frac{1}{2} \frac{\partial \gamma_{aa} \partial U_a}{\partial U_a \partial q_a} \Big|_{q_a^0}
\end{aligned} \tag{2.58}.$$

DFTB3 is more reliable method for the systems involving hydrogen bonds where it improves the hydrogen bonding energies compared to DFTB2 [6]. Like in DFTB2 method, the DFTB3 can also have the spin-polarized scheme.

2.4.3.3 Long-range corrected DFTB (LC-DFTB)

DFTB2 method, which is derived from DFT, inherits the infamous SIE problem coming from the use of local or semilocal DFT exchange-correlation functional [37]. Following the idea of LC-DFT to correct the SIE, the long-range scheme of DFTB, dubbed as LC-DFTB [38,39] can be proposed. After derivations and some approximations, the total energy of LC-DFTB takes the form

$$E^{LC-DFTB} = \sum_{\mu\nu} \left(H_{\mu\nu}^{(0)} P_{\mu\nu} + \frac{1}{2} H_{\mu\nu}^{(1)} \Delta P_{\mu\nu} \right) + E_{rep} \tag{2.59}.$$

In Eq. (2.59), $P_{\mu\nu}$ is the density matrix from orbital coefficient $c_{\mu,vi}$

$$P_{\mu\nu} = 2 \sum_i c_{\mu i} c_{\nu i}^* \tag{2.60}.$$

Zeroth order Hamiltonian, $H_{\mu\nu}^{(0)}$, can be computed similarly with the conventional DFTB Hamiltonian approximation

$$H_{\mu\nu}^0 = \begin{cases} \varepsilon_\mu & \text{if } \mu = \nu \\ \langle \phi_\mu | \hat{T} + V + V^{XSR+C} + V^{XLR} | \phi_\nu \rangle & \text{if } \alpha \neq \beta \\ 0 & \text{otherwise} \end{cases} \tag{2.61}$$

The term V^{XSR+C} is the short-range (DFT) exchange potential plus the correlation potential and V^{XLR} is the long-range (HF) exchange potential. The first order Hamiltonian,

$H_{\mu\nu}^{(1)}$, includes a fairly complicated charge-charge interaction function including the range-separated γ function. The LC-DFTB method has shown to give comparable results with LC-DFT on the description of frontier orbitals of several organic molecules, as well as correcting the SCC divergence problem for some protein models calculations encountered previously in our group [39]. The computational efficiency of LC-DFTB is two to three orders of magnitude faster compared to standard DFT, suggesting a promising efficient performance for QM/MD simulations.

2.4.4 Parameterization in DFTB

2.4.4.1 Introduction to DFTB parameters

Being that DFTB2 is an approximate method, several parameterizations should be done beforehand, in order that the method becomes useful. Generally, there are two kinds of parameterization in DFTB, namely electronic and repulsive parameterization. The electronic parameterizations are devoted to find the best atomic orbital in order to accurately calculate atomic orbital energies, Hubbard values, spin constants and the both Hamiltonian and overlap matrix elements.

As mentioned in previous section, the orbital energy for the diagonal matrix element can be calculated directly from standard DFT calculation. The Hubbard parameters (not used for NCC-DFTB) can be calculated by the means of Janak theorem [40] from Kohn-Sham unconfined orbital energy

$$U_{\mu} \approx \frac{\partial^2 E}{\partial n_{\mu}^2} = \frac{\partial \varepsilon_{\mu}}{\partial n_{\mu}} \quad (2.62).$$

The determination of Hubbard value can be practically done by varying the occupation number in an orbital. One can then plot the orbital energy as a function of its occupation number. The Hubbard value can then be calculated by analytically or numerically

deriving the orbital energy function with respect to occupation number. The values of spin coupling constants in Eq. (2.54) can also be determined similarly to the Hubbard value. Additionally, for DFTB3, the Hubbard derivative, $\frac{\partial U}{\partial q}$ from Eq.(2.58) can also be computed using Janak theorem in similar method of computing Hubbard parameter.

Meanwhile, the confined orbitals are used for constructing off-diagonal Hamiltonian and overlap matrix elements. This can be done by correctly adjusting the confining potential. The confining potential is basically employed in order to mimic the bonding environment of a system either in molecular or periodic systems since the radius of atoms in bonding state is shorter than the radius of free atoms, therefore either the orbital or density should be compressed.

There are several approximations for finding the best confining potential in the DFTB community. The general traditional form of the confining potential is

$$V_{conf}(r) = \left(\frac{r}{r_o}\right)^k \quad (2.63).$$

In the earlier implementation of DFTB method, the value of k is either 2 (harmonic) or 4 (quartic). Until now, many DFTB parameters use the $k = 2$ which usually come from Frauenheim's group and Elstner's group and old parameters from Seifert's group (see next section). The choice of r_o is usually optimized in order to fit to the band structure, typically 1.5 to 2 times of the atomic covalent radius. Recently, Heine's group proposed that the k should also be optimized instead of kept fixed as well as the r_o to get better agreement with the electronic band structure [41]. Witek *et al.* proposed the idea to use the confining potential in the form of Woods-Saxon potential [42] (Eq. (2.64)) that is widely used for nuclear science to describe nucleons (protons and neutrons) interactions among each other, to

take into account the relativistic effect of the atoms [43].

$$V_{conf}(\mathbf{r}) = \frac{W}{1 + \exp(-a(\mathbf{r} - r_0))} \quad (2.64).$$

The values of W , a , and r_0 determine the shape of the potential. W is the height of potential, r_0 is the position where $V_{conf}(\mathbf{r})$ is equal to a half of W , and a is proportional to the gradient of slope at $V_{conf}(r_0)$. Figure 2.1 shows the comparison between the traditional confining potential and the Woods-Saxon potential with certain value of parameter. In order for the Woods-Saxon confining potential to be effectively working, the Dirac-Kohn-Sham like eigenvalue equation is used instead of Kohn-Sham like equation (Eq. (2.65))

$$[-ic\boldsymbol{\alpha}\nabla + (\boldsymbol{\beta} - \mathbf{1})c^2 + V_{ne}(\mathbf{r}) + \int \frac{\rho_0(\mathbf{r}')}{|\mathbf{r} - \mathbf{r}'|} d\mathbf{r}' + V_{xc}(\mathbf{r}) + V_{conf}(\mathbf{r})] \phi_\mu(\mathbf{r}) = \varepsilon_\mu \phi_\mu(\mathbf{r}) \quad (2.65)$$

where c is the velocity of light, $\boldsymbol{\alpha}$ and $\boldsymbol{\beta}$ are Dirac matrices, $\mathbf{1}$ stands for unit matrix. ϕ_μ is spinor-like atomic radial wave function with energy ε_μ , which includes both scalar and spin-orbit relativistic effect. The pseudoatomic orbitals are then generated by averaging total four-components of ϕ_μ .

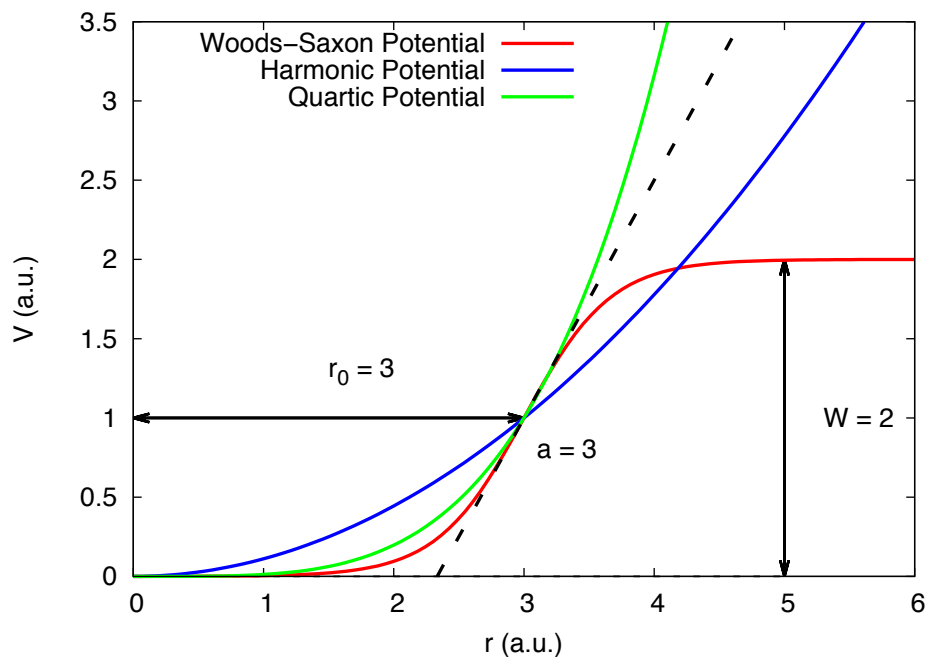


Figure 2.1 Comparison between Woods-Saxon potential and traditional confining potential. For Woods-Saxon potential, $W = 2.0$, $a = 3.0$ and $r_0 = 3.0$. The traditional confining potentials have similar r_0 value.

Having the optimized pseudoatomic orbitals from SCF calculations, the off-diagonal Hamiltonian and overlap matrix elements can be determined. For calculations of Hamiltonian and overlap matrix elements, the method of choice is up to the creators or the users for which the superposition method is used. While Frauenheim's parameters and Elstner's parameters are usually calculated using density superposition, Heine's and Seifert's parameters are calculated using potential superposition. The important thing is the user should be consistent of which sets are used, i.e. one should not mix the density superposition based and potential superposition based parameters in one system. The calculated Hamiltonian, overlap matrix elements, orbital energy for each shell and Hubbard parameters are stored in so-called Slater-Koster files. The Hamiltonian and overlap matrix elements are tabulated according to Slater-Koster rule [44]. For complete format of a Slater-Koster file please refer to site www.dftb.org.

At this point, we can already obtain the contribution of the band structure energy and the SCC energy. The remaining energy contributions are stored in the repulsive energy. As explained above, the repulsive energy takes into account the contribution of core-core electronic interactions, nucleus-nucleus repulsive interaction, the contribution of the exchange-correlation potential and the other system-independent term that is not known in details. By the definition, the repulsive energy is the difference between total energy and the total electronic energy

$$E_{rep} = E^{DFTB} - E_{BS} - E_{SCC} \quad (2.66).$$

It is already mentioned above that the E_{rep} can be broken down into the pairwise repulsive potential between atoms (Eq. (2.45)). Since in the beginning the DFTB total energy, E^{DFTB} is not known, the DFTB total energy can be approximated by either experimental value or theoretical calculation (DFT or other high level wave function method). In the current practice, the latter is more preferred since it allows to generate a versatile amounts of reference data.

Technically, there is no rule how to create the repulsive potential by itself. The only general rule is that the good parameterization of repulsive potential should minimize the energy difference between the reference and DFTB i.e. minimizing the error (for DFTB2)

$$\sum (E^{ref} - E^{DFTB2})^2 = \sum \left(\frac{1}{2} \sum_{\alpha, \beta} V_{\alpha\beta}^{rep}(R_{\alpha\beta}) - E_{BS} - E_{SCC} - E^{ref} \right)^2 = \min \quad (2.67).$$

The approximation of E_{rep} and the otherwise approximate nature of DFTB usually lead to lacking of universal transferability for a parameter. In the cases of successful parameterizations, the validity of a good parameter set can extend to a wide range of applications.

In the usual practice, repulsive parameterization for a pair of elements (for example C-C repulsive potential, $V_{CC}^{rep}(R)$) is conducted by varying the bond distances of desired pair while keeping the other bonds frozen in selected molecule(s) or solid-state systems. One can get the total reference energy and the DFTB electronic energy. The $V_{CC}^{rep}(R)$ curve can be obtained by subtracting the total reference energy and DFTB electronic energy with respect to C-C distance. In order to mimic different environment in the molecular and solid-state systems, one can construct a repulsive curve by merging different curve sections that represent different environment in molecules or solids. For example, the carbon-carbon repulsive potential can be constructed by combination of $E^{ref} - E_{el}$ curve from ethane, ethene and ethyne in order to take single, double and triple carbon bonds into account for the repulsive (see Figure 2.2). The resulting curve is further shifted and tuned in order to make smooth curve and to improve to be comparable with DFT reference data test sets. However, it is often that tuning a repulsive potential involve a tremendous amount of work; making a repulsive potential can take up to few months to generate good comparison between DFT and DFTB.

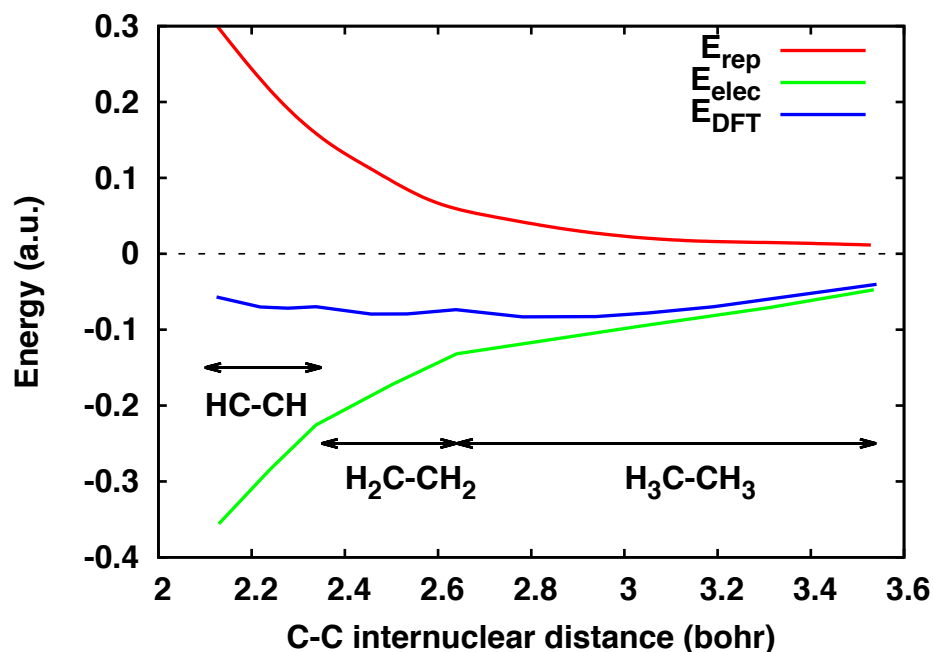


Figure 2.2 C-C repulsive potential fitting curve. The curve is combination from ethane, ethene and ethyne stretching curve. E_{DFT} is the total shifted DFT energies of each molecule at their respective C-C stretching ranges, E_{elec} is the DFTB electronic energy corresponding to DFT geometry and E_{rep} is difference between two curves. The figure is reproduced from ref. [45].

2.4.4.2 Currently available DFTB2 parameters

By the time of this thesis is written, many complete parameter sets are already published. Figure 2.3 illustrates all of the elements that have been completely parameterized (electronic + repulsive) of the periodic table. The first complete set parameters dated back to the original formulation of DFTB2. Elstner *et al.* developed the parameters for organic and bio molecules containing C, H, O and N [4] which become standard *mio* parameters. The C, H, O, N *mio* parameters has been used as backbone for extensions of many other important parameters, either for molecules or solid-state systems. Those extended parameters including the extension for S [46] and P [6] containing compounds; first row transition metals of Sc, Ti, Fe, Co, and Ni as *trans3d* parameters [47]; halogen containing compounds Cl, F, Br, I as *halorg* [48]. The aforementioned parameters have been usually tested only to molecules while they usually underperform for solid-state systems. As for *mio* based parameters that

have been tested for either molecules or solid state systems including partial B – H parameter as *borg* [49]; Ga, Ag, As, S parameter as *hyb* [50,51] and its partial As-S-H improvement as *chalc* [52,53]; Zn and Ti containing compound as *znorg* [54] and *tiorg* [55], respectively; and Au containing compounds with C, H, O, N, S as *auorg* [56].

1	1 IA	1	1.0079	H	Hydrogen	2	18 VIIA	2	4.0025	He	Helium																																																												
3	6.941	4	9.0122	Li	Lithium	6	12.011	7	14.007	8	15.999	9	18.998	10	20.180	B	Carbon	N	Nitrogen	O	Oxygen	F	Fluorine	Ne	Neon																																														
11	22.990	12	24.305	Na	Sodium	13	26.982	14	28.086	15	30.974	16	32.065	17	35.453	18	39.948	Al	Aluminum	Si	Silicon	P	Phosphorus	S	Sulphur	Cl	Chlorine	Ar	Argon																																										
19	39.098	20	40.078	21	44.956	22	47.867	23	50.942	24	51.996	25	54.938	26	55.845	27	58.933	28	58.693	29	63.546	30	65.39	31	69.723	32	72.64	33	74.922	34	78.96	35	79.904	36	83.8	K	Potassium	Ca	Calcium	Sc	Scandium	Ti	Titanium	V	Vanadium	Cr	Chromium	Mn	Manganese	Fe	Iron	Co	Cobalt	Ni	Nickel	Cu	Copper	Zn	Zinc	Ga	Gallium	Ge	Germanium	As	Arsenic	Se	Selenium	Br	Bromine	Kr	Krypton
37	85.468	38	87.62	39	88.906	40	91.224	41	92.906	42	95.94	43	96	44	101.07	45	102.91	46	106.42	47	107.87	48	112.41	49	114.82	50	118.71	51	121.76	52	127.6	53	126.9	54	131.29	Rb	Rubidium	Sr	Strontium	Y	Yttrium	Zr	Zirconium	Nb	Niobium	Mo	Molybdenum	Tc	Technetium	Ru	Ruthenium	Rh	Rhodium	Pd	Palladium	Ag	Silver	Cd	Cadmium	In	Indium	Sn	Tin	Sb	Antimony	Te	Tellurium	I	Iodine	Xe	Xenon
55	132.91	56	137.33	57-71	La-Lu	72	178.49	73	180.95	74	183.84	75	186.21	76	190.23	77	192.22	78	195.08	79	196.97	80	200.59	81	204.38	82	207.2	83	208.98	84	209	85	210	86	222	Cs	Cesium	Ba	Barium	La-Lu	Lanthanide	Hf	Hafnium	Ta	Tantalum	W	Tungsten	Re	Rhenium	Os	Osmium	Ir	Iridium	Pt	Platinum	Au	Gold	Hg	Mercury	Tl	Thallium	Pb	Lead	Bi	Bismuth	Po	Polonium	At	Astatine	Rn	Radon
87	223	88	226	89-103	Ac-Lr	104	261	105	262	106	266	107	264	108	277	109	268	110	281	111	280	112	285	113	284	114	289	115	288	116	293	117	292	118	294	Fr	Francium	Ra	Radium	Ac-Lr	Actinide	Rf	Rutherfordium	Db	Dubnium	Sg	Seaborgium	Bh	Bohrium	Hs	Hassium	Mt	Mendelevium	Ds	Darmstadtium	Rg	Roentgenium	Uub	Ununbium	Uut	Ununtrium	Uuq	Ununquadium	Uup	Ununpentium	Uuh	Ununhexium	Uus	Ununseptium	Uuo	Ununoctium
57	138.91	58	140.12	59	140.91	60	144.24	61	145	62	150.36	63	151.96	64	157.25	65	158.93	66	162.50	67	164.93	68	167.26	69	168.93	70	173.04	71	174.97	La	Lanthanum	Ce	Cerium	Pr	Praseodymium	Nd	Neodymium	Pm	Promethium	Sm	Samarium	Eu	Eurpium	Gd	Gadolinium	Tb	Terbium	Dy	Dysprosium	Ho	Holmium	Er	Erbium	Tm	Thulium	Yb	Ytterbium	Lu	Lutetium												
89	227	90	232.04	91	231.04	92	238.03	93	237	94	244	95	243	96	247	97	247	98	251	99	252	100	257	101	258	102	259	103	262	Ac	Actinium	Th	Thorium	Pa	Protactinium	U	Uranium	Np	Neptunium	Pu	Plutonium	Am	Americium	Cm	Curium	Bk	Berkelium	Cf	Californium	Es	Einsteinium	Fm	Fermium	Md	Mendelevium	No	Nobelium	Lr	Lavrentium												

Figure 2.3 Periodic table of the elements. Element pairs that have been parameterized for both electronics and repulsive in the literatures are displayed with yellow background. Not all element combinations X-Y are available.

Meanwhile, a set of parameters called *abc*, is independent of *mio* parameter and has the elements containing C, H, O, N, F, Si and Fe that has been tested mainly for periodic boundary condition [36,57–59]. A set of N interaction with Eu and Ga called *rare* [60] and a set involving Si, O, H elements called *siband* [61,62] have also been independently developed without *mio* set, which is mainly devoted to give accurate description of the electronic properties of the systems. The aforementioned sets generally come from Thomas Frauenheim’s group or Marcus Elstner’s group. Thomas Heine’s group and Gotthard Seifert’s group during 2004 – 2009 also developed the parameters aimed mainly for material

simulations in periodic boundary condition. The parameters already cover B, Na, Mg, Al, Si, Cu, Ti interactions with C, H, O, N, P, S denoted as *matsci* [63]. Those parameters created by aforementioned research groups have been publicly available in internet website www.dftb.org. On the other hand, there are also several published papers on DFTB2 parameters but are not publicly available. Shakar *et al.* developed the parameters for Cd, S, Se, Te elements interactions with C, H, O, N [64] and Saha *et al.* extends those parameters with Zn for description of zinc chalcogenides compounds [65]. Hellström *et al.* created the modification of Zn – O repulsive parameters to give better description of ZnO polymorphs in bulk, surface and nanowire [66]. All of the parameters above use the confining potential in the form of harmonic potential i.e. $k = 2$ in Eq. (2.57).

In the attempt to improve the electronic parameters, recently, Heine's group already created the electronic parameters all of the elements across the periodic table with the optimized k and r_0 value from Eq. (2.57) [41]. From those electronic sets, they have already created the complete set with repulsive for H to Ca, Br [67] and Mo [68].

Nishimura *et al.* has also created the electronic parameters for the elements across the periodic table [69] using the particle swarm optimization (PSO) [70] based automatic DFTB parameterization tools [71] based on the Woods-Saxon confining potential. However, the repulsive potential based on the Woods-Saxon potential is not available yet. The current works are devoted to create the repulsive potentials based on the Woods-Saxon electronic confining potential. The PSO method will be explained in Chapter 5.

Chapter 3 Coupled Cluster and Density Functional Studies of Atomic Fluorine Chemisorption on Coronene as Model Systems for Graphene Fluorination

3.1 Introduction

Chemical functionalization by single atoms is one of the most straightforward methods to alter the physical properties of carbon-based materials for their further use in devices. One of the most prominent atoms used for graphene functionalization is fluorine, which is mainly chosen due to its natural unique properties, such as high electronegativity and small atomic radius. The oldest known fluorinated carbon based material is fluorinated graphite [72,73], which has been recognized since about 80 years ago [73] as the applications ranging from cathode material in lithium battery to solid lubricant [74]. Nowadays, in the era of nanotechnology, fluorination is employed to alter the electronic and molecular structure of low dimensional carbon structures like fullerene [75], carbon nanotubes [76] and graphene [7]. Examples are fluorinated fullerenes [77], single-walled carbon nanotubes (SWCNTs) [78–81] and graphene/graphene nanoribbons [82–84], which are candidates for applications in the field of molecular electronics. Among them, fluorinated graphene, or so-called fluorographene, remains the most extensively studied, since graphene itself has as zero band gap with a high intrinsic charge carrier mobility, corresponding to a semimetal [7]. Upon fluorination, a band gap opens in graphene [84–88], which allows the application of fluorographene in electronic devices that require semiconducting materials properties, such as sensors, transistors, etc. Moreover, it was shown in previous experimental [84] and theoretical [89] studies that the band gap of fluorographene depends on the stoichiometric composition, namely the F/C ratio. The band gap can be tuned from 0 eV for pure graphene

(semimetal) up to 2.9 eV (semiconductor) by increasing the F/C ratio from 0 to 25% while other accurate theoretical studies predict that fully fluorinated graphene (F/C ratio of 100%) is insulator with band gap of 7 – 8 eV [90,91]. Experimental works show that fully fluorinated graphene has an optical band gap and emits UV light with an energy ca. 3.8 eV [85], while the single-sided fluorinated (F/C ratio of 50%), boat-shaped graphene has an electronic band gap of 6.2 eV [87]. These remarkable properties enable fluorographene to be a good candidate for either electronic or optoelectronic applications with tunable band gap, depending on the CF composition.

Fluorographene can be synthesized by direct reaction of graphene with XeF_2 [82,84] and F_2 gas; [83] liquid phase exfoliation from graphite fluoride; [92] reduction from graphene-oxide using HF solution [93] and diethylaminosulfur trifluoride [94]. Recently, more simple and controllable ways to synthesize fluorographenes via atomic exposure to graphene using either CF_4 or F_2 [95–97] have been reported. In these processes, graphene is fluorinated using the F atom radical generated from the precursor molecules via plasma treatment [95,96] or laser vaporization [97]. The generated F radical will aggressively attack the graphene surface to form a one-sided fluorinated graphene if it is not free-standing [89].

Thus far, several theoretical studies have been conducted on the molecular and electronic structure of fluorographenes. Several theoretical studies based on density functional theory (DFT) were carried out either to predict equilibrium geometries and binding energies of fluorine atoms in different fluorographenes [84,98–112] or to elucidate the graphene fluorination reaction mechanism and its energetics [105,113]. Depending on the employed quantum chemistry code, theoretical studies of graphene fluorination have either used periodic boundary conditions to model infinitely extended graphene sheets, or molecular

models such as pyrene, coronene and circumcoronene [101,105,114,115]. However, knowledge about the dynamics and mechanism of atomic F adsorption on graphene is still lacking. Moreover, fluorine is known to be poorly described when electron correlation is not adequately accounted for since it is an electron-rich element, and to date no *ab initio* correlated wave function theory (WFT) method has been used to study the atomic fluorine attack on graphene or a graphene model system.

For this reason, we decided to perform a thorough investigation of the potential energy curve (PEC) for the atomic fluorine attack on a central carbon atom in coronene ($C_{24}H_{12}$) as a molecular model for graphene, which allows us to employ both DFT and *ab initio* WFT levels of theory. The obtained results establish a high-level benchmark for future simulations of atomic fluorine attack on graphitic surfaces, and elucidate problems with conventional and approximate DFT-based methods due to their inherent self-interaction error (SIE).

3.2 Computational methodology

There are only three distinct adsorption sites for atomic fluorine on the six central carbon atoms of coronene, namely “top”, “bridge” and “hollow” sites as shown in Figure 3.1. Among them, only the “top” site attack will result in a strong C-F chemical bond, since the singly occupied fluorine $2p_z$ electron will interact with a singly occupied carbon $2p_x$ electron to form a covalent C-F bond, resulting in an sp^3 -hybridized carbon defect radical structure. It is also evident from previous studies that the “bridge” site is a saddle point connecting two “top” adsorption sites in fluorine migrations on polyaromatic hydrocarbons [115] and the “hollow” site is a higher order saddle point with even higher adsorption energy. Therefore, in this work, we limited our studies to the chemisorption on the “top” site. Also, since our goal

is the study of the fluorination of extended sp^2 -hybridized nanographene systems, fluorination of the coronene edges should not be considered in this study.

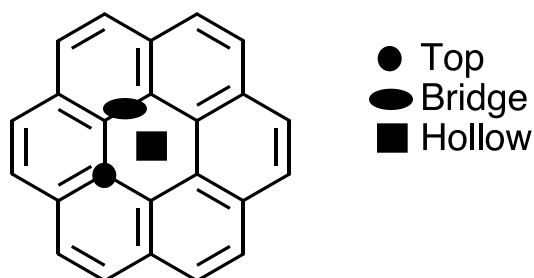


Figure 3.1 Possible adsorption sites on coronene ($C_{24}H_{12}$).

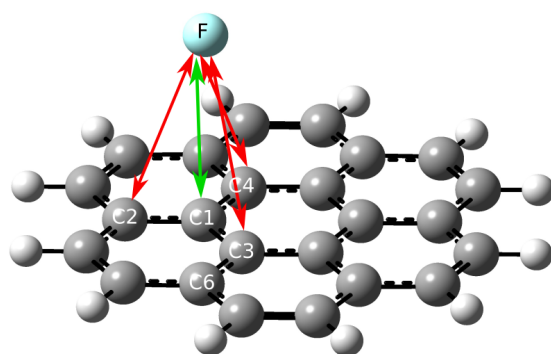


Figure 3.2 Atom labeling and potential energy curve (PEC) coordinate of the fluorine attack on the “top” site in coronene. The green line shows the C1-F distance used as reaction coordinate of the frozen and partially frozen PECs, while red lines show the distances that were additional fixed in partially frozen PEC scans below C1-F distances of 2.2 Å.

We performed frozen and fully relaxed potential energy scans for a coronene-F system in the “top” attack configuration, using the B3LYP [22,26] DFT functional and Dunning’s cc-pVDZ basis set. The calculations were performed for the doublet electronic ground state using spin-unrestricted Kohn-Sham molecular orbitals (MOs). In the PEC scans, the central C1-F bond was reduced from 4.0 to 1.0 Å with 0.1 Å intervals as reaction coordinate (see Figure 3.2).

In the frozen potential energy scan, we performed single point energy calculations with coronene geometries optimized at B3LYP/cc-pVDZ level of theory and a single F atom in the “top” position at a given distance from C1. Fully relaxed scans were performed by freezing the C1-F bond (see Figure 3.2) and allowing the rest of the atoms to be relaxed. In both cases, we start our scans with an initial C1-F distance of 4.0 Å and use the previous wave functions for the each geometry with decreasing carbon-fluorine distances. However, because of intermediate adsorption of fluorine on the coronene edge, a fully relaxed scan is not suitable for the purpose to study surface fluorination, and therefore we devised a partially frozen PEC scan as outlined in section 3.3.1.

Using the geometries along the partially relaxed PEC scan, we further performed single point energy calculations to evaluate the PECs using various first principles DFT functionals as well as *ab initio* MP2 and CCSD(T) WFT methods. The following DFT functionals were selected to determine if there were trends based on the type of functionals: the generalized gradient approximation (GGA) functionals PBE [24] and BLYP [21,22], hybrid functionals B3LYP and PBE0 [116], and range separated functionals CAM-B3LYP [32], LC- ω PBE [29,30] and LC-BLYP [21,22,31]. All DFT calculations were carried out using the spin-unrestricted formalism. For the *ab initio* MP2 and CCSD(T) method, we chose the restricted open-shell (RO) scheme, since the spin contamination of the unrestricted Hartree-Fock (UHF) reference wave function was unacceptably large in equilibrium fluorinated coronene structure, mainly because of the spin density symmetry breaking in graphene-related compounds [117]. The T1 diagnostic from CCSD(T) calculations always showed that the T1 value was less than 0.02, suggesting that the system has little nature of multiconfiguration [118]. Therefore, we employed the single determinant

approach here. The cc-pVDZ basis set was employed in all single point calculations, and the considerably larger cc-pVTZ and cc-pVQZ basis was employed in ROMP2 calculations. In doing so, ROCCSD(T)/cc-pVTZ energies can then be obtained using a G2MS-type [119] basis set energy extrapolation as follows:

$$\begin{aligned}
 E(\text{ROCCSD}(T)/cc - \text{PVTZ}) &\cong \text{G2MS} \\
 &= E(\text{ROCCSD}(T)/cc - \text{pVDZ}) + E(\text{ROMP2}/cc - \text{pVTZ}) \quad (3.1). \\
 &\quad - E(\text{ROMP2}/cc - \text{pVDZ})
 \end{aligned}$$

Complete basis set limit energy extrapolation were also conducted using SCS-MP2 [120] method using cc-pVTZ to cc-pVQZ extrapolation scheme from Halkier *et al.* [121,122]

In addition to the DFT and *ab initio* calculations, we also performed approximate DFT calculations within the framework of the density-functional tight-binding (DFTB) method [5]. In order to explicitly include charge-charge interactions, we used the second-order self-consistent-charge DFTB (SCC-DFTB [4], also known as DFTB2), as well as the more recent third-order DFTB3 [6] flavors of DFTB.

All DFT and SCS-MP2 calculations were performed using the Gaussian 09 [123] code while single point *ab initio* ROMP2 and ROCCSD(T) WFT energy calculations were performed using the Molpro [124] code. DFTB2 and DFTB3 calculations were carried out using the DFTB+ [125] program suite, both with the pbc-0-3 [57] and 3-ob-3-1 [126] Slater-Koster parameter set, respectively, using both spin-unpolarized and spin-polarized DFTB (sDFTB) [35,36]. In all DFTB calculations we used an electronic temperature of 300 K. Spin constants for C and H were taken from Kohler's work [35], while those for F were taken from the recent work by Kubar *et al.* [48]

3.3 Results and discussion

3.3.1 PEC scans at the B3LYP/cc-pVDZ level of theory

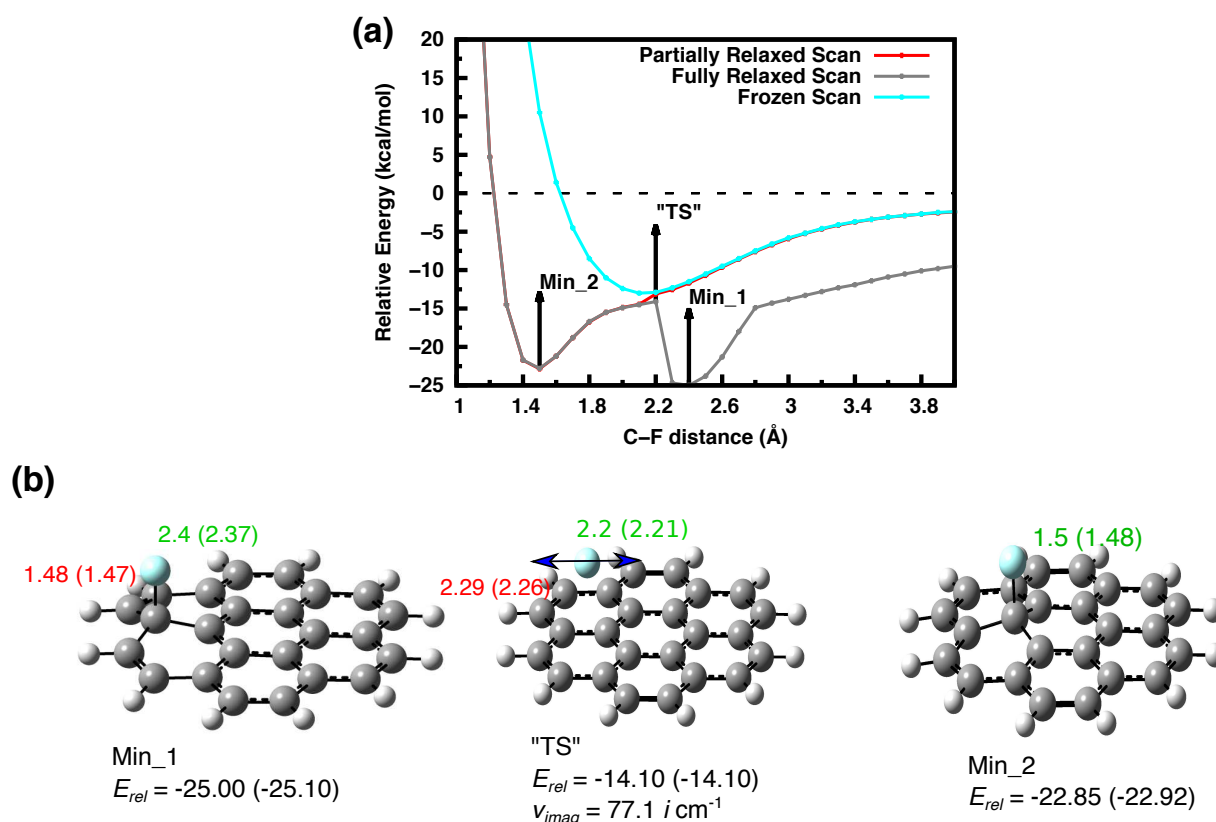


Figure 3.3 (a) PECs of the frozen (light blue), fully relaxed (grey), and partially relaxed (red) scans at the B3LYP/cc-pVDZ level of theory. Note that the red curve is hardly visible as it smoothly connects fully relaxed and frozen scans in the region where the C1-F distance is approximately 2.2 Å. (b) Geometry of first minimum (Min_1), transition state ("TS") and the second minimum (Min_2) based on PEC of relaxed scan. Green colors denote the C1-F bond length, while red colors indicate the C2-F bond length. Numbers in parentheses are the fully optimized geometry. Bond lengths are given in units of Å, while the relative energy (E_{rel}) is in kcal/mol.

The initial geometry at a C1-F distance of 4.0 Å was taken from an optimized coronene geometry with the fluorine atom directly above C1 atom and the angle C2-C1-F = C3-C1-F = C4-C1-F = 90.0°, and reduced in intervals of 0.1 Å to 1.0 Å, using the converged Kohn Sham MOs from the previous steps as initial guesses. The frozen PEC scan shows a single minimum energy at a C1-F distance of ~2.2 Å and increases steadily with increasing distance of the F atom from the coronene molecular surface as shown in Figure 3.3(a).

However, such a frozen scan does not consider the relaxation of the coronene molecule and hence underestimates the relative coronene-F interaction energy, which we define as:

$$E_{rel} = E_{coronene-F} - E_{coronene} - E_F \quad (3.2)$$

where E_{rel} is the relative (or negative binding) energy, $E_{coronene-F}$ is total energy of the composite supermolecular system, and $E_{coronene}$ and E_F are the total energy of the isolated, fully-relaxed coronene (singlet) and fluorine (doublet) atom in their ground state, respectively. The zero level of the PECs corresponds to $E_{coronene} + E_F$, obtained from two separate energy calculations. Note that for spin-polarized calculations, the reference energy is obtained using closed-shell singlet coronene and spin-polarized fluorine in its ground doublet state, whereas in the absence of spin polarization, the reference energy is computed using the restricted open-shell approach for fluorine in case of *ab initio* WFT methods.

Figure 3.3 shows that in the fully relaxed PEC scan, two exothermic minima appear. The minimum labeled **Min_1** corresponds to a structure with a C-F single bond between an edge C2 atom and the attacking F atom with a bond distance of 1.48 Å, whereas **Min_2** corresponds to a structure where the F atom forms a single bond to the central C1 atom with a bond length of 1.50 Å. It is clear that for C1-F distances greater than 2.2 Å, F prefers binding to edge C2 rather than to central C1. The relative energy at **Min_1** is -25.00 kcal/mol and thus slightly stronger than at **Min_2** with -22.85 kcal/mol. This is consistent with previous works [114,115,127] which show that edge functionalization is energetically more favorable than functionalization on the graphene π -system [127]. Approaching **Min_1** in PEC scans is undesirable for the purpose of studying surface fluorination, and we therefore decided to construct a partially frozen B3LYP/cc-pVDZ PEC scan as follows.

From 2.2 Å to 4.0 Å, we imposed an additional constraint to the scan; namely,

C2-F, C3-F and C4-F bond distances (see Figure 3.2) were also frozen and we assumed that the C-C bond lengths around the adsorption site (C1-C2, C1-C3, and C1-C4 bonds) and the planarity of the coronene molecule are unchanged compared to the fully relaxed coronene geometry. Below the 2.2 Å C1-F distance, we froze only the C1-F bond and allowed the other degrees of freedom to relax, exactly as in a fully relaxed scan. For C1-F bond lengths greater than 2.3 Å the partially relaxed PEC scan closely resembles the PEC of the frozen scan and exhibits a smoother transition for the full range of the C1-F distances than the fully relaxed PEC scan, as shown in Figure 3.3.

Figure 3.3 also shows that the “top” site attack in frozen and partially frozen PEC scans has no reaction barrier at the B3LYP/cc-pVDZ level of theory. In the case of hydrogenation, state crossing between formally neutral coronene + H and formally fully charged coronene⁺ + H⁻ is responsible for the appearance of a small adsorption barrier of about 4.6 kcal/mol both in the coronene-H [128] and graphene-H [129] systems at the same level of theory. Due to the higher electronegativity of F and the higher exothermicity of the fluorination compared to the corresponding hydrogenation reaction, as discussed in reference [89], the energy of the corresponding coronene⁺ + F⁻ state is considerably lowered, resulting of an overall lowering of the relative fluorine adsorption energies and thus a vanishing barrier. The barrierless adsorption of fluorine adsorption on graphene was also reported by Paupitz *et al.* from MD simulations using the semiclassical ReaxFF method [130].

3.3.2 B3LYP/cc-pVDZ optimized geometries

In isolated coronene, the central C1 atom has a regular sp² hybridization, along with the rest of carbon atoms. As the F atom approaches the coronene surface, the molecular

structure of coronene responds with geometrical changes. The C-C bonds around the adsorption site elongate and the C1 atom increasingly lifts off from the coronene molecular plane toward the attacking F atom, causing a so-called “puckering” angle, which is identical to the dihedral angle C2-C3-C4-C1. This puckering indicates increasing sp^3 character of the C1 atom in response to bond formation to F. In the final product, the F atom forms a covalent single bond with the C1 atom at a distance of 1.48 Å with an E_{rel} of -22.92 kcal/mol (Figure 3.3(b)). The C-C bonds around the adsorption site elongate from ~1.42 (isolated coronene) to ~1.54 Å (coronene + F product), a typical length for a C-C single bond. However, the puckering angle at C1 is 26.2° for this product structure, indicating that the hybridization of C1 does not completely correspond to a perfect sp^3 configuration, as the puckering angle for a perfect tetrahedral should be 35.3°. This finding is supported by the natural bond order (NBO) [131] analysis for the coronene-F system. The NBOs of C1 to its neighboring carbon bonds in the optimized, isolated coronene are expressed by

$$\begin{aligned}
 \sigma_{C_1=C_2} &= 0.7071(sp^{2.01})C1 + 0.7071(sp^{2.01})C2 \\
 \sigma_{C_1=C_3} &= 0.7071(sp^{2.01})C1 + 0.7071(sp^{2.01})C3 \\
 \sigma_{C_1=C_4} &= 0.7108(sp^{2.01})C1 + 0.7034(sp^{2.01})C4
 \end{aligned} \tag{3.3}$$

where the bonds have strong character of sp^2 . The NBOs of C1 to its neighboring carbon bonds in the optimized coronene-F product are

$$\begin{aligned}
 \sigma_{C_1-C_2} &= 0.7060(sp^{2.45})C1 + 0.7083(sp^{2.25})C2 \\
 \sigma_{C_1-C_3} &= 0.7060(sp^{2.45})C1 + 0.7083(sp^{2.25})C3 \\
 \sigma_{C_1-C_4} &= 0.7077(sp^{2.45})C1 + 0.7065(sp^{2.25})C4
 \end{aligned} \tag{3.4}$$

The NBOs show that there is indeed transition from sp^2 to sp^3 but that this transition is not complete. This is further corroborated by the fact that the binding energy of fluorinated

coronene with 22.92 kcal/mol is lower than in a compound with a clear C-F single bond such as in aliphatic C-F compounds (~ 113 kcal/mol) [132]. The geometry of around the local F adsorption site on coronene is comparable with those geometries obtained by periodic calculations. The C-F bond length ranges from 1.38 to 1.57 Å [111], and our computed value, 1.48 Å is satisfactorily similar, and the differences of angle, F-C1-C, are within 1°, meaning that the C bound F has a similar degree of hybridization.

In order to investigate the effect of the size of the π -conjugated graphene model systems, we also performed a full geometry optimization of pyrene-F ($C_{16}H_{10}$ -F) and circumcoronene-F ($C_{54}H_{18}$ -F) at the B3LYP/cc-pVDZ level of theory. Single F atomic adsorption with pyrene and circumcoronene corresponds to C/F ratio of 16 and 54, respectively. We again ignored edge adsorption and concentrated on products of fluorination at the central carbon atom in these compounds. Table 3.1 lists the binding energies ($-E_{rel}$) of these model systems with F along with the C-F bond length. It was found that an increasing number of the C/F ratio leads to slightly more positive C-F binding energy. PEC of F atom chemisorption on central atom carbon in circumcoronene exhibits similar profile compared to the PEC of F chemisorption on central atom carbon in coronene, as seen in Figure 3.4. Therefore, for practical purpose, coronene can be used as model.

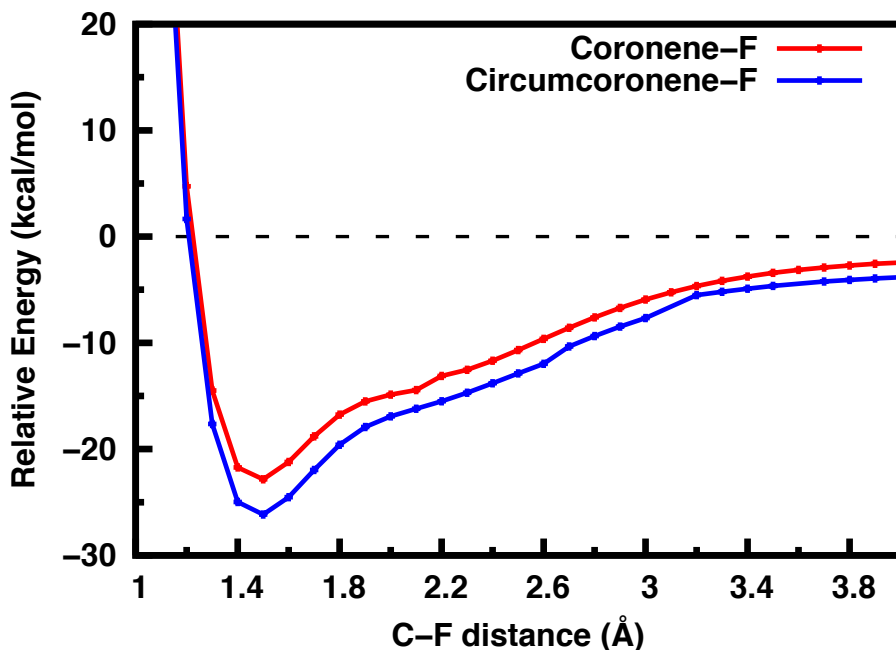


Figure 3.4 PECs of coronene-F and circumcoronene-F at B3LYP/cc-pVDZ level of theory.

Experimental estimates reported by Nair *et al.* [82] suggest that the C-F binding energy is ~ 14.2 kcal/mol for the fully fluorinated graphene. However, the authors suggest that the experimentally determined value is too small, possibly due to the presence of defects or due to unfavorable binding in the case of multiple fluorine adsorption. In fact, the theoretical binding energy of ideally fully fluorinated graphene was estimated as 113 kcal/mol [111]. Our calculated binding energy value of 22.92 kcal/mol for a single fluorine atom on coronene is certainly in excellent agreement with previously reported DFT binding energies reported by Nijamudheen *et al.* [115] and Bulat *et al.* [114]

Table 3.1 also lists the previous reported binding energy of the three different PAHs (pyrene, coronene and circumcoronene) as graphene model interaction with F using different DFT approaches. The computed binding energies are in the range from 20.0 to 26.2 kcal/mol. The reported binding energies are in excellent agreement with the present work.

Table 3.1 Fully optimized binding energy of several PAHs interaction with F.

System	C/F ratio	Method	Binding energy (kcal/mol)	Reference
Pyrene-F	16	M052X/6-31+G(d,p)	21.60	Nijamudheen <i>et al.</i> [115]
		B3LYP/cc-pVDZ	20.91	This work
Coronene-F	24	M052X/6-31+G(d,p)	24.30	Nijamudheen <i>et al.</i> [115]
		B3LYP/6-311G(d,p)	22.90	Bulat <i>et al.</i> [114]
		B3LYP/cc-pVDZ	22.92	This work
Circumcoronene-F	54	B3LYP/6-31G	20.00	Papuitz <i>et al.</i> [130]
		B3LYP/6-311G(d,p)	26.20	Bulat <i>et al.</i> [114]
		B3LYP/cc-pVDZ	26.23	This work

3.3.3 Single point energies along the partially frozen PEC obtained with various DFT and WFT methods.

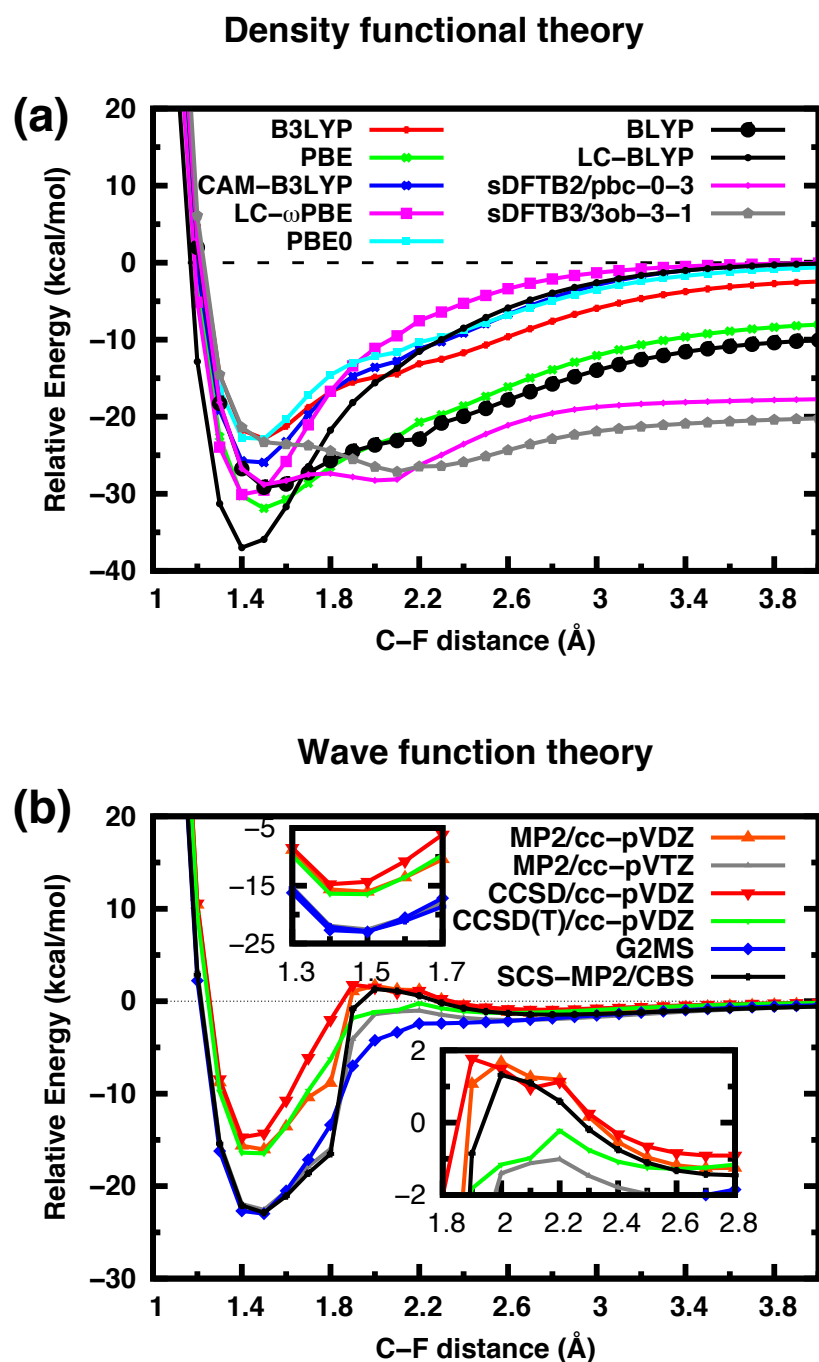


Figure 3.5 PECs of (a) DFT methods using the cc-pVDZ basis set for B3LYP/cc-pVDZ partially relaxed scan geometries, (b) *ab initio* WFT methods for B3LYP/cc-pVDZ partially relaxed scan geometries.

The binding energies for the “top” site F atom attack on the central carbon atom of coronene with various exchange-correlation DFT functionals are listed in Table 3.2, and the

corresponding PECs, based on the B3LYP/cc-pVDZ geometries from our partially frozen PEC scan, are shown in Figure 3.3(a). At first, we limit our discussion to GGA and hybrid density functionals. Unlike WFT methods, DFT is known to suffer from a self-interaction error (SIE) [133], chiefly because the exact density-based exchange functional is unknown. Thus, the SIE mainly affects pure DFT exchange-correlation functionals with no Hartree-Fock exchange (HFX).

Table 3.2 Binding energy with respect to neutral coronene and fluorine species, charge on fluorine in the unit of electron, and frontier orbital energies calculated at various DFT levels of theory.

Method	Binding energy		Charge on F at 50 Å	HOMO	SUAO
	(kcal/mol)			Energy of	Energy of F
	PEC minimum	50 Å		Coronene (eV)	(eV)
BLYP/cc-pVDZ	29.15	8.09	-0.199	-4.84	-8.35
PBE/cc-pVDZ	31.88	6.83	-0.190	-5.11	-8.35
sDFTB2/pbc-0-3	28.81	14.65	-0.249	-5.70	-10.31
sDFTB3/3-ob-3-1	23.29	15.97	-0.275	-5.66	-10.31
B3LYP/cc-pVDZ	22.85	1.01	-0.082	-5.63	-6.63
PBE0/cc-pVDZ	22.87	0.01	-0.009	-5.88	-5.90
LC-BLYP/cc-pVDZ	36.98	0.00	0.000	-7.83	-3.10
LC- ω PBE/cc-pVDZ	30.09	0.00	0.000	-7.86	-3.26
CAM-B3LYP/cc-pVDZ	25.93	0.00	0.000	-6.55	-4.71

Mixing of a few percent of Hartree-Fock Exchange (HFX) into the functional often reduces the SIE [134]. SIE is often cited for causing underestimation of activation energies [133] and

overestimation of the binding well [135]. Our results show that PBE with 0% HFX has the largest binding energy with 31.8 kcal/mol, while both PBE0 (25% HFX) and B3LYP (19% HFX) have remarkably smaller and similar values around 22.9 kcal/mol, despite different amounts of HFX mixed within both functionals. BLYP predicts a binding energy in-between PBE and the hybrid functionals with 29.2 kcal/mol. We note that the effects of the percentage of HFX mixing do not affect the C-F binding energy to a large extent.

PECs for both spin-polarized DFTB2 and DFTB3 methods along the partially frozen PEC scan, also shown in Figure 3.5(a), show that there are two minima and generally lower E_{rel} , the latter being commonly found for DFTB due to its use of a minimal basis set when atomic energies are involved in the definition of the reference energy [54]. The two minima are related to the C-F repulsive potential, which have a cutoff of 4.20 a.u. (~ 2.2 Å) and 3.94 a.u. (~ 2.0 Å) in the pbc-0-3 and 3-ob-3-1 DFTB parameter sets, respectively, and cause the unphysical second minima for the geometries of partially relaxed PEC scan. In addition, the DFTB2/3 coronene-F dissociation limits at 4.0 Å, where it can be safely assumed that the C-F interaction has completely decayed, are far lower than the zero energy level with E_{rel} values converging to around -20 kcal/mol. Since experimentally and theoretically, the ionization potential (IP) of coronene is higher with 166.3 kcal/mol [136] than the electron affinity (EA) of F with 78.4 kcal/mol [137], it is expected that the dissociation of coronene-F leads to both neutral species. This means that the total energy of the isolated coronene-F supersystem has to converge to the energy of an isolated coronene molecule plus the energy of an isolated fluorine atom. Hence, for large C-F distances, E_{rel} and the binding energy $-E_{rel}$ should approach exactly 0 kcal/mol at the dissociation limit according to Eq. (3.2). Conventional DFT functionals with no HFX such as PBE and BLYP

also converge to negative dissociation values of -8.03 and -10.05 kcal/mol, respectively. Apparently, the SIE causes spin delocalization, leaving both species still charged. This unphysical artifact of pure DFT functionals is reduced in hybrid functionals that include HFX, where PBE0 and B3LYP predict the dissociation limit to be -0.63 and -2.44 kcal/mol, respectively. The largest errors in the dissociation limit were obtained for both spin-polarized DFTB. sDFTB2 with pbc-0-3 parameter predicted the dissociation limit to be -17.72 kcal/mol while sDFTB3 with 3-ob-3-1 predicted the dissociation limit to be -20.20 kcal/mol.

Ab initio WFT calculations are free from the SIE of DFT. The coupled cluster theory with singles, doubles and perturbative triples is often referred to as the “gold” standard among quantum chemical methods. In particular, the CCSD(T) method using large basis sets such as Dunning’s cc-pVTZ, or even larger, is desirable. Due to computational resource limits, in this work, we employed a G2MS-type [119] basis set extrapolation to estimate the CCSD(T)/cc-pVTZ PEC energies as defined in Eq. (3.1). As shown in Figure 3.5(b), our results show that the relative energy obtained at the PEC minimum point using the ROMP2/cc-pVDZ level of theory is -16.04 kcal/mol, noticeably identical to the ROCCSD(T)/cc-pVDZ value of -16.45 kcal/mol. The larger basis set in ROMP2/cc-pVTZ reduces the relative energy by 6.53 kcal/mol to -22.57 kcal/mol. Using these binding values obtained from ROMP2/cc-pVDZ, ROCCSD(T)/cc-pVDZ and ROMP2/cc-pVTZ levels of theory, we obtained an estimated binding energy by G2MS, 22.98 kcal/mol, and the SCS-MP2 binding energy, 22.87 kcal/mol at extrapolated complete basis set limit, both in surprisingly good agreement to standard B3LYP with the smaller cc-pVDZ basis set. A similar surprisingly good agreement between G2MS and B3LYP was previously reported for the hydrogenation of coronene [128].

In the following section we discuss the shape of the PECs for the *ab initio* WFT methods. As shown in Figure 3.5(b), these PECs converge to the correct dissociation limit with $E_{rel} \sim 0$ kcal/mol. Furthermore, at a separation of 50 Å, the total energy of coronene and F in a supermolecular calculation is equal to the sum of isolated coronene and F energies within micro-Hartrees. Another interesting feature is the shape of the WFT PECs, which exhibit steeper binding wells in comparison to DFT, especially for pure and hybrid functionals. Since there is no SIE in WFT methods, the aforementioned state crossing is better described. MP2/cc-pVDZ, MP2/cc-pVTZ, CCSD/cc-pVDZ, CCSD(T)/cc-pVDZ and SCS-MP2/CBS PECs show a shallow energy minimum around 2.6 Å related to a van der Waals complex, and a very small barrier around 2.0 Å not exceeding 1 kcal/mol, originating from the state crossing. This very small barrier is not present in the G2MS PEC, and it is difficult to assess whether its absence is real or originates from a still too small basis set. In any case, the small barrier predicted by some WFT methods is certainly small enough for spontaneous fluorination of nanographenes. This is the case, as fluorine atoms can be attached to graphene in mild experimental condition under 200° C [96].

We now discuss the results from range-separated DFT calculations. These methods, such as LC-BLYP, LC- ω PBE and CAM-B3LYP, predict correct dissociation limits, as can be seen in Figure 3.5(a), and the charges on coronene and fluorine become neutral, with the spin solely residing on the fluorine atom (see Table 3.2). However, since the short-range contribution in these functionals uses standard GGA with smaller or no %HFX as in LC-BLYP and LC- ω PBE, these methods still tend to predict the same or even greater binding energy as their counterpart functionals without range separation.

Table 3.3 Calculated binding energies of *ab initio* wave function methods without and with counterpoise (CP) correction at the B3LYP/cc-pVDZ fully optimized geometry of the fluorinated coronene molecule

Method	Binding Energy (kcal/mol)		
	CP-uncorrected	CP-corrected	BSSE
B3LYP/cc-pVDZ	22.92	18.30	4.62
ROMP2/cc-pVDZ	16.29	8.54	7.75
ROMP2/cc-pVTZ	22.74	19.27	3.47
CCSD/cc-pVDZ	14.80	7.10	7.70
CCSD(T)/cc-pVDZ	16.80	8.53	8.27
G2MS	23.25	19.26	3.99
SCS-MP2/CBS	22.87	22.87	-

Counterpoise (CP) corrections were calculated using the Boys-Bernardi scheme [138].

We now focus on the effect of the basis set superposition error (BSSE) on the relative PEC energies. Usually, for correlated *ab initio* WFT methods, the BSSE is larger than in DFT methods. We find this general trend also in the case of coronene fluorination, see Table 3.3. The B3LYP/cc-pVDZ level of theory predicts the BSSE to be 4.62 kcal/mol, lower than ROMP2/cc-pVDZ by 7.75 kcal/mol. With counterpoise (CP)-correction [138] in the case of ROCCSD/cc-pVDZ methods, the binding energy decreases by 7.70 kcal/mol, and is almost identical to the CP-corrected ROMP2/cc-pVDZ binding energy. The inclusion of noniterative triple excitations at the ROCCSD(T) level results in a small increase of the

BSSE by 8.27 kcal/mol. As expected, ROMP2/cc-pVTZ has the smallest BSSE energy with 3.47 kcal/mol. Assuming that the BSSE for ROCCSD(T)/cc-pVTZ can be obtained using the G2MS scheme according to Eq. (3.1), replacing total energies by the BSSE, we estimate the G2MS BSSE to be 3.99 kcal/mol, very similar to the ROMP2/cc-pVTZ BSSE. At the complete basis set limit, the BSSE energy can be assumed to be zero. The SCS-MP2/CBS binding energy is 22.87 kcal/mol, indicating that the CP-corrected binding energy of the WFT would converge to ~ 22.9 kcal/mol. It is worth mentioning that the CP-corrected value at the basis set limit of WFT will converge to that computed at either B3LYP/cc-pVDZ level of theory or G2MS. Thus, both the SCS-MP2 value and the CP-uncorrected values by B3LYP/cc-pVDZ or G2MS can be used as references.

3.3.4 Spin-polarized vs spin-unpolarized DFTB calculations.

We would like to elaborate further on the DFTB method, since its computational efficiency potentially allows its use as on-the-fly quantum chemical potential in nonequilibrium MD simulations of graphitic carbon fluorination processes. The DFTB calculations reported in the previous section were performed using the spin-polarized scheme for consistency with our spin-polarized DFT calculations. However, sDFTB has a much simplified formulation of spin-polarization compared to conventional spin-unrestricted DFT methods, as the exchange functional of DFT is replaced by an on-site spin coupling constant to describe the difference between α and β electron populations based on Mulliken spin densities in different atomic orbital (AO) shells on each atomic center.

We note that the DFTB method also can and has been applied to open-shell systems without spin polarization using fractional occupation numbers, where for instance a single unpaired electron is described by two spin AOs occupied by half α and half β spin. In

such a case, the E_{spin} term in Eq. (2.49) disappears completely.

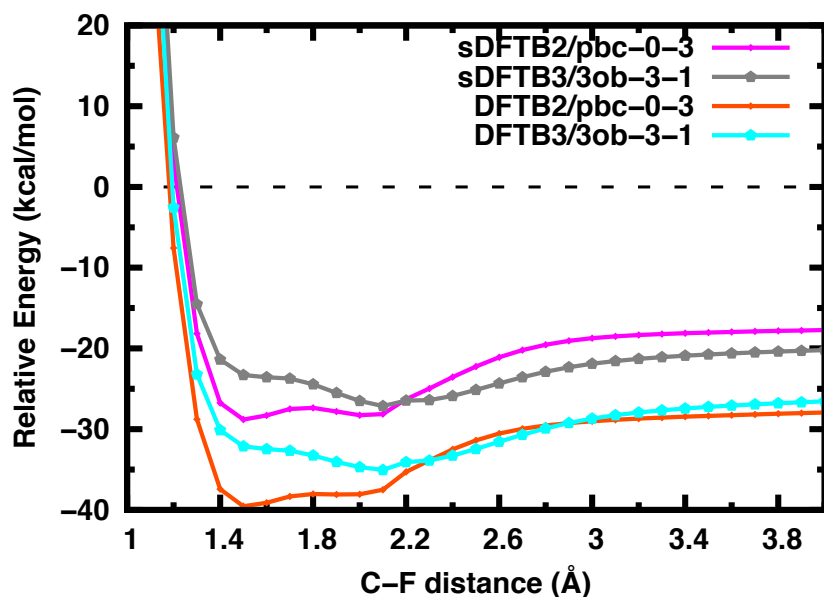


Figure 3.6 PECs of spin-polarized DFTB and spin-unpolarized DFTB methods for B3LYP/cc-pVDZ partially relaxed scan geometries.

Figure 3.6 shows spin polarized and unpolarized PECs for both DFTB2 and DFTB3 methods. sDFTB2 PEC curves are consistently higher in E_{rel} by about 10 kcal/mol relative to those from unpolarized DFTB2 over the entire range of C1-F distances, and sDFTB3 PEC curves are similarly consistently higher by about 8 kcal/mol. This comparison indicates that the shape of the PECs does not depend on whether spin polarization is used or not in DFTB2 and DFTB3 calculations. However, the dissociation limit and thereby the exothermicity of the fluorination reaction is considerably affected.

3.3.5 Origin of the incorrect dissociation limit in pure, hybrid, and approximate DFT methods.

The incorrect dissociation limit in pure, hybrid, and approximate DFT methods is accompanied by artificial partial electron transfer from coronene to F. At a coronene-F separation of 4.0 Å, one would expect almost no excess charge on F, and certainly at a separation of 50 Å both molecule and atom should be charge-neutral. However, BLYP and

PBE functionals at 4.0 Å C-F distance predict that approximately $0.3e$ are still transferred from coronene to F.

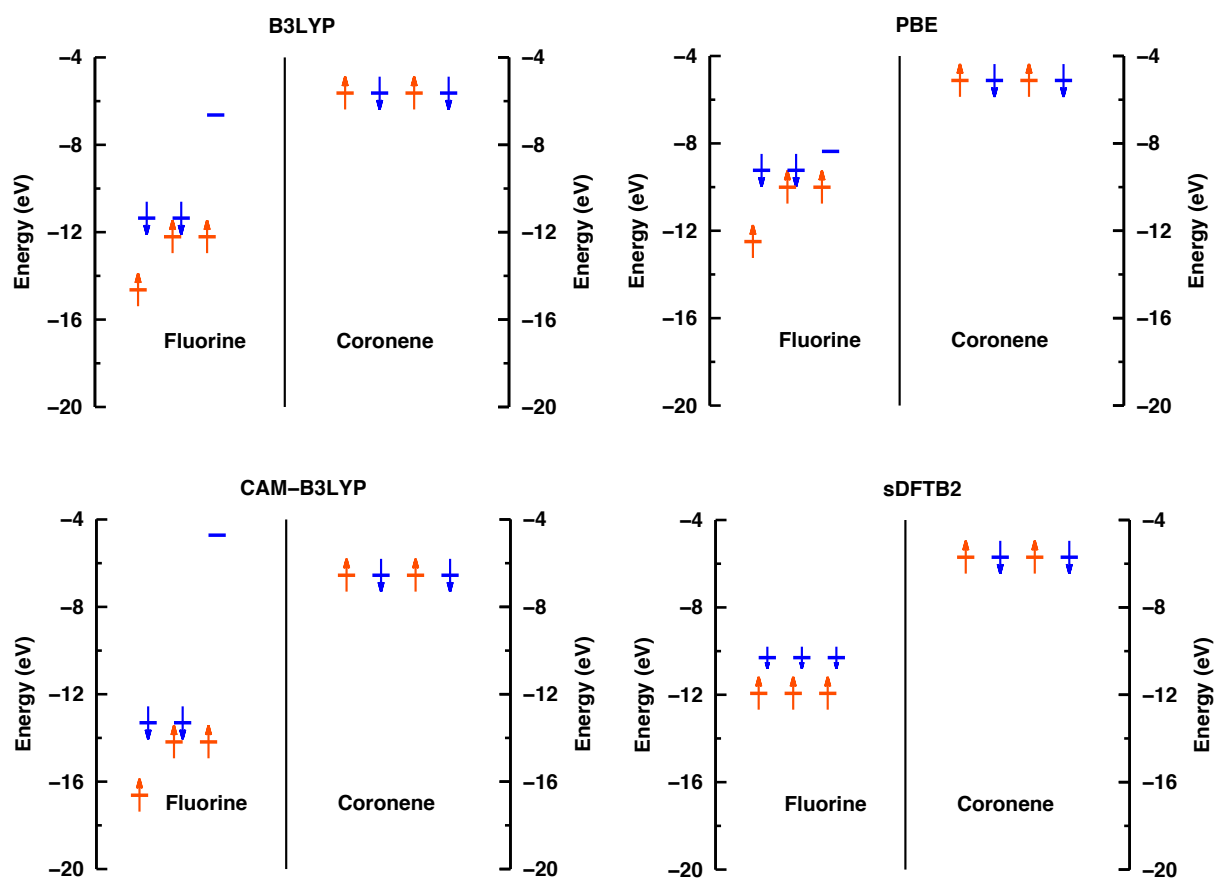


Figure 3.7 Coronene HOMO and Fluorine highest occupied and lowest unoccupied 2p atomic orbital energies calculated separately from each other at selected DFT levels of theory. Red arrows indicate α electrons, blue arrows indicate β electrons. All DFT calculations employed the cc-pVDZ basis set while sDFTB calculations employed the pbc-0-3 parameters. In the sDFTB theory, the use of fractional occupation numbers results in an occupancy of $2/3$ β electrons in the β 2p shell, as indicated by “shorter” blue arrows.

Even at a separation of 50 Å, artificial charge transfer of around $0.2e$ is observed (see Table 3.2). The artificial charge transfer in these methods occurs because the highest occupied molecular orbital (HOMO) of the isolated coronene molecule is higher than the lowest singly unoccupied atomic orbital (SUAO) of the isolated F atom (see Figure 3.7). When both species are computed in a supermolecular system, the orbitals from each species will mix. It follows that, if the SUAO (or SUMO in case of molecules) of the radical species is lower

than the HOMO of the closed shell species, following the Aufbau principle, artificial charge transfer occurs as reported previously in reference [135].

As shown in see Table 3.2 and Figure 3.7, pure functionals do indeed predict that the SUA0 of F is much lower than the HOMO of coronene, in line with their general tendency toward smaller HOMO-LUMO gaps in comparison to those obtained at the HF level of theory. Therefore, unsurprisingly, this error is less pronounced in hybrid functionals containing HFX such as B3LYP, and virtually absent in range-separated DFT methods such as CAM-B3LYP. The smaller errors in the dissociation limit of the coronene-F system confirm this general trend. On the other hand, in DFTB methods, similar as in pure DFT functionals, the HOMO of coronene is higher than the SUA0 of F, which is actually a degenerate state having a fractionally occupied 2p shell with $2/3e$ occupation in each β AO. The fractional occupation of the 2p β shell seems unusual from a chemist's perspective but yields the correct spherical electron density for a fluorine atom in vacuum. In addition, DFTB only considers spin polarization within and between AO shells belonging to the same angular quantum number, further reducing the energy of the fluorine β SUA0, hence the dissociation limit error is the largest in sDFTB2/3 among all investigated methods and the artificial charge transfer at 50 Å separation is largest with partial charges closer to $0.3e$ (see Table 3.2).

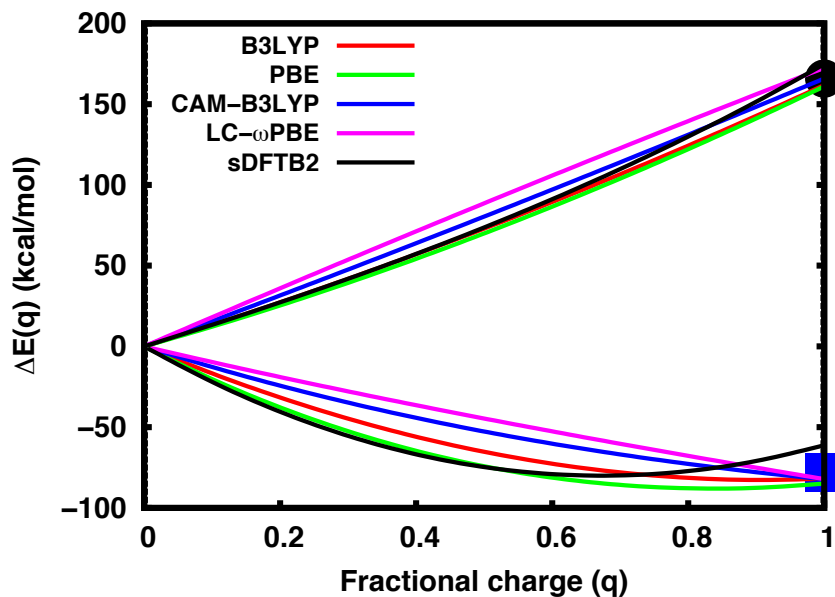


Figure 3.8 Fractional charge vs energy curve for coronene (upper five lines) and F (lower five lines). For fluorine, the aug-cc-pVDZ basis set was used to obtain its correct electron affinity in the atomic DFT calculations. The black dot and blue square on the $q=1$ ordinate represent the experimental IP of coronene and EA of fluorine, respectively.

For the above-mentioned reason, DFTB, pure DFT, and to a lesser extent hybrid DFT methods exhibit an artificial, partial electron transfer from coronene to fluorine, depending on the proximity of the coronene HOMO and the fluorine SUA0 energy levels. The fractional charge on each unit of the supermolecule at large coronene-F distances then induces an artificial stabilization of the total energy, which originates from the SIE, which is also called “delocalization error” [139]. The curves shown in Figure 3.8 show relative energies of coronene and the fluorine atoms as a function of increasingly positive and negative charge, respectively, with the energy of the neutral species as reference. These quantities are labeled $\Delta E(q)$ in Figure 3.8, and were plotted by means of a third-order polynomial interpolation using Janak [140] theorem, as shown in Eq.(3.5), and Koopman’s theorem for the gradient of start ($q=0$) and end ($q=1$) points.

$$\varepsilon_{\mu} = \frac{\partial E}{\partial n_{\mu}} \quad (3.5).$$

The latter are ideally identical to the ionization potential (IP) and negative electron affinity (EA) of coronene and F, respectively. If the exchange functional in DFT was exact, then there should be a straight line between the two states [141]. However, the actual energy-charge-curves, especially for F, show that the concaveness of the curve is related to the percentage of HFX mixing to the GGA exchange. For instance, PBE with 0% HFX is more concave than B3LYP with 20% HFX. Since HF is free from the SIE, increasing the contribution of HFX will increase the linearity of the energy-charge curve.

In DFTB methods, the amount of artificial charge transfer between coronene and fluorine is largest at the dissociation limit and approaches the maximum of the SIE at $q=0.5$. Hence, the artificial delocalization error is largest for these approximate DFT methods in the present example. DFTB is well known to show SIE and a delocalization error problem [37,142], related to the E_{SCC} and E_{spin} terms in the DFTB total energy definition [142]. As shown in Figure 3.8, DFTB energy-charge curves exhibit highest concaveness among all DFT methods. It means that the delocalization error in DFTB is most severe for the modeling of nanocarbon fluorination. A solution to this problem should become available once C-F parameters for the LC-DFTB [39], have been developed.

3.3.6 Potential energy curves from DFTB+ U calculations

A possible way to cure the self-interaction error in DFTB is via the + U correction [37]. The U value was determined in coronene-F compound to shift its dissociation limit closer to ~ 0 kcal/mol. We used the + U correction for 2s and 2p orbital of F atom based on FLL scheme [143]. We determined the U value based on the DFTB2 calculations. Table 3.4 lists the UJ value with the dissociation limit and binding energy. The dissociation limit was calculated using relaxed B3LYP/cc-pVDZ geometry of coronene-F at 4 Å C-F distances

while the binding energy was calculated at 1.5 Å C-F distances under the condition of electronic temperature of 300 K and the reference is energy of coronene and spin-polarized F. As seen from Table 3.1, increasing UJ value will shift the dissociation limit energy toward ~ 0 kcal/mol. On the other hand, it will decrease the binding energy. We found that $U = 0.08$ gives the dissociation limit of DFTB2 to 0.22 kcal/mol. However, the sDFTB2 calculations will have lower dissociation limit to be 4.85 kcal/mol.

Table 3.4 Effects of UJ value to the binding and dissociation limit energy.

UJ	DFTB2		sDFTB2	
	Binding energy (kcal/mol)			
	4.0 Å	PEC minimum	4.0 Å	PEC minimum
0.00	18.53	30.14	17.72	28.81
0.02	10.46	25.25	14.44	25.86
0.04	6.97	22.30	11.20	22.94
0.06	3.56	19.37	8.00	20.02
0.08	0.22	16.45	4.85	17.13
0.10	-3.04	13.55	1.73	4.25

The PECs of DFTB+ U method with $U = 0.08$ is shown in Figure 3.9. There is discontinuity at C-F distance around 2.5 Å. The discontinuity is probably caused by state crossing, where the SCC converges to excited states at C-F distance above 2.5 Å. Therefore, the DFTB+ U correction may not be suitable for curing the SIE in the coronene-F case.

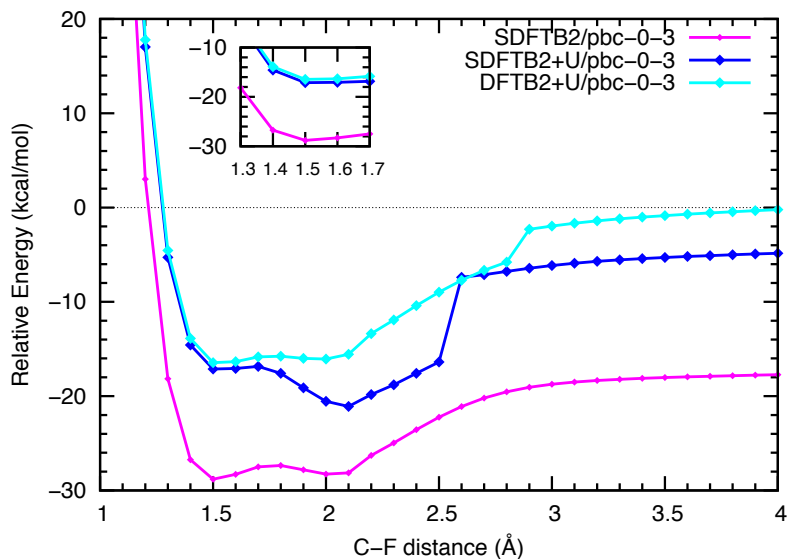


Figure 3.9 PEC of coronene-F system calculated using DFTB+ U method with $UJ=0.08$.

3.3.7 Fitting C-F repulsive potential from the potential energy curves

Due to inability to cure the delocalization error using currently available method, we propose a new C-F repulsive potential from pbc-0-3 electronic set in order to be compatible for application in interaction between F and graphitic surface based on coronene-F potential energy surface. The new repulsive is tuned to mimic the graphitic surface environment and also parameterized with the spin-polarized scheme. It will be used to further to perform of simulation of F on graphitic surface in the future.

In this section we present a modification proposal of the short-range C-F potential. We only modified the C-F repulsive potential, while keeping the other elemental pair repulsive potential and the electronic as in the original set since we consider that the most important interaction in the adsorption is the C-F interaction. We propose that instead of fitting the C-F repulsive potential with the relative energy (Eq. (3.2)) the repulsive potential is fitted to the formation energy defined as

$$E_F = E_{\text{coronene-F}} - E_{\text{coronene}} - \frac{1}{2}E_{F_2} \quad (3.6).$$

The definition of formation energy is more realistic for DFTB since the energy of

atoms calculated in DFTB2 is not well defined due to lack of repulsive. The atomic energy calculated from DFTB level of theory is generally higher than the supposed value.

The repulsive can be fitted from either high-level G2MS or B3LYP/cc-pVDZ level of theory formation energy curve. Using the formation energy definition, the PEC minimum is shifted to higher energy by approximately 18 kcal/mol for B3LYP/cc-pVDZ and G2MS while the shifting of the PEC from sDFTB2 level of theory is approximately 37 kcal/mol. Interestingly, using this definition of energy, the dissociation limit of F attack on coronene from G2MS, B3LYP/cc-pVDZ and DFTB2 converge to value of about 16-18 kcal/mol, as displayed in Figure 3.10 and the sDFTB2 formation energy of C-F at the equilibrium geometry is significantly higher than the formation energy calculated from G2MS and B3LYP/cc-pVDZ with the value of 7.24 kcal/mol. Based on the formation energy curve, it is easier to fit the C-F short-range repulsive potential to reproduce the formation energy of either G2MS or B3LYP/cc-pVDZ method.

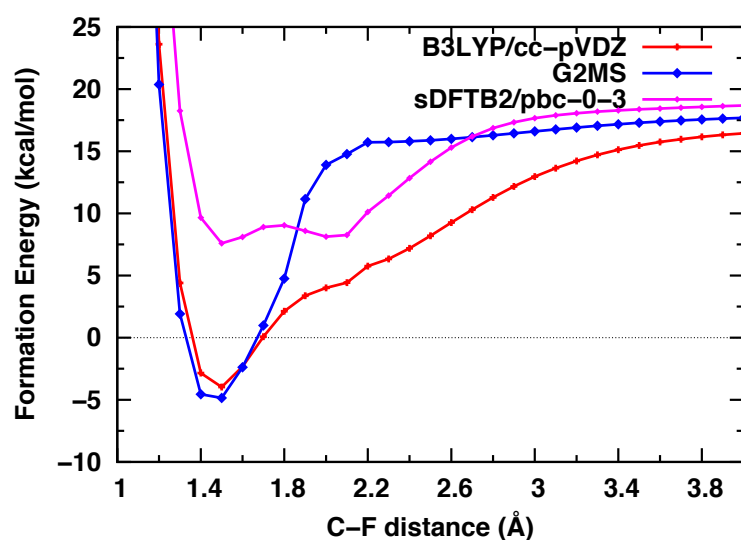


Figure 3.10 Coronene-F PECs using the definition of formation energy (Eq. (3.6)).

As a comparison, we also report the sDFTB2 relative energy. However, due to nonzero nature of the sDFTB2 dissociation limit, the sDFTB2 relative energy is shifted

properly with respect to sDFTB2 infinity distance i.e.

$$E_{rel}^{DFTB} = E^{DFTB}(S) - E_{\infty}^{DFTB}(\infty) \quad (3.7)$$

where E_{rel}^{DFTB} is the DFTB relative energy, $E^{DFTB}(S)$ is the total sDFTB2 energy of coronene-F supermolecule at geometry S and $E_{\infty}^{DFTB}(\infty)$ is the total energy of coronene-F supermolecule with C-F distance of 50 Å.

The C – F repulsive potential fitting was performed using semi-automatic DFTB repulsive parameterization code that uses the least square fitting procedure [144]. The repulsive pair $V(r)$ is represented using the M th order polynomial

$$V(r) = \sum_{i=m}^M c_{i-m}(r - r_0)^i \quad (3.8)$$

where m is usually 2 or larger in order to ensure the repulsive and the first derivative goes to zero at the cutoff value r_0 . The value of the repulsive for the distance greater than r_0 is zero. In the fitting procedure, the polynomial coefficient c_{i-m} is the free parameter to be adjusted to reproduce the reference energy. The polynomial is then converted to 3rd – 5th order spline to be compatible with DFTB+ code. We created 2 independent C-F repulsive potential based on the B3LYP/cc-pVDZ and G2MS formation energy curve. The resulting repulsive potentials are comparable. We report the sDFTB2 PEC and geometrical parameters using the new repulsive potential.

After several trial attempts, the optimum polynomial degree is 9 with $m = 3$ and the cutoff radius is 3.22 bohr for both repulsive potential to describe reasonable C-F geometry and energy within DFTB accuracy as well as maintaining good shape of the potential. In contrast to our argument from section 3.3.3 that the existing C-F pbc-0-3 repulsive potential is too repulsive if we use the definition of relative energy to fit, our repulsive potential is less

repulsive compared to the existing pbc-0-3 repulsive, as displayed in Figure 3.11 since if we use the definition of formation energy, the current pbc-0-3 will predict that coronene-F formation energy is higher than the reference value. Nevertheless, in the following sections we will show that the new repulsive potential can improve the PEC, geometry and formation energy. New C-F repulsive potential based on B3LYP (rep-B3LYP) is more repulsive than G2MS based repulsive (rep-G2MS) at the value below 3.2 bohr since the formation energy of coronene-F from B3LYP/cc-pVDZ level of theory is higher than G2MS formation energy around the minimum.

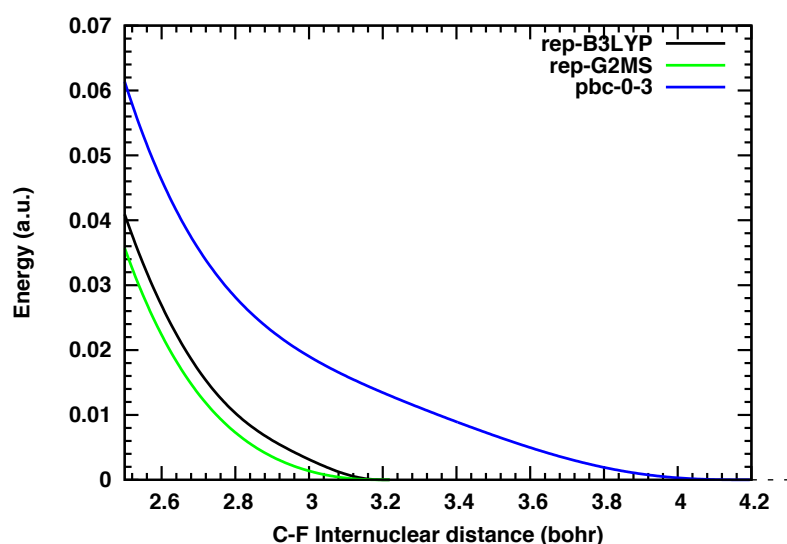


Figure 3.11 Comparison between the original C-F repulsive potential [57] and the new repulsive potentials.

Single point formation energy curve based on B3LYP/cc-pVDZ mixed relaxed scan geometry is shown in Figure 3.12. Using the new C-F repulsive potential, the formation energy curve from DFTB level of theory looks similar to the reference PEC, especially around the minimum. The formation energy minimum of DFTB2 level of theory calculated using repulsive potential based on B3LYP/cc-pVDZ and G2MS are -3.40 and -5.18 kcal/mol, respectively while the formation energy minimum of B3LYP/cc-pVDZ and G2MS level of

theory are -3.97 and -4.85 kcal/mol, respectively. Since the new repulsives are short ranged, the long-range part of the sDFTB2 PECs remains the same as the original pbc-0-3 curve. The “fake” minimum on the original pbc-0-3 PEC around 2.1 Å is not present using the new repulsive potentials.

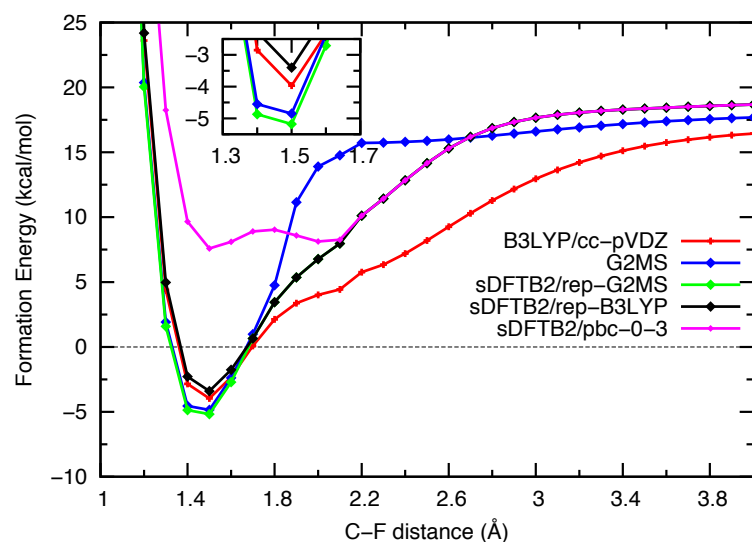


Figure 3.12 DFTB2 coronene-F PEC's using the definition of formation energy calculated using the new C-F repulsive potentials. Reference PEC's are given for comparison.

On the other hand, reducing the range of repulsive potential and making the potential less repulsive than the original pbc-0-3 potential will inevitably decrease the coronene-F total energy by approximately 12 kcal/mol compared to the total energy of original pbc-0-3 at the geometry around the minimum. This can be seen from Figure 3.13(a), where if using the definition of relative energy in Eq. (3.2), PEC minimum of pbc-0-3 is declined from -28.81 kcal/mol to -39.44 and -41.22 kcal/mol for rep-B3LYP and rep-G2MS, respectively. As shown in Figure 3.13(b), using the definition of relative energy in Eq. (3.7), the minimum will increase to -25.72 and -27.40 kcal/mol for rep-B3LYP and rep-G2MS, respectively while the shifting also increases the DFTB2/pbc-0-3 minimum to -14.16 kcal/mol. However, the shifted sDFTB2 minimum is still lower than the minimum calculated

using B3LYP/cc-pVDZ and G2MS level of theory, but higher than the unshifted DFTB2 minimum calculated using original pbc-0-3. Probably, for coronene-F case, DFTB2 electronic effect is more dominating than repulsive effect for description of relative energy, even if corrected to the total energy at “infinite” distance, where the SIE dominates at separated C-F distance. In our coronene-F case, it is rather hard to judge whether the C-F repulsive is not repulsive enough or too repulsive. Using definitions of different energies will lead to different conclusions. Nevertheless, using the definition of formation energy that is often used to describe energetics in DFTB, we obtain very accurate value of the minimum compared to the *ab initio* reference.

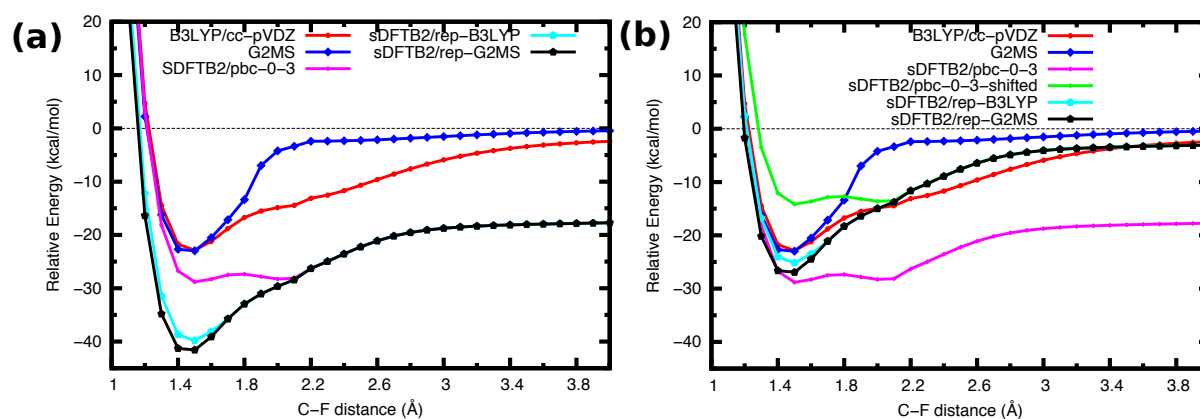


Figure 3.13 (a) PEC of several levels of theory using definition of relative energy in Eq. (3.2). (b) Shifted PEC for sDFTB2 using Eq.(3.4). Unshifted reference PEC’s are given as comparison.

Fully optimized geometry of coronene-F calculated using various levels of theory are illustrated in Figure 3.14. C-F bond distance value obtained using B3LYP/cc-pVDZ is 1.48 Å. For the sDFTB2, the C-F bond distance values obtained using rep-B3LYP and rep-G2MS are 1.47 and 1.45 Å, respectively. The difference between the B3LYP/cc-pVDZ reference and sDFTB2/rep-B3LYP and sDFTB2/rep-G2MS C-F bond distances are shorter by 0.01 and 0.03 Å, respectively and the original pbc-0-3 bond distance is longer by 0.03 Å with 1.51 Å compared to the reference. The F-C1-C angles at the adsorption site in general

are also in good agreement between the B3LYP/cc-pVDZ reference and sDFTB2 values with the value of 103.18-104.46°.

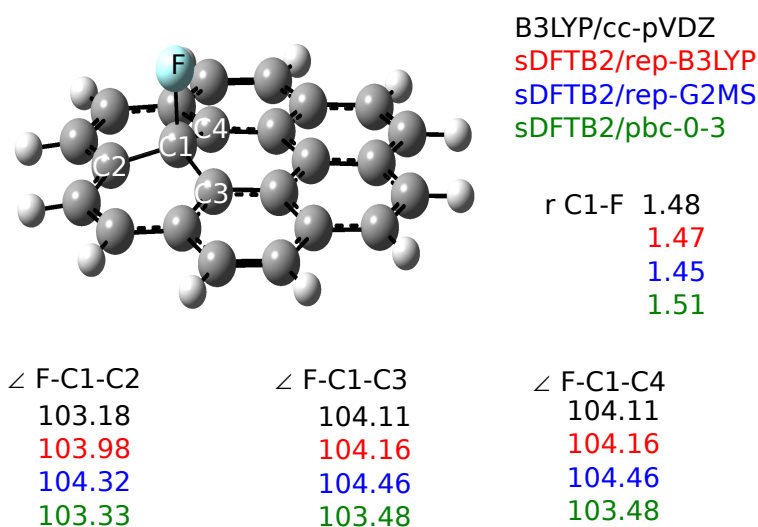


Figure 3.14 Selected geometry parameters of coronene-F calculated using B3LYP/cc-pVDZ and sDFTB2 levels of theory. Bond distances are in the unit of angstrom and angles are in the unit of degree.

Furthermore, more improved formation energy is obtained using the new C-F repulsive potential compared to the pbc-0-3 repulsive. The values of formation and binding energy are listed in Table 3.5. Coronene-F formation energy predicted by B3LYP/cc-pVDZ and G2MS has the value of -4.04 and -5.12 kcal/mol, respectively. The values of the reference can be reproduced by the sDFTB2 within DFTB accuracy. The coronene-F formation values predicted by sDFTB2/rep-B3LYP and sDFTB2/rep-G2MS are -4.00 and -6.00 kcal/mol, respectively where sDFTB2/pbc-0-3 predicts higher formation energy with 7.12 kcal/mol. The formation energy predicted by sDFTB2/rep-G2MS is lower by 2.00 kcal/mol than the value predicted by sDFTB2/rep-B3LYP since the C-F rep-G2MS is lower by ~2.00 kcal/mol compared to the C-F repulsive (see Table 3.5). Nevertheless, since DFTB has the accuracy within 3-5 kcal/mol, the formation energy difference between predicted by the new C-F repulsive is in reasonable agreement compared to the *ab initio* reference. Overall,

the performance of the both new repulsive potentials is very satisfactory for coronene-F systems to describe the formation energy and geometry compared to their respective references. Therefore, we can propose to use the new repulsive potentials for further investigations involving systems with graphene/graphitic material with fluorine atom.

Table 3.5 Formation and binding energy of coronene-F. Numbers in parentheses are the binding energy ($-E_{rel}$) calculated using Eq. (3.7).

Method	Formation energy (kcal/mol)		Binding energy (kcal/mol)	
	PEC minimum	Optimized geometry	PEC minimum	Optimized geometry
sDFTB2/pbc-0-3	7.24	7.12	28.81 (14.16)	28.93 (14.62)
sDFTB2/rep-B3LYP	-3.40	-4.00	39.45 (25.14)	40.05 (25.75)
sDFTB2/rep-G2MS	-5.18	-6.00	41.22 (26.92)	42.05 (27.75)
B3LYP/cc-pVDZ	-3.97	-4.04	22.85	22.92
G2MS	-4.85	-5.12 ^a	22.98	23.25 ^a

^aCalculated using B3LYP/cc-pVDZ geometry.

3.4 Summary

We calculated *ab initio* and DFT-based PECs for attacks of fluorine on coronene molecules in their centers at “top” site (center carbon atom). The purpose of the study was to establish a high-level benchmark for the development of fluorine–graphitic material interaction parameters. We found out that fluorine attack on coronene has no reaction barrier at the B3LYP/cc-pVDZ level of theory. In DFT methods, the percentage of Hartree-Fock exchange (%HFX) scales proportionally to the value of binding energy, in which the pure DFT functional (0 %HFX) such as PBE and BLYP predict the largest binding energy and

DFT functional with fair amount of %HFX predict lower binding energy than pure DFT functional. Additionally, we found a similar trend for the dissociation limit: For pure DFT functionals, coronene-F total energies at long separation do not converge to the sum of separate coronene molecular and fluorine atoms. Addition of % HFX to the functional either by hybrid or range separated scheme will cause the energy convergence closer to the correct dissociation limit. Our best G2MS estimate of the ROCCSD(T)/cc-pVTZ binding energy after counterpoise correction is 19.3 kcal/mol, which is very close to that from B3LYP/cc-pVDZ with 18.3 kcal/mol. We conclude that studies performed at the B3LYP level of theory are sufficiently accurate for the description of the chemisorption of a single fluorine atom on a graphitic surface. Unfortunately, at present, computationally efficient, yet approximate DFT methods such as DFTB2/3 suffer severely from the self-interaction error and are less suitable for this purpose. Parameter development for range-separated LC-DFTB is currently ongoing in our group. Instead, we have modified the C – F repulsive potential based on pbc-0-3 parameter set by fitting to the formation energy versus C – F distances profiles that had been generated from high level *ab initio* G2MS and B3LYP/cc-pVDZ level of theory.

The new potentials improve both of the formation energy curve of coronene-F and the geometry of coronene-F system around the F adsorption site. The older pbc-0-3 predicts that there are two minima in the PEC while the new potentials predict only one minimum as based on their respective references. The formation energy at the optimized coronene-F geometry calculated using the new C – F potential agree very well with the *ab initio* reference formation energy where the older pbc-0-3 predicts significantly higher formation energy. On the other hand, the relative energy calculated using the new potential is significantly lower than

the relative energy of the *ab initio* references and the pbc-0-3 set. This is due to the less repulsive nature of the new potential compared to the C –F pbc-0-3 potential. Nevertheless, using the definition of formation energy, which is better defined in DFTB2, we managed to obtain the good agreement with the references. Therefore, we propose to use the new C –F potential for the simulation of atomic fluorine attack on graphene surface.

Chapter 4 Density Functional Studies of Atomic Oxygen and Nitrogen Interactions with Coronene as Model for Graphene Functionalization

4.1 Introduction

Atomic oxygen and nitrogen have been explored to functionalize carbon-based nanomaterials. Oxygen-functionalized graphene, often called graphene oxide (GO) [145], has potential for application in electronic devices, such as field effect transistors [146], transparent conductor material for solar cells [147], and light emitting diodes [148]. In contrast, nitrogen does not functionalize perfect graphene surfaces via chemical adsorption. Instead, it replaces the carbon atom on graphene to functionalize defective graphenes to form what is often called doped graphene-N [149–151].

GO can also be used as a precursor for synthesizing graphene based nanosheets to functionalize by chemical reduction [152]. Therefore, effective synthesizing of GO is one of important issues for creating GO-based electronic materials with desired electric profile and performance. Common chemical synthetic approaches are the oxidation of graphite by strong oxidizing agent, such as KMnO_4 , which is known as Hummers method [153], followed by chemical, thermal or mechanical treatment to exfoliate the bulk into few-layered sheets [147,152,154]. However, the obtained GO has heterogeneous distribution of different functional groups of O, such as epoxide, hydroxyl, carboxylic, phenol, carbonyl, lactone, and quinone [145,155–157]. The inhomogeneity of the GO prevents smooth electron transportation on resultant graphene nanosheets compared to the pristine graphene due to defects in the nanosheets [145]. Another physical approach to obtain GO is the direct oxygen plasma exposure to graphene [158–160]. In the approach, without careful control of the

plasma oxygenation conditions, graphene would receive irreversible lattice damages and generate defects caused by high-energy species, such as O_2^+ .

One of the more promising approaches to GO synthesis is exposure of graphene to atomic O produced in thermal cracking [161,162]. O_2 molecules are cracked into O atoms on a hot tungsten filament at ~ 1500 °C under ultrahigh vacuum conditions. For both plasma as well as thermal cracking processes it is difficult to obtain information on structural transformation and reaction mechanism due to the high temperature of the process, and thus theoretical calculations are expected to provide atomic-level insight for the functionalization mechanism. A number of theoretical studies of O attack on graphene [163,164] and graphite [165,166] under periodic boundary condition have been reported. However, most studies have focused on the resulting oxidized nanosheet structures themselves, and information about the mechanism of atomic O attack on graphene is still lacking, which can help explaining the structure of GO in the aforementioned experimental results and designing GO based material. In addition, there are also scarce reports on interaction between atomic nitrogen with graphene model.

In this work, we theoretically investigated atomic oxygen and nitrogen interactions with coronene ($C_{24}H_{12}$) as a model of graphene by the means of density functional theory (DFT). We showed the possible reaction intermediates, transition states and products. Additionally, we performed semi empirical DFTB2 [4,5] calculations for comparison with DFT. The results can be used as reference for the development of DFTB parameters for further investigations of systems containing O or N atoms and graphene/graphitic surfaces.

4.2 Computational details and model systems

To predict possible stationary points, in the early stage we performed the potential

energy scan of the atom on coronene. We performed the potential energy scan depending on the distance between the atom and the coronene sheet at the "top" or "bridge" site (see Figure 3.1) to observe chemisorption of the O, while for N, we only consider the "bridge" site since the N atom will bind weakly on the "top" site as evident from previous studies [167,168]. The O atom can form one single bond or two single bonds with C species in the coronene sheet, while we did not consider the "hollow" site for both atom adsorption site because the atoms on this site should not form chemical bond with the surrounding carbon atoms. The C-X (X=O, N) distances, r_{C-X} , are defined as the distance between X and C1 at the "top" site like in the case of coronene-F (Figure 3.2), and between X and the center of C1 and C4 atoms at the "bridge" site in Figure 4.1, where $r_{C-X} = r_{C1-X} = r_{C4-X}$.

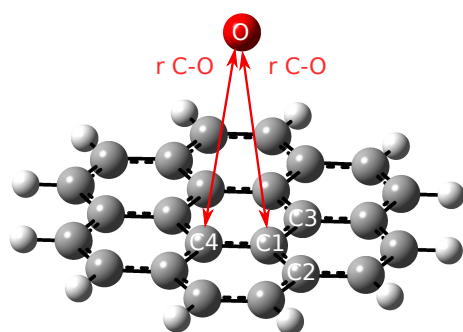


Figure 4.1 "Bridge" site potential energy curve coordinate of O attack on coronene.

The electronic ground states of the O, N atom and coronene are triplet 3P , quartet 4S , and closed-shell singlet (coronene), respectively. The atom and coronene are in their ground electronic state when they are distant from each other, while they can adapt either singlet or triplet state in the case of coronene-O and doublet or quartet state in the case of coronene-N when chemical bonds are formed. Therefore, we considered these possible electronic states to address the dependency of the adsorption mechanism on the different spin states.

After optimization of the coronene sheet, we conducted relaxed scans at "top" (only coronene-O) and "bridge" sites in triplet state in the case of O and quartet in the case of N with fixing r_{C-X} to obtain the PECs for the distance between X and each site. After obtaining the PECs, we optimized the geometries from the local minima or maxima on the PECs in the both spin states and performed vibrational analyses. In case of transition states, the intrinsic reaction coordinate (IRC) calculations were performed to confirm the obtained geometries were transition states.

We employed unrestricted B3LYP [22,26] functional with cc-pVDZ basis set for the relaxed scan "top" and "bridge" sites and full optimization of the stationary points. The UB3LYP/cc-pVDZ level of theory without BSSE seems to be accurate enough because the analogous interactions of coronene with either H or F atom evaluated by B3LYP/cc-pVDZ were similar to those estimated at the complete basis set limit of high-level WFT methods [128].

To evaluate the performance of DFTB2 parameters, single point spin-polarized DFTB2 calculations based on UB3LYP/cc-pVDZ level of theory PECs geometries were conducted using mio-0-1 parameter set [4] with spin coupling constant from Kohler's work [35] for all atoms. Since the electronic parameters of C-H-O-N elements from mio-0-1 set were parameterized using the PBE functional, and the element pair repulsive potentials were parameterized using B3LYP functional [4], it is noteworthy to compare DFTB2 PECs with both unrestricted PBE and B3LYP calculations. To give the comparable results with the basis set size of UB3LYP, cc-pVDZ basis set was also employed in PBE calculations. The DFT calculations were carried out using Gaussian 09 program [123] and DFTB calculations were carried out using DFTB+ program [125]. The interaction or relative (or negative

binding) energy of coronene-X interaction was reported as the difference of the energy of coronene-X supermolecule with the energy of coronene plus energy of the atoms at their respective ground state.

4.3 Results and discussions

4.3.1 Oxygen adsorption on coronene computed at B3LYP/cc-pVDZ level of theory

The PECs at the "top" and "bridge" site are shown in Figure 4.2. The triplet PECs for both attack sites in Figure 4.2(a) show that the largest interaction energy, -1.7 kcal/mol, at $r_{c-o} = 2.7 \text{ \AA}$ and $r_{c-o} = 2.7 \text{ \AA}$ for "top" and "bridge" attack sites, respectively. The interaction energy can be considered as an entrance channel minimum which resembles a van der Waals (vdW) complex, which is similar to the case of graphene models and OH radical [169]. The PEC at "top" site shows a local maximum of 6.3 kcal/mol at $r_{c-o} = 1.8 \text{ \AA}$ and local minimum of -0.4 kcal/mol at $r_{c-o} = 1.4 \text{ \AA}$, while the PEC at "bridge" site shows a local maximum of 14.5 kcal/mol at $r_{c-o} = 1.8 \text{ \AA}$ and local minimum of 3.3 kcal/mol at $r_{c-o} = 1.5 \text{ \AA}$. The maximum and minimum of the PECs are the indications of the activation barrier of O attack to coronene and formation of coronene-O adduct, respectively. In addition, the PEC obtained by single point calculations in the singlet state at the scanned geometries in triplet state as shown in Figure 4.2(b), a local minimum of 1.5 kcal/mol at $r_{c-o} = 1.4 \text{ \AA}$ and -20.4 kcal/mol at $r_{c-o} = 1.5 \text{ \AA}$ were obtained for "top" and "bridge" site, respectively, indicating the formation of coronene-O adduct.

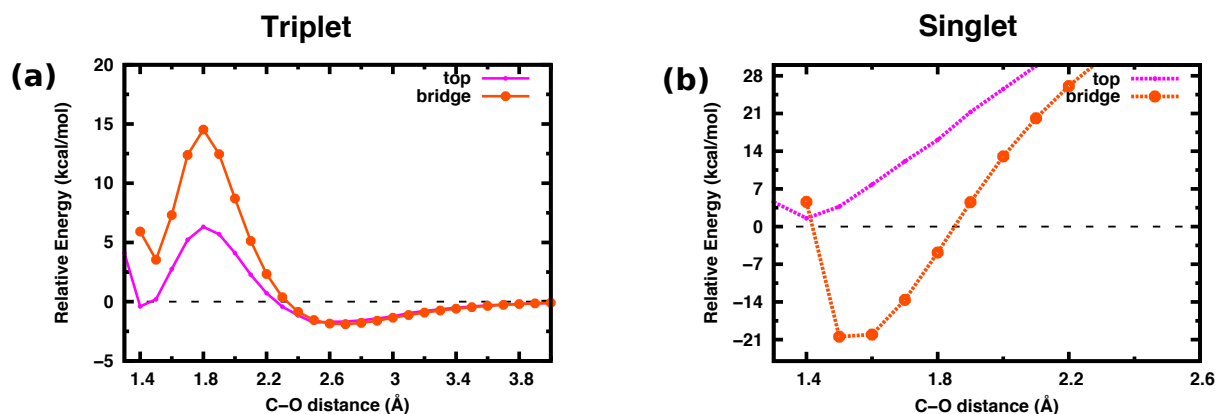


Figure 4.2 The PECs of the interaction between coronene and O at B3LYP/cc-pVDZ level of theory in (a) triplet and (b) singlet state. The PECs in singlet state were obtained by single point calculations based on triplet state relaxed scan geometries.

The stationary points that are described above are not the true lowest energy since they were computed with the fixing of the distance of C – O bonds. These geometries can be used as initial geometries to obtain the global minimum structures on each spin state, described below.

According to the obtained PECs, we can assume an energy diagram for atomic O interaction with the coronene as a graphene model at each site. The stationary points which can be read from the PECs at the "top" site can locate around $r_{c-o} = 1.4 \text{ \AA}$ as oxidized coronene, $r_{c-o} = 2.5 \text{ \AA}$ as vDW complex, and the medium region between them to form C-O bond. In the case of the "bridge" site, the points can be around $r_{c-o} = 1.5 \text{ \AA}$ as oxidized coronene, $r_{c-o} = 2.6 \text{ \AA}$ as vDW complex, and the medium region between them to form C-O bond and change the spin state. The obtained stable species are named alphabetically and the geometries at transition states are indicated by the name of their reactant and product. The relative (or interaction) energies to the sum of total energy of coronene and O (3P) state were used to draw the energy diagram for the consistency with the PECs.

Regarding the triplet state as shown in in Figure 4.3(a), the vDW complexes at "top" and "bridge" site converged to the same species **A** where O atom locates on the "top"

site with the C1 – O distance, 2.67 Å and the interaction energy of -2.0 kcal/mol. The geometry at the local maximum (around $r_{c-o} = 1.8$ Å) on the PEC of the "top" site was optimized and a first order transition state named **TS(AB)** was observed, where the O located in the "top" site with $r_{c1-o} = 1.82$ Å and interaction energy of 6.1 kcal/mol. On the other hand, the optimized geometry converged to an undesired second order transition state in the case of "bridge" site. This geometry would not be included in the remaining discussions. We succeeded in obtaining two stable structures of coronene-O adduct, namely **B** and **C** from the initial structures of oxidized coronene around $r_{c-o} = 1.4$ Å at "top" and "bridge" sites, respectively. Both of **B** and **C** have the interaction energies of -1.8 kcal/mol and 3.3 kcal/mol, respectively. In addition, we obtained a first order transition state between **B** and **C**, namely **TS(BC)** with $r_{c1-o} = 1.43$ Å and $r_{c4-o} = 1.73$ Å and interaction energy of 6.1 kcal/mol, which was not expected from the relaxed scan PECs. For the singlet state as shown in Figure 4.3(b), there are two possibilities of geometries at the "bridge" site, namely "edge-bridge" (named **D**) and "graphitic-bridge" site (named **E**). The "edge-bridge" geometry, **D** was obtained from the geometry of $r_{c-o} = 1.4$ Å on the PEC of the "top" site since the "top" site is not a stable species in singlet state. Meanwhile, the "graphitic-bridge" geometry was obtained from the geometry of $r_{c-o} = 1.4$ Å on the PEC of the "bridge" site. Both of **D** and **E** have epoxide structures with the interaction energies, -35.0 kcal/mol and -29.2 kcal/mol, respectively. The structure of the transition state between **D** and **E**, **TS(DE)**, was successfully optimized with the distance, $r_{c1-o} = 1.42$ Å and the interaction energy 1.2 kcal/mol.

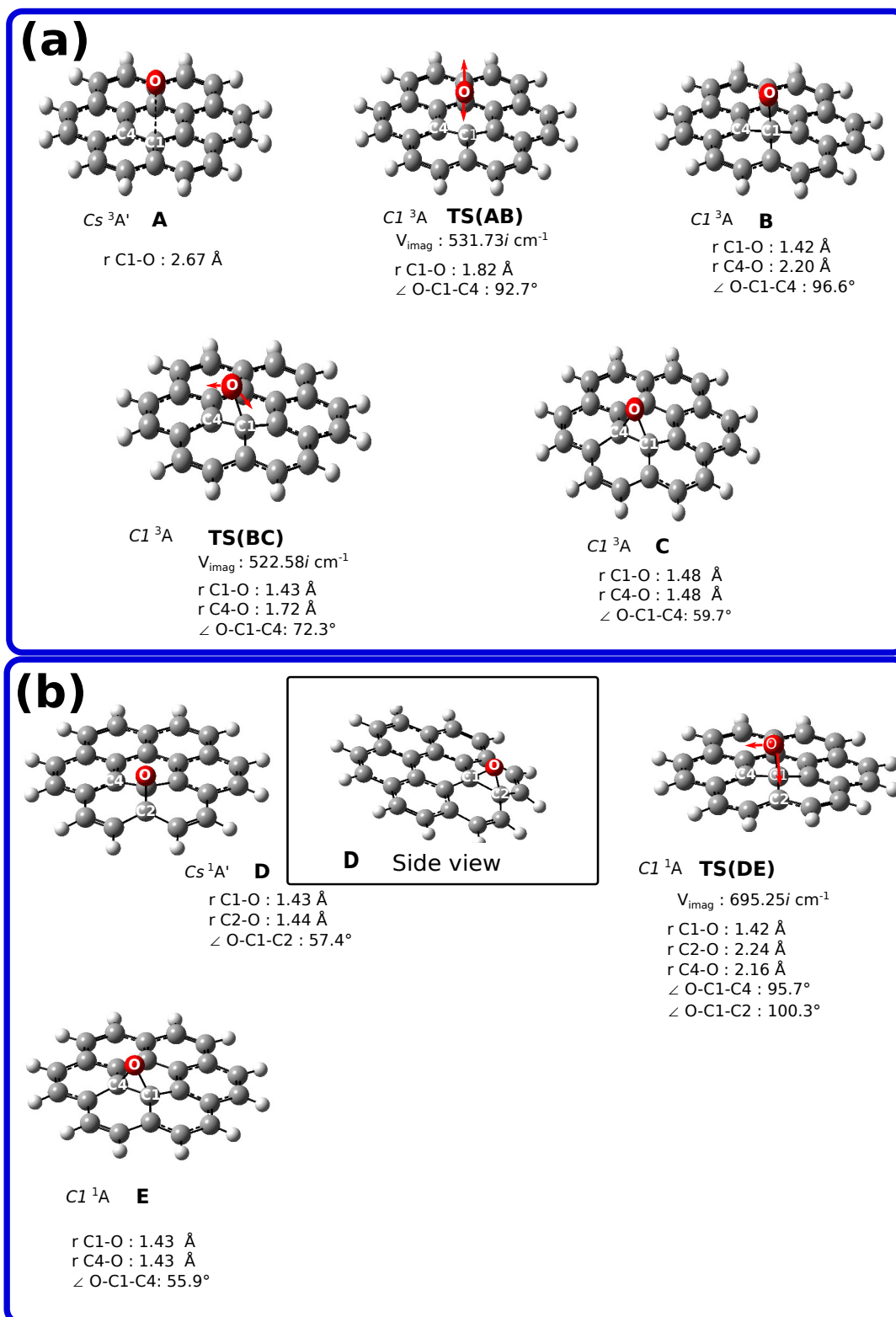


Figure 4.3 Optimized geometries of intermediates and transition states with their selected geometrical parameters in (a) triplet and (b) singlet states. The imaginary frequencies mode for the transition state are drawn by red colored arrows.

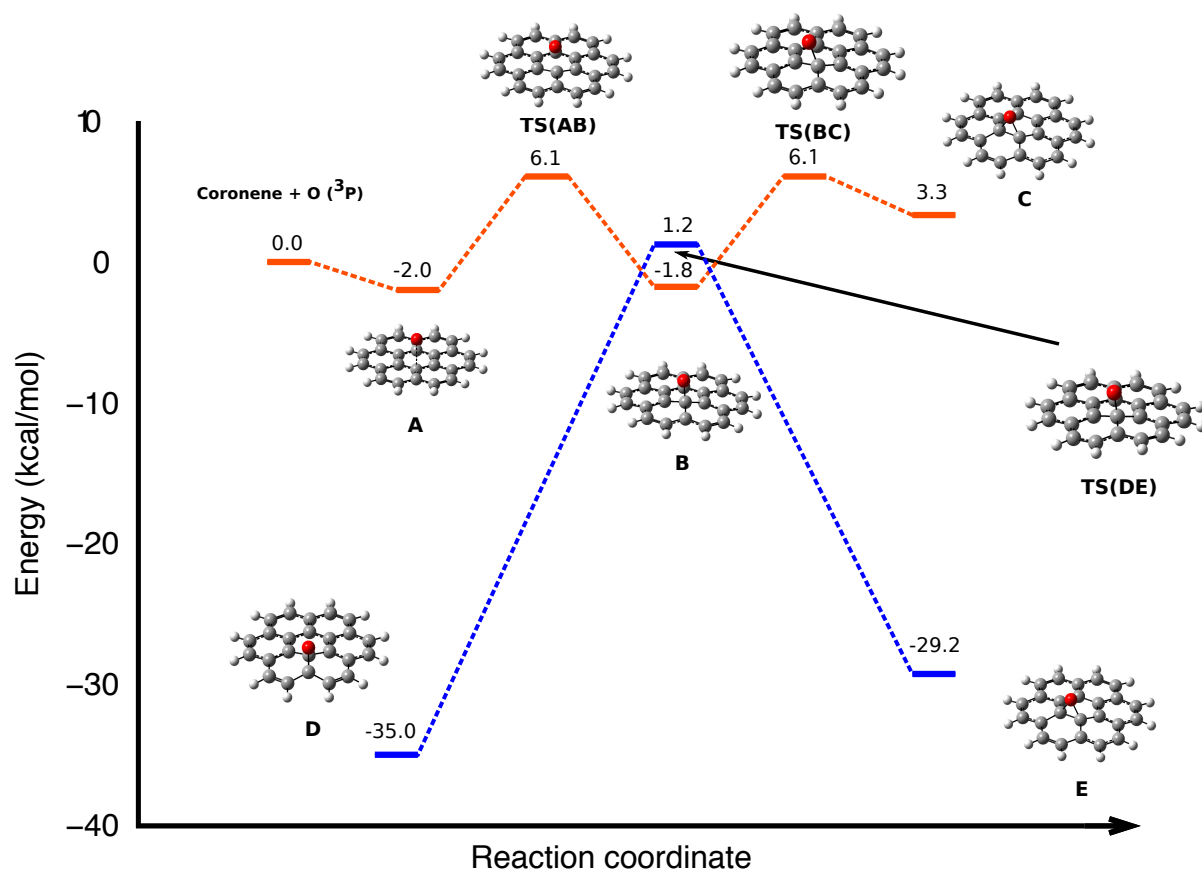


Figure 4.4 Potential energy diagram (kcal/mol) of the O addition on coronene in triplet (red) and singlet (blue) states.

Hereafter, we focus on low energy O attack in experiments, where the O does not cause defects on coronene or other graphitic surfaces. According to the potential surface in Figure 4.4, we can presume the chemisorption process of O on graphene from the atomic oxygen direct attack on the sheet. Approaching O atom in ^3P state form a precursor complex (**A**) at the distance, $r_{\text{C1-O}} = 2.67 \text{ \AA}$. After overcoming the activation barrier, 6.1 kcal/mol at $r_{\text{C1-O}} = 1.82 \text{ \AA}$, the distance between O atom and coronene is shortened to $r_{\text{C1-O}} = 1.42 \text{ \AA}$ and they form a weak coronene-O complex, **B**. The **B** is a biradical complex in triplet state with the interaction energy of -1.8 kcal/mol where the one unpaired electron is localized on O and the other unpaired electron is delocalized on the coronene (supporting information). After the formation of **B**, there are some possibilities to form epoxide form. First possible reaction

pathway is a ring closing reaction by C4-O bond formation, and the reaction yielding the epoxide form complex **C** in triplet state. Second possibility might be an intersystem crossing (ISC) from triplet state to singlet state, because the energy difference between **B** and **TS(DE)** is in a few kcal/mol and the structures of **B** is similar to the structure **TS(DE)**.

Recent theoretical studies of O (3P) + C₂H₄ reaction discovered that ISC can be occurred at the crossing point where the spin state of acetyl biradical •CH₂CH₂O• species change from triplet minimum state to open-shell singlet saddle point [170–172]. The possibility of similar spin state change in the atomic oxygen collision with graphite cluster was suggested by Ehrenfest dynamics simulation using time-dependent DFT (TD-DFT), and the distance between oxygen and the graphite model surface was ca. 1.2 Å [166], which is in the close proximity to $r_{\text{C1-O}}$ in **B** and **TS(DE)**, which might be applicable to our case.

After the ISC, ring-closing reaction can occur to form either **E** or **D**. Although we do not focus on the ISC process deeply, the final product should be dominated by **E** or **D** in singlet state because the epoxide structure in singlet state (**E** or **D**) is much more stable than in triplet state (**C**). The obtained results are consistent with the previous study which mentioned that the ground state of graphene oxide is always nonmagnetic [158].

Based on our results, we presume that the O attack on graphene yields graphene oxide dominated by epoxy functional groups since formation of the weakly adsorbed O atom on "top" site of graphene in triplet state can readily undergo migration to "bridge" in singlet state because of the significant energy difference among those states where the latter is much lower.

4.3.2 PBE and DFTB2 calculations of the interactions of oxygen with coronene

We performed the single point calculations and evaluated relative energies by

pure functional, PBE, and DFTB to assess the performance of both approaches. We employed UPBE/cc-pVDZ level of theory and spin-polarized DFTB2 level of theory based on the geometries in triplet state obtained by UB3LYP/cc-pVDZ level of theory. The obtained PECs of the interaction of O and coronene by DFT are shown in Figure 4.5 and the energies are listed in Table 4.1.

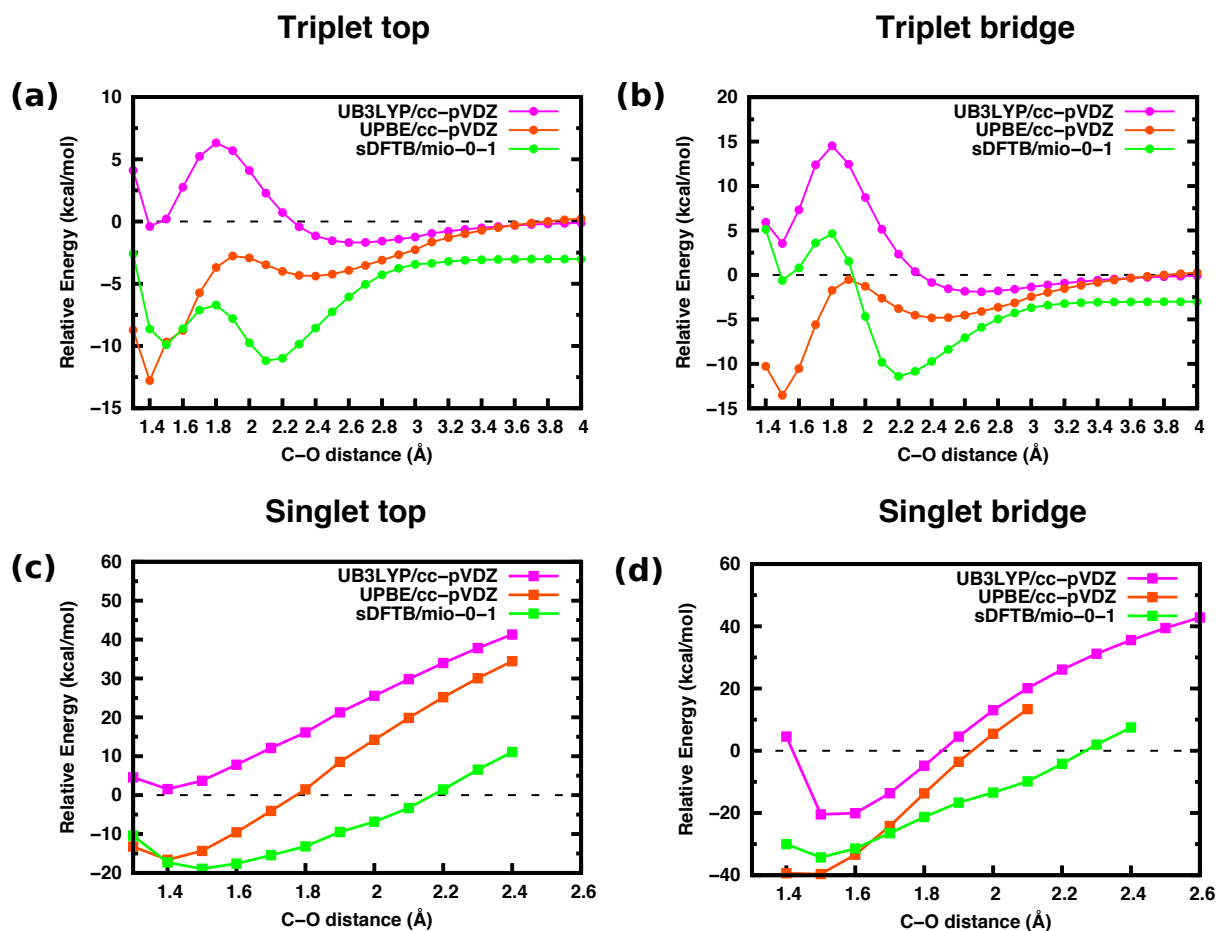


Figure 4.5 PECs of the atomic O attack on coronene calculated at various DFT level of theory. (a) Triplet state “top” attack site. (b) Triplet state “bridge” attack site. (c). Singlet state “top” attack site. (d) Singlet state “bridge” attack site.

Table 4.1 Interaction energies (in kcal/mol unit) obtained at various levels of theory. The interaction energies of optimized geometries are shown in parentheses.

Method	Relative energy minimum			Barrier	vdW
	“top”	“bridge”		“top”	“top”
	Triplet	Singlet	Triplet	Triplet	Triplet
B3LYP/cc-pVDZ	-0.4	-20.4	3.5	6.3	-1.8
PBE/cc-pVDZ	-12.8	-39.6 (-48.0)	-13.5 (-14.4)	-2.8	-4.7
sDFTB2/mio-0-1	-9.9	-34.3 (-42.2)	-0.6 (-1.5)	-6.7	No vdW

From the triplet state, the minimum calculated from UPBE/cc-pVDZ is lower than the value obtained from UB3LYP/cc-pVDZ as shown in Figure 4.5(a) and (b). This trend is similar with the trend obtained from coronene-F case. The interaction energy in vDW complex is -4.7 kcal/mol computed by PBE/cc-pVDZ, and ca. 3 kcal/mol lower than the energy at B3LYP/cc-pVDZ level of theory while in the case of DFTB2, no small vDW energy was observed at the vDW complex of B3LYP. For DFTB2, there is a large minimum around $r_{C-O} = 2.1 \text{ \AA}$. This interaction energy could not be considered as vDW energy since the geometry is closer to the geometry of the entrance transition state **TS(AB)**, instead, it is an unphysical local minimum artifact as experienced in “top” site attack of F on coronene presented in previous chapter, due to lack of short-range C-O repulsive.

The energy lowering is observed for the “top” site energy of coronene-O adduct and the “top” site entrance channel barrier, as the interaction energy and the entrance barrier is lower by 13.1 and 9.1 kcal/mol to -12.8 and -2.8 kcal/mol, respectively. In comparison with the DFTB2 value, DFTB2 calculation shows that the minimum of “top” site for triplet state adsorption and the entrance barrier are -9.9 kcal/mol and -6.7 kcal/mol, respectively. For the case of “bridge” site, similar trends appear where the lowest relative energy was obtained

for PBE, and the DFTB2 relative energy was between the PBE and B3LYP as shown in Figure 4.5(b).

For the case of singlet state, the energy lowering from the PBE and DFTB2 levels of theory were also observed in the case of the minimum from “top” and “bridge” site as shown in Figure 4.5(c) and (d), respectively as compared to B3LYP PECs. Since the “top” site attack in singlet state minimum is a transition state of the adjacent bridge site migration, these PECs would not be discussed further. PEC for singlet state “bridge” site adsorption shows that the interaction energy computed at PBE level of theory is much lower by ca. 20 kcal/mol to -39.6 kcal/mol than the interaction energy computed at B3LYP level of theory with -20.4 kcal/mol. Performing full geometry optimization for coronene-O adsorption at “bridge” site for singlet state using PBE/cc-pVDZ level of theory yields the binding energy ($-E_{rel}$) of 48.0 kcal/mol. The value “bridge” site singlet adsorption calculated from PBE/cc-pVDZ level of theory is comparable with previous theoretical periodic PBE planewave calculation [158] where the binding energy is 41.4 kcal/mol for single O adsorption in 5×5 graphene supercell and 44.2 kcal/mol for single O adsorption in 7×7 graphene supercell. As for DFTB2, the “bridge” site binding energy for singlet state is 34.3 kcal/mol, respectively. Fully optimized “bridge” site adsorption of coronene-O at C-O distance around 1.4 Å DFTB2 results in the binding energy of 42.2 kcal/mol. From this results, coronene is a proper model for oxidation of graphene.

In general, the value of interaction energy calculated from DFTB2 is lower than the value obtained from B3LYP/cc-pVDZ but higher than the value calculated from PBE/cc-pVDZ. DFTB2 binding energy value tends to be more toward to PBE value due to lack of the three-body interaction, that is only implicitly included in the DFTB Hamiltonian.

This problem can be corrected by adjusting the short-range C-O repulsive as in the case of C-H repulsive potential in coronene-H system [173] and C-F as shown in section 3.3.7. However, tuning the C-O repulsive potential for the coronene-O case is more complicated because the system can exist in two states, namely singlet and triplet states. At present, we already attempted to fit the new C-O repulsive only in triplet state using similar algorithm as described in section 3.3.7, also using the definition of formation energy. The details will be published elsewhere.

4.3.3 Interactions of atomic nitrogen and coronene computed at various DFT levels of theory

PEC from B3LYP/cc-pVDZ displayed in Figure 4.6(a) shows that there is an entrance barrier of direct attack to the “bridge” site at $r_{C-N} = 1.8 \text{ \AA}$ with the interaction energy of 36.2 kcal/mol. Similar to the case of coronene-O entrance barrier to “bridge” site, this entrance barrier is a second order transition state. The interaction energy values for quartet and doublet state from the PEC minimum ($r_{C-N} = 1.8 \text{ \AA}$) are 31.5 and 8.2 kcal/mol, respectively.

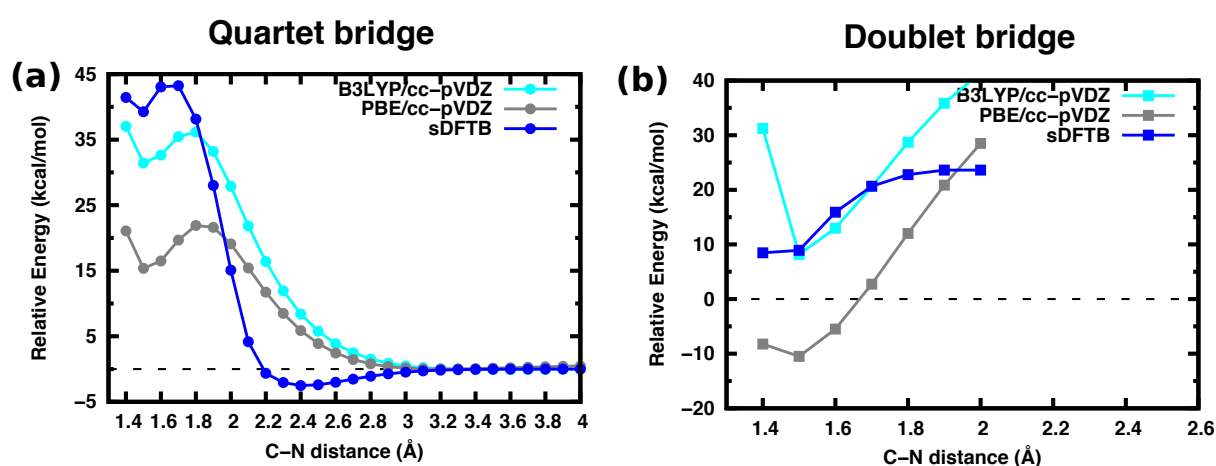


Figure 4.6 PEC of “bridge” site N adsorption on coronene calculated at various DFT levels of theory at “bridge” site (a) quartet and (b) doublet state.

The properties of coronene-N at PEC minimum are listed in Table 4.2. Full

optimization of coronene-N product at B3LYP/cc-pVDZ level of theory will decrease the interaction energy to 31.3 and -6.9 kcal/mol for doublet and quartet state, respectively. The more positive interaction energy indicates that N atom binds weaker to coronene at “bridge” site in quartet state.

Table 4.2 Interaction energies and selected bond length of the PEC minimum of coronene-N from various levels of theory. Numbers in parentheses are the interaction energy and bond length of the optimized geometries.

Method	Interaction energy (kcal/mol)		r_{C-N} (Å)		r_{C1-C4} (Å)		
	Minimum		Barrier				
	doublet	quartet	quartet	doublet	quartet	doublet	quartet
B3LYP/cc-pVDZ	8.2	31.4	36.2	1.50	1.5	1.49	1.49
	(-6.9)	(31.3)		(1.41)	(1.52)	(2.12)	(1.49)
PBE/cc-pVDZ	-10.5	15.4	21.9	1.50	1.5	1.49	1.49
	(-22.1)	(14.4)		(1.41)	(1.52)	(2.09)	(1.50)
sDFTB2/mio-0-1	8.5	39.2	43.2	1.50	1.5	1.49	1.49
	(-2.9)	(37.8)		(1.42)	(1.46)	(1.65)	(1.52)

Adsorption of N in doublet state will induce C1-C4 bond breaking for coronene while for quartet state the C1-C4 bond remains intact. The C-N bond length at optimized geometry for doublet state is 1.40 Å and C1-C4 bond length is 2.01 Å. The results of optimized geometry is not in good agreement with the recent periodic PBE calculation of atomic N adsorption on graphene [167]. However, they used a rather large supercell with 48 and 96 atoms of C atoms, so probably coronene is too small for modeling N adsorption on pristine graphene for doublet state without breaking C-C bond. To confirm this, we performed full geometry optimization

of N adsorption to a larger model, namely circumcoronene ($C_{54}H_{18}$) at “bridge” site. The results are the C-N and C1-C4 bond length are 1.47 and 1.55 Å, respectively and the interaction energy is -3.5 kcal/mol. The interaction energy is higher than the interaction energy obtained by Rani *et al.* They found that the “bridge” site interaction energy is -0.92 eV or \sim -21.3 kcal/mol. However, they used the PBE functional that usually has lower interaction energy compared to B3LYP. Full optimization of coronene-N at doublet state using PBE functional also causes the C1-C4 bond to break and the binding energy is 22.1 kcal/mol but optimizing the circumcoronene-N system using PBE results the binding energy of 20.1 kcal/mol, which is in close agreement to the value obtained by Rani *et al.* They also show that the graphene becomes magnetic upon the introduction of single N atom with the moment magnet of $0.73 \mu_B$ that is close to the doublet state where 1 electron is delocalized to the system, confirming doublet state is the stable ground state for the minimum.

For DFTB2, the “bridge” site coronene-N interaction energy is higher than the value obtained from B3LYP/cc-pVDZ with 8.5 and 39.2 kcal/mol for doublet and quartet state, respectively while the barrier energy is 43.2 kcal/mol. Full optimization of the “bridge” site minimum yields the decrease of binding energy to -2.9 and 37.2 kcal/mol for doublet and quartet state, respectively. The PEC calculated at DFTB2 level of theory shows that there is a small minimum around 2.4 Å C-N distance. At this point what we can suggest for the discussion is that the C-N repulsive energy is too high at the short range but the repulsive is not repulsive enough at the value close to the cutoff for describing the total energy on this system. The C-N parameter was fitted to some small organic molecules [4], therefore, probably the repulsive is not suitable for this system. For the DFT methods, coronene is too small to model the N adsorption on graphene. Therefore, for future method development,

circumcoronene will be used as the model of N adsorption on graphene.

4.3.4 Interaction energies on the dissociation limit of the coronene-O and coronene-N

PECs

Table 4.3 Charge on O (e) and interaction energy in triplet state at 50 Å C-O distance separation.

Method	Interaction Energy (kcal/mol)	Charge on O
B3LYP/cc-pVDZ	0.0	0.00
PBE/cc-pVDZ	0.8	0.00
sDFTB2/mio-0-1	-3.6	-0.120

As summarized Table 4.3, the PEC of coronene-O calculated at B3LYP/cc-pVDZ and PBE/cc-pVDZ in triplet state leads to correct interaction energy of the dissociation limit which is close to 0 kcal/mol. The ground state energy of dissociation limit is related to the orbital energy levels of the interacting species. If the highest occupied orbital energy level of an electron donor is higher than lowest unoccupied energy level of an electron acceptor, the artifact charge transfer can be caused even at the separated distance due to the delocalization error of electrons [135]. In the case of coronene-O, coronene and O are supposed to be a donor and an acceptor, respectively. In present case, the HOMO donor will be the π orbital of coronene and the acceptor is the empty β 2p orbitals, dubbed as lowest unoccupied atomic orbital (LUAO). In the O case, there should be two LUAOs 2p orbitals. As illustrated in Figure 4.7, calculations at the B3LYP/cc-pVDZ level of theory show that the HOMO energy level in coronene is -5.63 eV, while the LUAO energy level in O (3P) is -4.35 eV and PBE/cc-pVDZ level of theory show that the HOMO energy level in coronene is -5.11 eV, while the LUAO energy level in O (3P) is -5.71 eV. These LUAOs are degenerate. Therefore,

the relative energy levels of the HOMO and the LUAO from B3LYP calculation indicate the impossibility of the artificial charge transfer; while for PBE there is a possibility of charge transfer to O atom, but at very large C-O distance, the charge transfer on O is not observed.

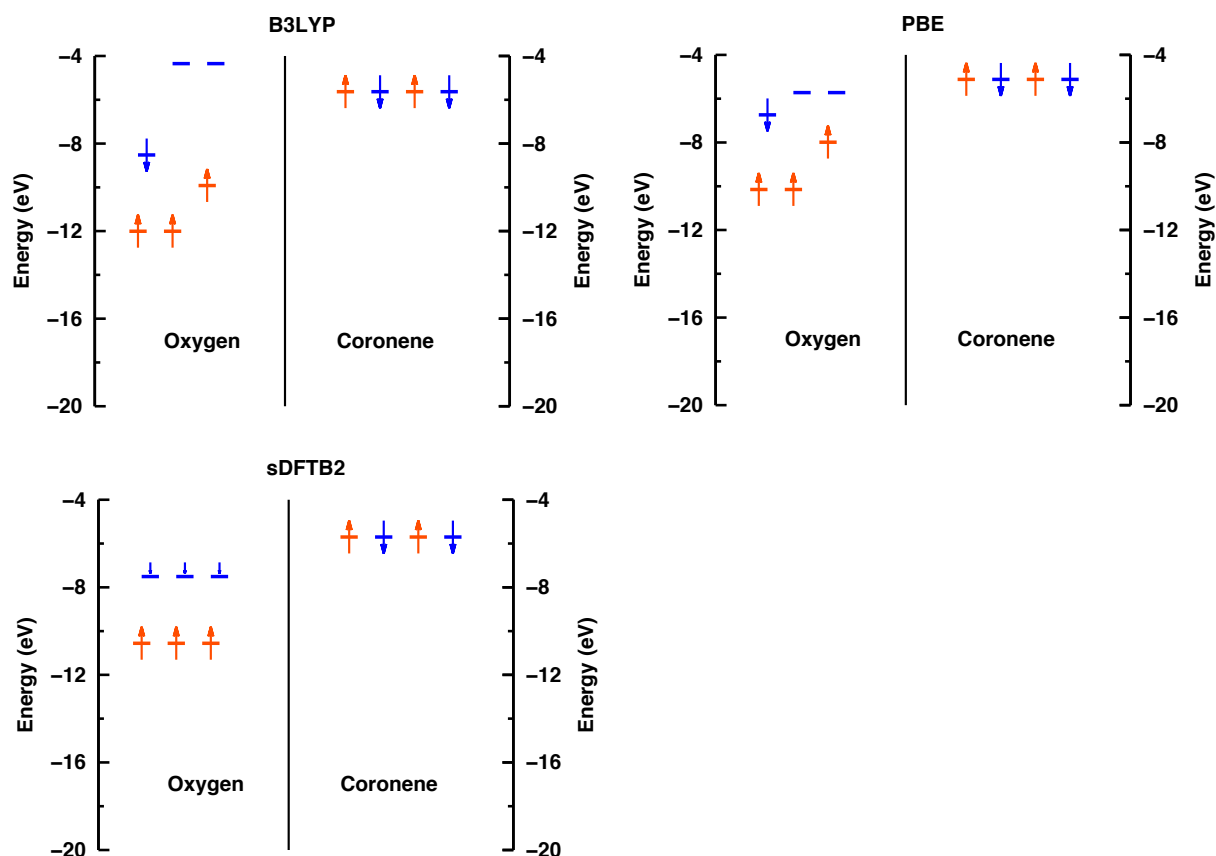


Figure 4.7 Coronene HOMO and oxygen highest occupied and lowest unoccupied 2p atomic orbital energies calculated separately from each other at selected DFT levels of theory. Red arrows indicate α electrons, blue arrows indicate β electrons. All DFT calculations employed the cc-pVDZ basis set while sDFTB calculations employed the mio parameters. In the sDFTB theory, the use of fractional occupation numbers results in an occupancy of 1/3 β electrons in the β 2p shell, as indicated by “shorter” blue arrows.

In the case of sDFTB2 level of theory, the interaction energy of the dissociation limit does not converge to 0 kcal/mol. The coronene and O dissociation limit is ca. -3 kcal/mol. This means that the HOMO level of coronene (-5.68 eV) is higher than the LUAO level of O (-7.51 eV) of coronene and the artificial charge transfer can occur at “infinite” C-O distance. In the DFTB case, For instance, the distance between coronene O is even 50 Å, O

atom has still $-0.120e$ charged (see Table 4.3).

Table 4.4 Charge on N (e) and interaction energy of quartet state at 50 Å C-N distance separation.

Method	Interaction Energy (kcal/mol)		Charge
B3LYP/cc-pVDZ	0.0		0.00
PBE/cc-pVDZ	0.0		0.00
sDFTB2/mio-0-1	0.0		0.00

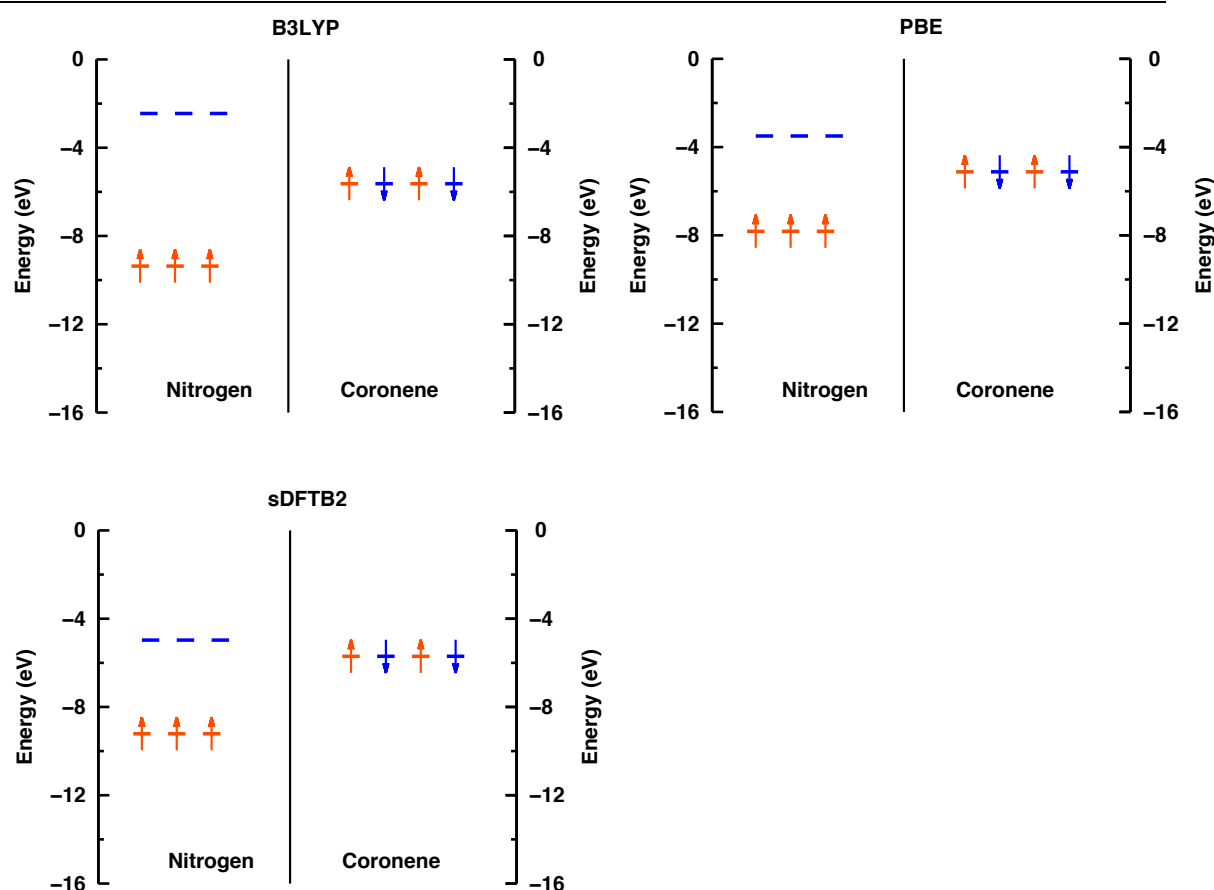


Figure 4.8 Coronene HOMO and nitrogen highest occupied and lowest unoccupied 2p atomic orbital energies calculated separately from each other at selected DFT levels of theory. Red arrows indicate α electrons, blue arrows indicate β electrons. All DFT calculations employed the cc-pVDZ basis set while sDFTB calculations employed the mio parameters.

In contrast with coronene-O results, the interaction energy dissociation limit of coronene-N computed using all methods employed in present works converge to 0 kcal/mol

as listed in Table 4.4. Although B3LYP/cc-pVDZ and PBE/cc-pVDZ level of theory predicts the correct dissociation limit since the HOMO of coronene is lower than the LUAO of quartet N, it is quite surprising that DFTB2 level of theory can predict the correct HOMO – LUAO energy ordering, as illustrated in Figure 4.8, preventing the artificial charge transfer from coronene to nitrogen. This also means that the delocalization error for N is in a lesser extent compared to O and F at DFTB level of theory.

We would like to focus on the discussions to the trends of the LUAO energy level of the atoms in the context of DFTB method. In Chapter 3, we already showed the poor performance of DFTB for the coronene-F reaction. In DFTB, the problem is caused by the severe charge transfer experienced by F atom. This is because of the LUAO of β 2p of F atom is much lower than the HOMO of coronene. In this chapter we showed a trend that compared to F, O still experienced a charge transfer but not as severe as the case of F. On the other hand, N does not experience the charge transfer problem. The cause of this problem is the limitation of DFTB to describe the spin-polarized orbital. In the case of F and O, we can say that both the highest occupied atomic orbital (HOMO) and the LUAO are *degenerate* for the β orbital, shown by the fractional occupation number. In fact, based on our results, increasing the number of electron in the 2p orbital will have lower 2p orbital energy level. The β 2p energy level in F is lower than the 2p energy level in O, since the β 2p shell of F has 2 electrons and β 2p shell of O has 1 electron. For DFTB method, the occupied orbital with same angular momentum in each AO is degenerate for each spin-orbital, further reducing the energy of the β LUAO. This is not experienced in N, with no occupied β LUAO. Thus, the LUAO energy level is the highest among other most electronegative atoms.

4.4 Summary

We theoretically proposed a possible attack and chemisorption mechanism of O on coronene as a model of graphitic material based on the PECs calculated by DFT at "top" and "bridge" sites on coronene. We confirmed that the stable spin state of coronene – O system is triplet state at far C-O distance, while the stable spin state is singlet state in the coronene-O binding region. We proposed that O attack on the coronene starts in triplet state at "top" site with the energy barrier, 6.1 kcal/mol, and ISC occurs with smooth O migration in order to form stable epoxide structures in singlet state with the interaction energy of -29.2 kcal/mol or -35.0 kcal/mol.

DFTB2 level of theory benchmark PECs calculations results show that the value of interaction energies calculated from DFTB2 is lower than the value obtained from B3LYP/cc-pVDZ but higher than the value calculated from PBE/cc-pVDZ. In contrast with the coronene-F case, the interaction energy of the dissociation limit for the coronene-O case approach closer to zero kcal/mol. There is a possibility to fit the short-range C-O repulsive with the energy obtained in B3LYP level of theory.

We have performed DFT-based PECs for interaction of nitrogen on coronene molecules in their centers at "bridge" site. The purpose of the study was to evaluate the trend of binding energy and dissociation limit energy of the theoretical methods employed compared to adsorption of fluorine and oxygen with coronene as a model of graphitic material. Similar to the coronene-O case, there are two possible spin states which are doublet and quartet. Coronene – N system is more stable in the quartet state at far C-N distance, while in the coronene-N binding region, the system is more stable in the doublet state. Binding energy calculated using PBE/cc-pVDZ level of theory is lower than the binding energy

calculated using B3LYP/cc-pVDZ and DFTB2 level of theory. On the other hand all of the methods employed predict correct dissociation limit to be ~ 0 kcal/mol. The delocalization error for nitrogen is in a lesser extent compared to oxygen and fluorine

Chapter 5 Long-Range and Short-Range Zr–Zr DFTB2 Repulsive Potential for Interaction in Bulk Zirconium

5.1 Introduction

It is mentioned in the introduction part of this thesis that we are interested in the simulation of YSZ systems. In this chapter, we report the strategy of development of repulsive potential for Zr – Zr. The repulsive potential parameterizations of Zr – Zr are the first step for extending the complete set for YSZ systems and its interaction will strongly affect the rest of the potential. We address different scheme of parameterization and their behavior will be discussed. The resulting Zr – Zr parameters will be used to make the complete Zr – X parameters.

5.2 Parameterization procedures and computational details

DFTB2 parameterization for the electronic parts have been previously done by Nishimura in his doctoral works [69]. The confining potential for the orbitals has been determined to generate the Hamiltonian and overlap matrix elements that reproduce valence and low-lying conduction bands of Perdew-Burke-Ernezhoff (PBE) [24,25] functional with projected augmented wave (PAW) [174] basis electronic band structure for hexagonal closed pack (HCP) crystal structure using the automatized DFTB parameterization code [71] based on particle swarm optimization (PSO) [70] algorithm (the confining potential is shown in Appendix A). He showed that the electronic parameters based on our automatic DFTB PSO code could reproduce accurate band structure up to 5 eV above Fermi level from PBE band structure for all elements in periodic table except for *f*block [69].

PSO is one of the methods for stochastic optimization. It solves a problem by spreading the so-called candidate solutions, also known as particle over a searching space. The

particle will move toward the global minimum according to the certain algorithm.

For the parameterization of the repulsive potentials, we calculated total energy from PBE exchange-correlation functional with PAW basis as the reference for DFT level. We devised a strategy to create DFTB repulsive potential especially for metal-metal interaction in solids states.

The first attempt was a “hand-made” repulsive parameter as in the traditional DFTB repulsive parameterization. In this parameterization, we employed semi-manual parameterization using mostly by hand and using traditional DFTB parameterization philosophy: the repulsive should not go beyond second nearest neighbor so that the third and so forth neighbor interactions were neglected. Zr – Zr repulsive parameter was fitted to most stable phase at ambient condition (HCP phase). The DFT reference data were obtained by scanning reference HCP phase from approximately 70 % to 130 % volume of the DFT equilibrium geometry with approximately intervals of 5 % volume. HCP has 2 degree of freedom, namely lattice parameter a and c . In this part of this work, the c/a ratio of Zr HCP was fixed to ideal value ~ 1.633 , thus in the structure, all Zr – Zr bond lengths in the reference geometries have same distance in order to simplify the parameterization process. The repulsive potential was represented with a polynomial function using the M th order polynomial

$$V(r) = \sum_{i=m}^M c_{i-m} (r - r_0)^i \quad (5.1)$$

where m is usually 2 or greater in order to ensure the repulsive and the first derivative go to zero at the cutoff value r_0 . The value of the repulsive for the distance greater than r_0 is zero.

In the fitting procedure, the polynomial coefficient c_{i-m} is the free parameter to be adjusted

to reproduce the reference energy. The polynomial fitting and conversion to 3rd - 5th order spline for DFTB+ compatibility utilized code developed by Bodrog *et al.* [144].

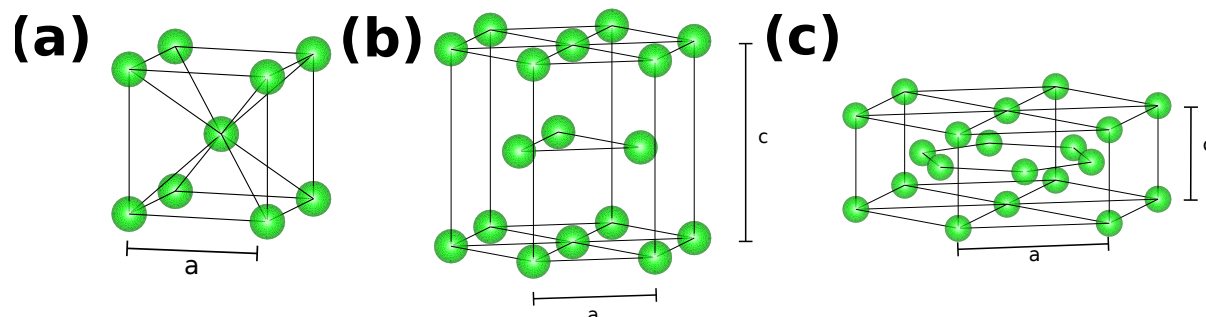


Figure 5.1 Considered unit cells for the bulk phase of Zr (a) BCC (space group $Im\bar{3}m$) (b) HCP (space group $P6_3/mmc$) and (c) ω (space group $P6/mmm$).

Next attempt was an automatic repulsive parameterization. We performed the parameterization using automatic repulsive parameterization code [175] that has been interfaced with the automatic DFTB parameterization tools [71] to fit to the repulsive part. With the automatic code, more fitting systems are applicable at the same time with less human effort. In this parameterization, we employed many training sets from all experimentally exist bulk Zr, namely HCP, body centered cubic (BCC) and so-called ω phase as shown in Figure 5.1. BCC phase of Zr occurs at higher temperature around 1130 K. The ω phase occurs from HCP phase transformation at high pressure above 2.2 GPa in the room temperature [176–178], as shown in . In general, the DFT reference were similar to those of the “hand-made” parameterization that is the total energy of each phase at stretched and compressed unit cell from approximately 80 % to 120 % volume of the DFT equilibrium geometry. The difference is that we were able to put all of the reference data into the fitting systems instead of only putting one single phase into the fitting systems. Additionally, it is also possible to put random displacement of atoms inside the unit cell and random compression or expansion of the lattice vectors into the training sets. We also played with the

cutoff value. We started by extending the cutoff of the repulsive long enough so it will be beyond first nearest neighbor and reducing it short enough. It will be shown later that at some conditions, we will have excellent agreement with the DFT reference data; but at the same time, it sacrifices some important aspects in the performances.

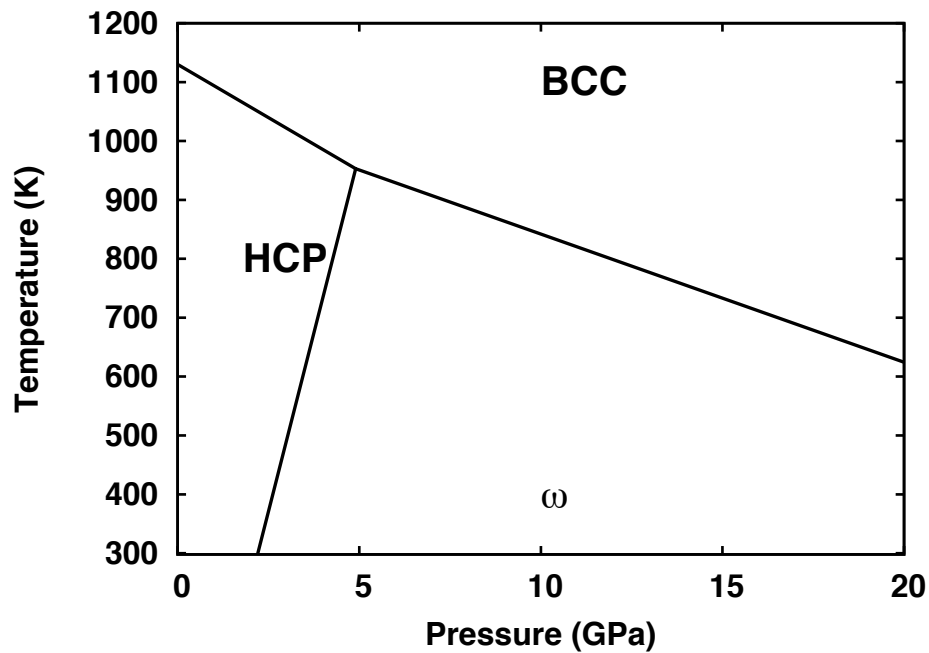


Figure 5.2 Phase diagram of bulk Zr. The phase boundary was plotted based on experimental data from refs. [176–178].

In the automatic repulsive parameterization we introduced the fitness value, following this formulae

$$fitness = MAE * 0.95 + Maximum AE * 0.05 \quad (5.2)$$

with *MAE* is the mean absolute error and *Maximum AE* is the maximum absolute error. Per definition, the fitness value determines how close is the testing set compared to training set. In this work, the target is the relative energy with respect to most stable phase i.e. HCP phase. For other fitness targets see ref. [71]. Generally, the fitness value below 0.1 in error unit can be considered as good. However, a “bad” fitness value does not mean yielding a “bad” parameter, it could mean that some training sets contribute larger error value compared

to some other training sets. Conversely, a “good” fitness value does not always yield “good” parameter since probably some systems are not included in the training sets. In this work we attempted to balance between training sets and testing sets, therefore the fitness value is merely a number and does not affect entirely to the performance of the physical systems. In the automatic parameterization, the repulsive potential is represented by 4th order spline [175] instead of traditional 3rd – 5th order spline. In the present works, the particles of the PSO are the position of the knot in the spline repulsive. The algorithm determines the best position of the knot in the spline based to have the smallest fitness value compared with the reference data.

The DFT reference calculations were performed using VASP code version 5.2 [179–182] using the PBE functional in conjunction with PAW basis [174] with cutoff energy of 550 eV. 4s²4p⁶5s²4d² electronic configuration was used Zr. The k-point sampling in the first Brillouin zone, based on the Monkhorst-Pack scheme [183], were 18 × 18 × 18 for HCP and ω, and 16 × 16 × 16 for BCC. The number of k-points and cutoff energy had been tested to obtain convergence in total energy for less than 0.5 meV/atom.

All DFTB calculations were performed using DFTB+ [125,184] program with same number of k-points as in the DFT reference. For the automatic DFTB parameterization, a modified version of DFTB+ was used that can read the 4th order spline.

All the generated Zr-Zr parameter will be used for testing purpose. The test systems are bulk Zr in the available phase diagram. Trend based on individual test systems will be discussed. This work concerns about the transferability of Zr-Zr parameter from HCP phase to BCC and ω phase and strategy to create a good quality repulsive potential especially for solid transition metal.

5.3 Results and Discussions

5.3.1 DFT testing set

DFTB parameterization results are usually compared with the equilibrium geometry, cohesive and formation energy as well as the bulk modulus from the reference, both DFT and experimental data. Since we used DFT as reference data, this section shows the results from reference DFT calculations for the validation with experimental and previous theoretical calculations.

The DFT equilibrium geometry was obtained by simultaneously optimizing the position of the atoms and relaxation of the volume of the unit cell. The high cutoff value ensures that the planewave basis is complete in order to avoid the so-called Pulay stress [185] if the volume is relaxed. The equilibrium geometry is then scaled isotropically to approximately 80% - 120% of the equilibrium volume to obtain the energy vs volume ($E - V$) curve. The $E - V$ curve is then fitted to the Birch-Murnaghan equation of state [186] (BM EOS) to obtain the bulk modulus and bulk modulus derivative. The cohesive energy was obtained by subtracting the bulk total energy with the energy of spin-polarized Zr atom where more negative value means that the bulk phase is more stable with respect to atomic detachment. For formation energy, we defined it as the relative energy between all of the phases with respect to the most stable phase (HCP). Those values from DFT are used as control for the performance of the DFTB parameters. The DFT results for structural parameter, bulk modulus and energetic properties are shown in Table 5.1. For comparison with previous theoretical calculation, we only compared to GGA based calculations since generally choice of different type of exchange-correlation functional will lead to different results and the DFTB parameters were fitted to PBE (GGA) level of theory.

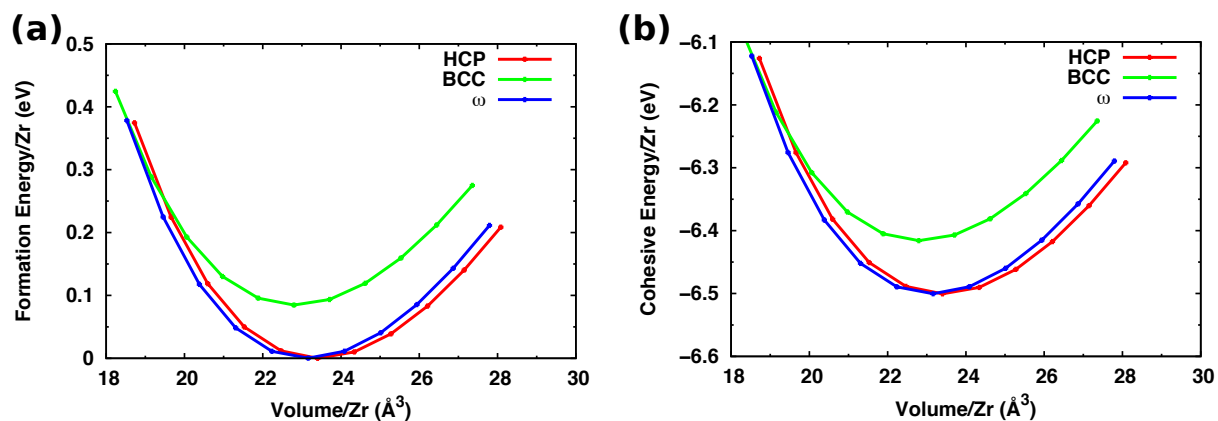


Figure 5.3 (a) Relative/formation and (b) cohesive energy vs volume per atom curve for all experimental phases of bulk Zr calculated at PBE-PAW level of theory. For formation energy, equilibrium HCP geometry energy was used as reference.

Table 5.1 Calculated DFT structural parameters, cohesive energy, bulk modulus and bulk modulus derivative from current work compared with previous GGA calculations and available experimental value.

Phase	Parameter	This work	Previous calculations	Experiment
HCP	a (Å)	3.235	3.236 ^a [187],	3.233 [177],
			3.240 [188],	3.231 [190]
			3.232 [189]	
	c (Å)	5.163	5.166 ^a [187],	5.146 [177],
			5.178 [188],	5.148 [190]
			5.182 [189]	
c/a	1.597	1.596 [187],	1.592 [177],	
		1.598 [188],	1.593 [190]	
		1.603 [189]		
	E_{coh}/Zr (eV)	-6.50	-6.19 [191]	-6.25 [192]
	E_{form}/Zr (eV)	0.00 ^b	0.00 ^b	0.00 ^b

Phase	Parameter	This work	Previous calculations	Experiment
HCP	B_0 (GPa)	93.61	91 [193], 93.4 [188], 95 [194], 96.78 [187]	94 [177], 97.6 [190], 102 [195]
	B_0'	3.317	2.25 [187], 3.22 [188]	3.10 [177], 3.10 [195]
BCC	a (Å)	3.572	3.572 [187], 3.580 [188], 3.577 [189]	3.574 [196]
	E_{coh}/Zr (eV)	-6.41	N/A	N/A
	E_{form}/Zr (eV)	0.09	N/A	N/A
	B_0 (GPa)	83.38	N/A	N/A
	B_0'	3.19	N/A	N/A
	ω	a (Å)	5.042	5.035 ^a [187], 5.056 [188], 5.050 [189]
ω	c (Å)	3.155	3.153 ^a [187], 3.150 [188], 3.150 [189]	3.136 [190]
	c/a	0.626	0.626 [187], 0.623 [188], 0.623 [189]	0.622 [190]

Phase	Parameter	This work	Previous calculations	Experiment
ω	E_{coh}/Zr (eV)	-6.50	N/A	N/A
	E_{form}/Zr (eV)	0.2×10^{-3}	N/A	N/A
	B_0 (GPa)	95.32	95.93 [187], 101.1 [188]	90 [177], 104 [176]
	B_0'	3.52	3.45 [187], 3.27 [188]	2.05 [176]

^aCalculated based on c/a ratio and volume. ^bPer definition.

As seen from Table 5.1, for HCP phase, our calculated a lattice parameter is in excellent agreement with the a lattice parameter experimental value of about 3.23 Å. On the other hand, the c lattice parameter is longer by approximately 0.017 Å compared to experimental lattice value. The trend of longer c lattice parameter is similar to previous GGA level of theory calculations where c lattice parameters are longer than experimental value by 0.02 – 0.03 Å. For ω phase, the c lattice parameter from our calculation and previous theoretical calculations is also longer than the experimental value by ~0.015 Å while the a lattice parameter is in good agreement with experimental value. For BCC phase, the geometry is in excellent agreement with previous theoretical calculations and experimental value. The bulk modulus and bulk modulus derivative obtained from BM EOS fitting are in good agreement with the experimental and previous theoretical study for all of the available data on the literature.

Now we discuss the energy ordering of the experimental phase. As shown from the E-V curve in Figure 5.3 and the value of cohesive energy in Table 5.1, we found that HCP phase is the most stable phase, followed by the ω phase with only 0.2 meV/atom higher than

HCP phase. The unstable phase is BCC phase with 0.09 eV/atom higher than HCP phase. The energy ordering is consistent with the experimental observation and the PBE-pseudopotential (PBE-PP) by Zhang *et al.* [187] and PBE-PAW by Hao *et al.* [197]. On the other hand, a different publication but also from Hao *et al.* [188] predicted the opposite trend of HCP- ω stability using also PBE-PAW level of theory. The discrepancies of results from ref. [188] and ref. [197] might be caused by the difference in their geometry. As seen in Table 5.1, the c lattice parameter for HCP phase from Hao *et al.* in ref. [188] is longer by 0.015 Å than our lattice parameter, therefore the HCP from Hao *et al.* in ref [188] results could be less stable than our results. However, in ref. [197] the value of the lattice parameters are not explicitly mentioned and the calculations were performed in a supercell instead of small unit cell, which probably causes the discrepancy. Given that our geometries resemble the geometries from Zheng *et al.*, we might say that our results are reliable since Zheng *et al.*'s results are also comparable with experimental and other theoretical studies [193,194]. Also, in both cases where ω phase is more or less stable, the energy difference between both phases is below 0.5 meV, which is probably beyond the accuracy of DFT level of theory, therefore both phases could be considered as a degenerate phase. Nonetheless, we could use our DFT results as the reference for DFTB performance.

5.3.2 DFTB2 results

This section is devoted to discuss the detailed method and results of the parameterization of the polynomial fitted (“poly”) and the automatic generated (“PSO”) repulsive potential.

5.3.2.1 Polynomial fitted repulsive potential

The repulsive was obtained by fitting the energy – distance curve by taking

equality between reference (DFT) energy and DFTB energy i.e.

$$E_{DFT}(r) = E_{DFTB}(r) \quad (5.3)$$

where $E_{DFT}(r)$ and $E_{DFTB}(r)$ are total energy from DFT and DFTB, respectively at certain geometry with bond length r . With the definition of E_{DFTB} , in this case for HCP we obtain

$$\begin{aligned} E_{DFTB}(r) &= E_{el}(r) + E_{rep}(r) \\ &= E_{el}(r) + 6V_{rep}(r) \end{aligned} \quad (5.4)$$

where factor 6 comes from the coordination number of Zr in HCP divided by 2 to avoid double counting. The repulsive energy can be determined by subtracting total DFT energy with DFTB electronic energy as in the conventional parameterization scheme [45]. We can rearrange Eq.(5.3) and (5.4) to obtain the expression for pairwise repulsive potential $V_{rep}(r)$

$$V_{rep}(r) = \frac{[E_{DFT}(r) - E_{DFT}(r_{ref})] - [E_{el}(r) - E_{el}(r_{ref})]}{6} + V_{rep}(r_{ref}) \quad (5.5)$$

where r_{ref} is a reference geometry, in this work, the fully optimized geometry from DFT level of theory. The term $V_{rep}(r_{ref})$ is the repulsive potential at the reference geometry. Its value, however, can be arbitrary to be fitted to the atomization/cohesive energy [66]. In this work, we didn't pay attention to the accuracy of cohesive energy (i.e. total energy of the bulk subtracted with atomic energy) since in DFTB, the atomic total energy is not well defined due to compressed orbital and lack of repulsive potential. It is also known for its overbinding problem [54]. Therefore, the accuracy of cohesive energy was sacrificed to obtain better agreement with the geometry. Theoretically, a good electronic parameter should have the electronic energy parallel to total DFT at some point where at that point, the potential can vanish to zero and where the cutoff is. However, as seen in Figure 5.4, the electronic energy becomes parallel with total DFT energy after approximately 9 bohr (~ 4.76 Å), which is almost close to second nearest neighbor Zr – Zr distance.

With that condition, the Eq. (5.4) and (5.5) will not be applicable if the repulsive cutoff is determined to be greater than 9 bohr since additional terms must be included from second nearest neighbor contribution. Since we restricted the repulsive potential so that the second nearest neighbors do not contribute, we have to set the cutoff before 9 bohr.

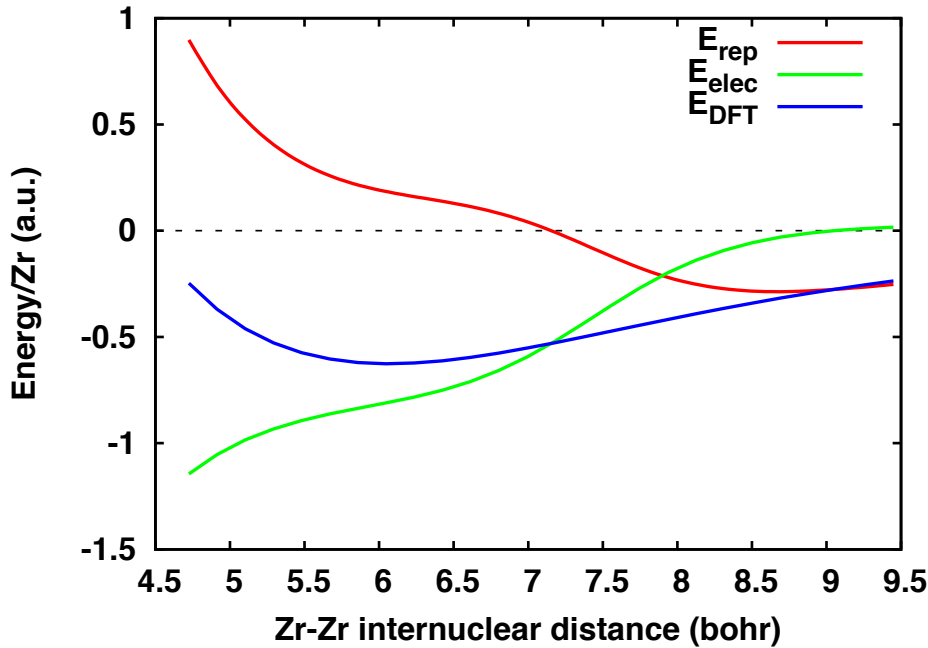


Figure 5.4 Zr-Zr repulsive potential fitting curve. The fitting system is bulk Zr in HCP phase with ideal value of c/a of 1.633. E_{DFT} is the total shifted DFT energies, E_{elec} is the DFTB electronic energy corresponding to DFT geometry and E_{rep} is difference between two curves. E_{rep} in this curve is not the final outcome for the Zr-Zr repulsive energy.

We examined that around 6 to 6.5 bohr is the safe distance where to put the cutoff value and force the repulsive potential to zero. First consideration is that we have the training set starts from 4.72 bohr (2.5 Å), which mean that the second nearest neighbor from that training set is around 6.67 bohr (3.5 Å), the cutoff value should be before that value. Second consideration is that in that region, the potential is less steep than the potential after 6.67 bohr (see Figure 5.4), so it will be easier to force the repulsive to zero at that region. After several trial attempts, we obtained that the optimum polynomial degree is 9 with $m = 3$ and the cutoff radius is 6.15 bohr to describe reasonable HCP geometry of bulk Zr. This repulsive potential

is shown in Figure 5.5.

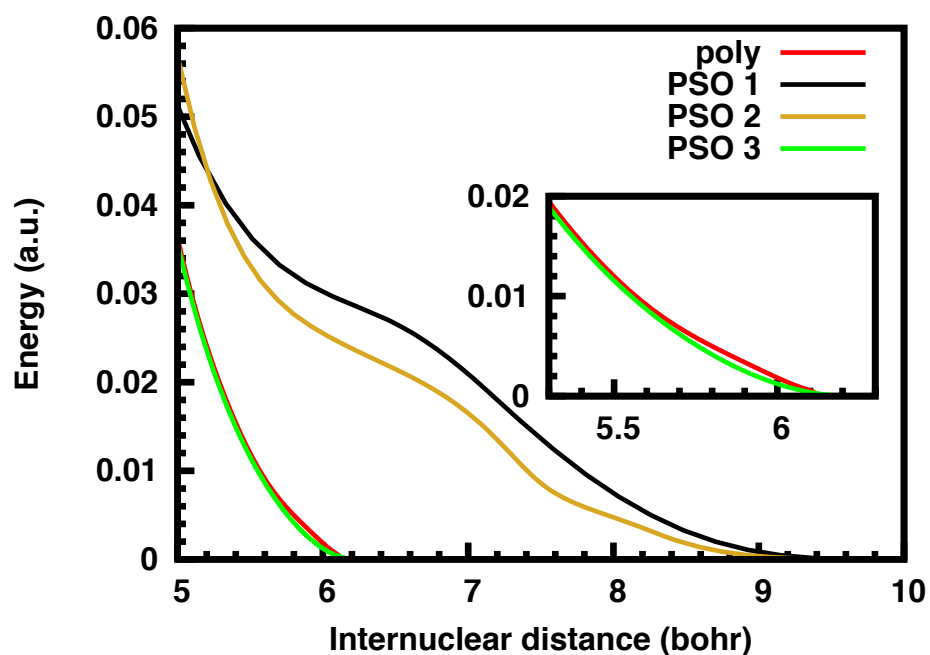


Figure 5.5 Generated Zr-Zr repulsive potential from the polynomial fitted (“poly”) and PSO generated (“PSO”) parameterization.

Structural parameter, cohesive energy, bulk modulus and bulk modulus derivative of the three phases obtained using the hand-made potential are shown in Table 5.2. For locating the equilibrium geometry, as in the DFT calculations, position of atoms and the lattice parameters were optimized simultaneously using default criteria of force convergence in DFTB+. The bulk modulus and bulk modulus derivatives were also fitted using BM-EOS.

Table 5.2 Bulk properties of Zr obtained using polynomial fitted repulsive potential.

Polynomial fitted DFTB2 potential		
HCP	a (Å)	3.244
	c (Å)	5.219
	c/a	1.609
	E_{coh}/Zr (eV)	-10.69
	E_{form}/Zr (eV)	0.00
	B_0 (GPa)	215.07
	B_0'	-3.80
BCC	a (Å)	3.495
	E_{coh}/Zr (eV)	-10.67
	E_{form}/Zr (eV)	0.02
	B_0 (GPa)	125.13
	B_0'	3.38
ω	a (Å)	4.984
	c (Å)	3.005
	c/a	0.602
	E_{coh}/Zr (eV)	-10.73
	E_{form}/Zr (eV)	-0.04
	B_0 (GPa)	227.66
	B_0'	1.31

Structure of HCP phase obtained using the hand-made potential are fairly in good agreement with experiment and PBE calculation. The lattice parameter a is 0.01 Å longer

than both experimental and PBE value whereas the lattice parameter c is overestimated by 0.06 \AA and 0.08 \AA to PBE and experimental value respectively. With the hand-made set, c/a ratio is slightly higher with 1.609 compared to PBE and experimental value with 1.597 and 1.592 , respectively. Although not directly comparable, similar trend of lattice parameter value overestimation for the HCP phase are also present in the case of DFTB2 calculations of bulk Ti from *tiorg* [55] set and bulk Zn from *znorg* set [54] which could mean that DFTB tends to overestimate one or two lattice parameters in HCP phase. For BCC and ω phase, since these phases were not taken into account in the reference data, the description of those phases could become the additional advantage for the hand-made parameter if the results are satisfactory. BCC lattice parameter a value is shorter than PBE and experimental lattice parameter within 0.08 \AA . For ω phase, in contrary with results from HCP, both lattice parameter a and c values are shorter compared to the PBE and experimental results. a and c are shorter by ~ 0.05 and $\sim 0.15 \text{ \AA}$, respectively, consequently, the c/a ratio is lower than the reference value. Nonetheless, for our case, our hand-made parameter is quite satisfactory to describe the geometry of the most stable phase of Zr that is used as repulsive potential reference as well as the BCC phase.

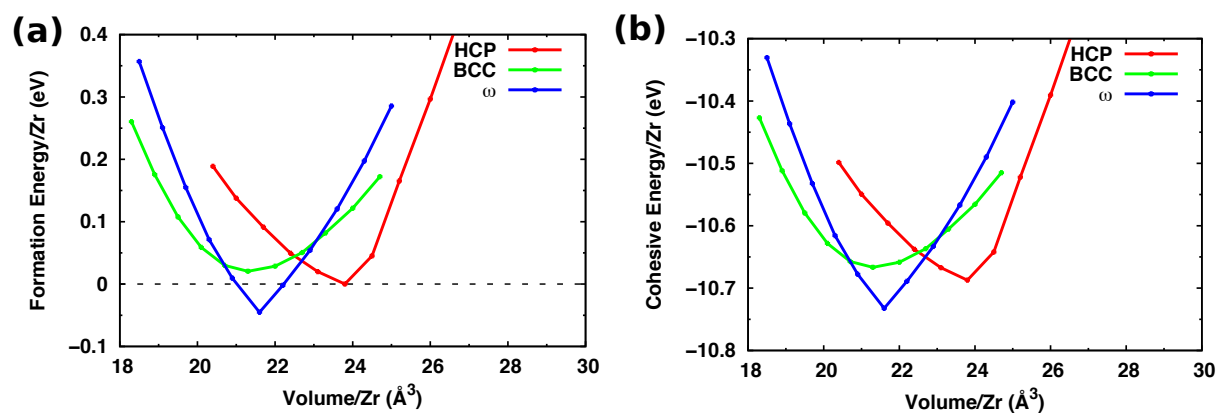


Figure 5.6 (a) Relative/formation and (b) cohesive energy vs volume per atom curve for all experimental phases of bulk Zr obtained using the polynomial fitted repulsive potential. For formation

energy, equilibrium HCP geometry energy was used as reference.

Now, we discuss the energetic properties. The cohesive energy of HCP phase is lower by approximately 4 eV compared to PBE and experimental value. This underestimation is not surprising since the DFTB has the tendency to overestimate the binding energy. However, the high value of cohesive energy could mean that the wave function is strongly compressed; therefore the orbital energies of the bulk phase are smaller than the supposed value. BCC phase is higher in cohesive energy by 0.02 eV with -10.69 eV/atom while ω phase cohesive energy is lower than HCP cohesive energy with -10.73 eV/atom. Despite the inaccuracy of the formation and relative energy, the “poly” repulsive potential could reproduce the correct energy ordering of HCP and BCC phase as in the reference DFT calculations, while the ω phase is more stable than HCP phase, in contrast with experimental and DFT observation.

The calculated bulk moduli of all three phases from “poly” repulsive potential are generally too high compared to the DFT and experimental value. As seen in Figure 5.6, the E – V curves are very steep compared to the DFT curves. This is due to non-coverage of the Zr-Zr bond by the repulsive potential. We set the repulsive potential to 6.15 bohr, which is near the equilibrium Zr-Zr bond length in HCP phase. We can correct the error in the bulk modulus by extending the repulsive potential longer close to second nearest neighbor distance as will be shown in next section.

At this stage, our “poly” repulsive potential is able to describe correct geometry and energy ordering for HCP and BCC phase within DFTB accuracy.

5.3.2.2 PSO repulsive potentials

In order to possibly improve the DFTB results, we performed the repulsive

parameterization using the PSO code. In this section we considered 3 of the best repulsive potentials based on their performances, either in geometry or the energetic from the PSO parameterization, namely “PSO 1”, “PSO 2” and “PSO 3”. Here, we specify the repulsive potentials based on their training sets and creation methods. All of the repulsive potentials are shown in Figure 5.5.

At first, we just simply wanted to reproduce DFT energy curve with the PSO parameterization. Based on the experience in the “hand-made” parameterization, the repulsive has to be extended long enough in order to cover all of the Zr-Zr bonds in the training set, regardless of the phase. Hence, we created the “PSO 1” repulsive potential using the training set of isotropically scanned 3 experimental phases from approximately 80% to 120% of the equilibrium volume, which is also the geometry as in DFT test set. About 30 data points were fitted. The potential has cutoff radius of 10 bohr in order to ensure the bond coverage of all 3 phases and number of the knots are 6. The spline part of “PSO 1” starts at 5 bohr.

Figure 5.7 shows the “PSO 1” E – V curve of the 3 phases of zirconium computed at DFT geometry. It is shown that the long range “PSO 1” repulsive potential is able to reproduce perfectly the DFT training set. This can be characterized by the value of bulk modulus B_0 which has the error less than 5 GPa for all three phases and the fitness value of 0.03. The energy difference of each phase can also be reproduced with the great accuracy and the energy ordering of the three phases is also correctly reproduced. HCP – BCC energy difference is 0.083 eV/atom that agrees well with DFT result, while energy difference of HCP and ω phase is 0.010 eV/atom, which is higher than DFT value. Nevertheless, the DFTB energy difference of HCP and ω phase is still in accuracy of DFTB, where probably the DFT

reference energy is hard to reproduce in DFTB.

The cohesive energy is also improved compared to the “poly” repulsive The cohesive energy for HCP phase is -5.76 eV/atom, higher than DFT value and experimental value by 0.8 and 0.5 eV, respectively. This is due to repulsive nature of the potential around the DFT equilibrium bond length of HCP phase.

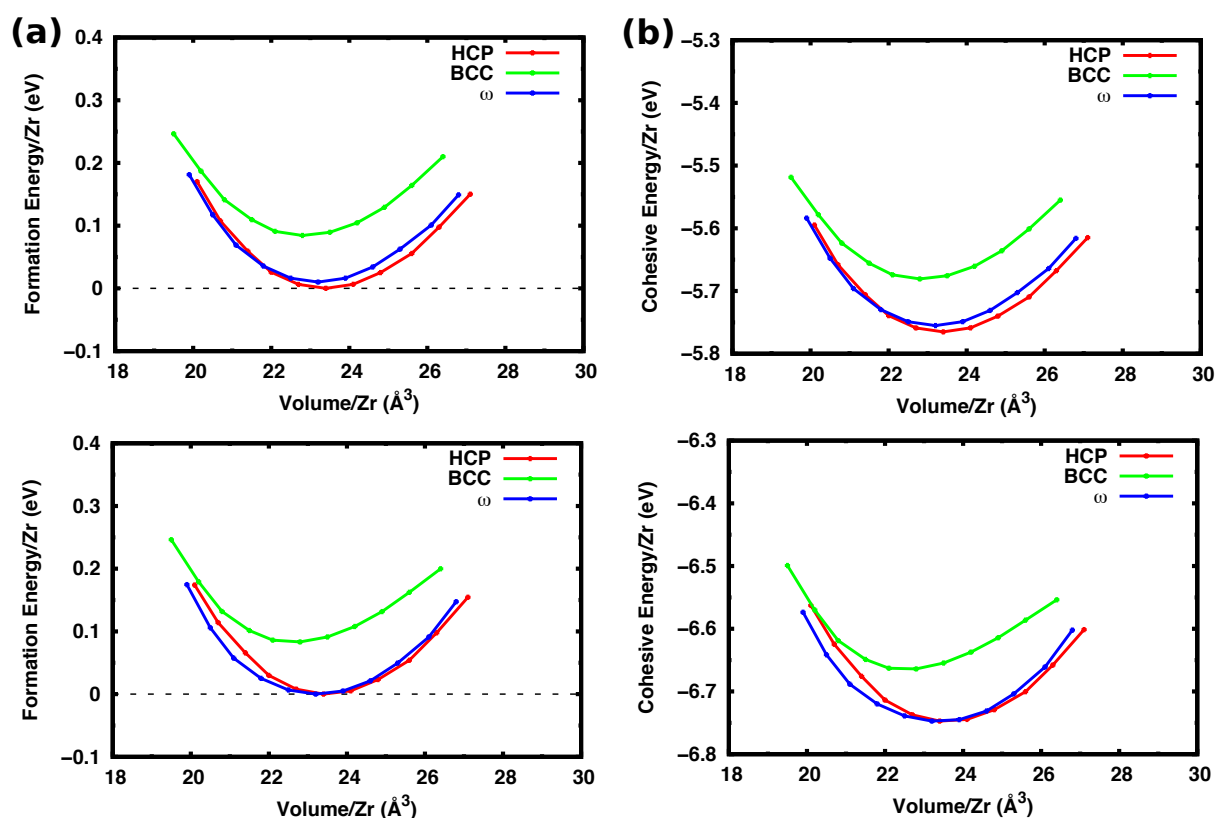


Figure 5.7 (a) Relative/formation and (b) energy curve vs volume per atom curve for all experimental phases of bulk Zr obtained using the “PSO 1” (upper panel) and “PSO 2” (lower panel) repulsive potentials in DFT geometry.

At this point we were able to reproduce the E – V curve of DFT reference with good accuracy. We have to further validate the usability of the “PSO 1” parameter by locating the true minimum of each phase. The energy minimization was carried out using same procedure as in the “poly” repulsive set. We confirmed that for HCP phase, the DFT geometry has all force components below the threshold value if calculated with “PSO 1” parameter. It means

that the geometry optimization will stop if the geometry starts at DFT geometry (Table 5.1). Meanwhile, for BCC, the lattice parameter a is 3.572 Å, which is also in perfect agreement with DFT results, but for ω phase geometry optimization led to wrong minimum. The lattice parameter a is 4.642 Å while c is 3.841 Å. With this geometry, the cohesive energy of ω phase becomes lower to -5.82 eV/atom. However, further test on HCP phase shows that the DFT geometry is not a true minimum but a saddle point. This can be shown in the potential energy surface (PES) of HCP in Figure 5.8. The PES is constructed as function of lattice parameter a as x -axis and c as y -axis. There is a rather deep potential well at approximately (2.90, 6.10) with -360 meV and a slightly deeper minimum at approximately (3.25, 5.10) with -0.25 meV lower than DFT geometry energy. If the initial geometry slightly deviates from the DFT geometry, the geometry will converge to either the lower energy geometry. As for BCC phase, the true minimum is correct, while for ω phase, the PES also shows 2 minima. On the other hand, DFT results show that the geometrical parameters listed in Table 5.1 are indeed global minimum for each surface.

Based on the results of “PSO 1” parameterization, we proceed further to improve the DFTB results from the repulsive potential, especially for removing the “fake” minimum of the HCP phase and finding the correct minimum for ω phase. The improvement may be established by adding more systems into the training sets. The PES from DFT calculations for HCP and ω phase can become additional training sets. Additionally, the displacement of atoms inside the cell can also be used as training sets.

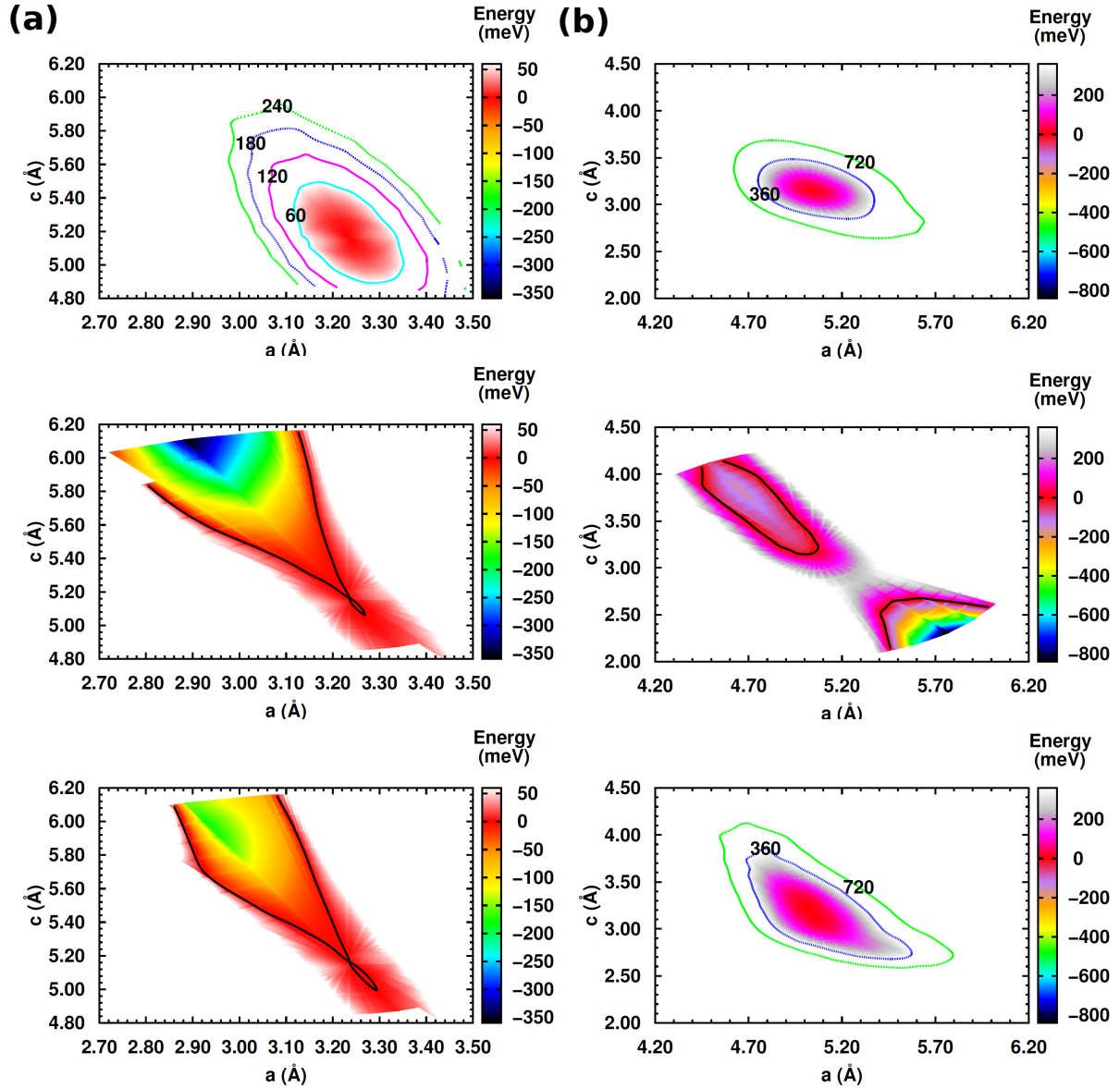


Figure 5.8 PES contour of (a) HCP and (b) ω phase calculated at PBE-PAW (upper panel), DFTB-PSO 1 (middle panel) and DFTB-PSO 2 (lower panel). Black solid line represents the surface with value of 0. Energy is relative with respect to energy of DFT equilibrium geometry for each phase.

Next repulsive potential that improves the results is denoted as “PSO 2”. In “PSO 2” parameterization, the more training sets were added in addition to “PSO 1” training sets. Those additional training sets are: random compression and expansion of a and c lattice parameter for HCP and ω phase, taken from the DFT PES, and atomic displacements in HCP and ω phase, in total about 100 data points were fitted. Also, the energy difference between

HCP and ω phase were given an additional weight by factor of 10 to 20 in order to obtain closer energy results to DFT value. This potential also has the cutoff of 10 bohr and number of the knots are 6. The repulsive potential, as shown in Figure 5.5, is less repulsive than the “PSO 1” potential in the spline part.

The $E - V$ curve calculated using “PSO 2” repulsive potential is hardly affected compared to the “PSO 1” $E - V$ curve. The value of bulk modulus B_0 is increased by about 4 GPa for HCP and ω while for BCC phase, the bulk modulus is decreased by 2 GPa. The fitness value of this set is 0.05. The major improvement of this set is the energetic. The energy difference of HCP and ω phase, which now becomes ~ 0.9 meV/atom while the energy difference of HCP - BCC remains the same. The cohesive energy is now closer to the DFT results. The cohesive energy for HCP phase is -6.64 eV/atom, now only lower than DFT value and experimental value by 0.24 and 0.5 eV, respectively.

Table 5.3 Bulk properties of Zr obtained using PSO generated repulsive potential.

		PSO 1	PSO 2	PSO 3
HCP	a (Å)	3.235	3.238	3.163
	c (Å)	5.163	5.165	5.187
	c/a	1.597	1.595	1.639
	E_{coh}/Zr (eV)	-5.76	-6.64	-10.752
	E_{form}/Zr (eV)	0.00	0.00	0.00
	B_0 (GPa)	97.91	101.51	212.87
	B_0'	2.39	1.222	-1.28
BCC	a (Å)	3.572	3.552	3.520
	E_{coh}/Zr (eV)	-5.68	-6.56	-10.744
	E_{form}/Zr (eV)	0.083	0.083	0.008
	B_0 (GPa)	89.00	87.28	151.04
	B_0'	2.933	6.297	-2.133
ω	a (Å)	4.642	5.039	4.939
	c (Å)	3.841	3.178	3.049
	c/a	0.827	0.630	0.617
	E_{coh}/Zr (eV)	-5.82 (-5.77)	-6.64	-10.747
	E_{form}/Zr (eV)	-0.06 (0.01)	3.3×10^{-5} (9.0×10^{-4})	5.6×10^{-3}
	B_0 (GPa)	(94.93)	98.98	201.33
	B_0'	(3.205)	2.507	2.67

As in PSO 1, we also need to locate the true minimum of each phase. The fully optimized geometry parameters are shown in Table 5.3. Fully optimized geometry for HCP

phase is also in good agreement compared to the DFT geometry if the initial geometry is from the DFT geometry. The geometry optimization will stop if the geometry starts at DFT geometry in few optimization steps. However, there is still a deeper minimum at $a = 2.92$ and $c = 6.00$ with -175 meV lower than the minimum, as shown in the PES where the HCP geometry parameters listed in Table 5.3 is still a “saddle point”, therefore if the initial geometry deviates from DFT geometry, the optimized geometry will be the deeper minimum geometry. As for BCC, the lattice parameter a is 3.552 Å, while for ω phase geometry optimization leads to the real minimum with the lattice parameter a is 5.039 Å and c is 3.178 Å.

After a number of trial attempts, we deduced that the cause of the “fake” minimum in HCP phase is the long-range parameter itself. Putting the “fake” minimum geometry into the training set will eventually lead to unphysical shape of the repulsive (oscillation), which is probably caused by the two systems that have different coordination number but have same energy. Furthermore, even that if we could produce the long range repulsive potential that can mimic the DFT geometry and energetic perfectly, we have a preference to use the short-range repulsive potential for our systems in interest that will be discussed in next section.

As the last resort, we created the short-range repulsive potential, called “PSO 3”. “PSO 3” was created using similar training sets as in the hand-made parameterization, HCP phase with their ideal c/a value of 1.633 . About 10 data points are fitted. Addition of more phases into the training set will not improve the generated repulsive potential; it only worsens the fitness value, while roughly produces similar repulsive potential shape and gives similar performance. This potential has cutoff value of 6.23 bohr and the number of the knots are 2. The shape of “PSO 3” repulsive, as shown in Figure 5.5 resembles the polynomial fitted

repulsive potential, apart that the “PSO 3” repulsive has smoother decay to 0 to the cutoff radius.

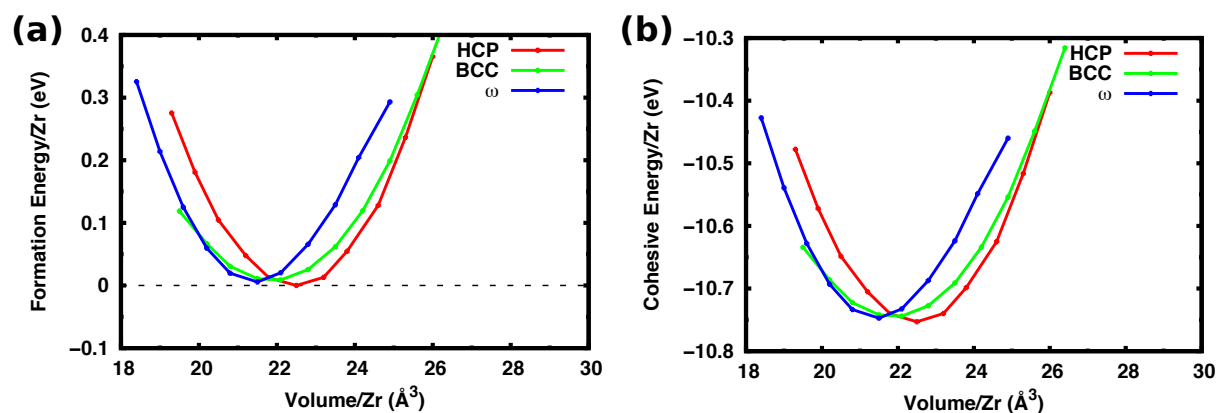


Figure 5.9 (a) Relative/formation and (b) cohesive energy vs volume per atom curve for all experimental phases of bulk Zr obtained using the “PSO 3” repulsive potential. For formation energy, equilibrium HCP geometry energy was used as reference.

As for its performance, from the short-range polynomial fitted repulsive potential results, we will expect a severe disagreement for the bulk modulus. The value of bulk modulus for each phase is about twice of the reference value bulk modulus. This is also proven from the $E - V$ curve shown in Figure 5.9 where the curve is very steep compared to DFT $E - V$ curve. However, the $E - V$ curve is smoother than the $E - V$ curve of bulk Zr calculated from polynomial fitted repulsive potential since the “PSO 3” repulsive has smoother decay.

In general, all the phases obtained using “PSO 3” has more compressed volume compared to the reference, apart of that, the geometrical parameter for some phase is in reasonable agreement with reference value. For HCP phase, the lattice parameter a is shorter by 0.07 Å while lattice parameter c is 0.02 Å longer than DFT value yielding an overestimation of c/a ratio to 1.639. For BCC phase, the lattice parameter a is shorter by 0.03 Å while for ω phase, both lattice parameter a and c are shorter by 0.10 Å.

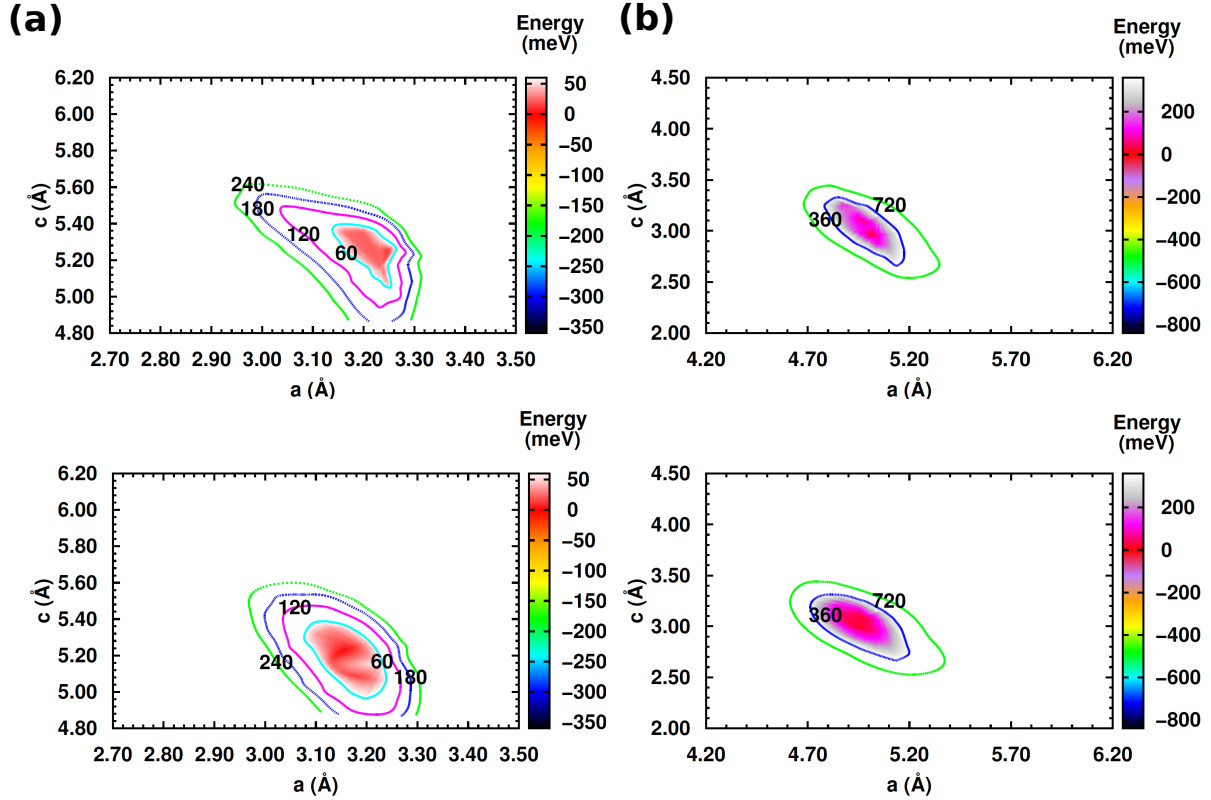


Figure 5.10 PES contour of (a) HCP and (b) ω phase calculated using polynomial fitted (upper panel) and PSO 3 (lower panel) repulsive potential. Energy is relative with respect to energy of DFTB equilibrium geometry for each phase listed in Table 5.2 and Table 5.3.

Now we discuss the energetic properties. Since this repulsive potential resembles the polynomial fitted repulsive, the cohesive energy is also lower than the DFT cohesive energy for about 4 eV. On the other hand, the energy ordering of the three phases is surprisingly correct according to the DFT results, apart that the value of energy difference is not correctly reproduced. HCP is the most stable phase followed by ω with 5 meV/Zr higher than energy of HCP phase. The most unstable phase is BCC with 8 meV/Zr higher than BCC. With the “PSO 3” repulsive potential, all of the equilibrium geometry of the three phases are the global minimum in their respective PES, especially for HCP and ω phase as shown in Figure 5.10. At this point, “PSO 3” is considered to be the best repulsive potential from the PSO parameterization that we could create. The geometry of two most important phases

(HCP and BCC) are in reasonable agreement compared to the DFT value and the geometry is stable to the symmetry breaking. The drawback of this parameter is the severe overbinding of the cohesive energy and the overestimation of the bulk modulus. Nevertheless, the last two properties are common problem in DFTB, especially for bulk metal.

5.4 Discussions

DFTB parameterizations are nontrivial problems. One can create as many as possible set from the same electronic parameter based on different fitting systems and testing sets. Their performances may be different if applied to different systems.

This works focus on the repulsive parameterization only while keeping the electronic parameters fixed as the control variable. We considered that the electronic parameters are already good enough to produce good band structure, the quantity that can usually describe good electronic parameter. Our long-range repulsive potentials show that its shape is not monotonically decreasing to the cutoff value, but there is a bump in the middle of the potential. This bump indicates that there is an overbinding for the systems. This can be shown from our cohesive energy results. The long-range repulsive potential results (“PSO 1” and “PSO 2”) show that the cohesive energy only has a difference with the reference value for around ~ 0.7 eV, even in “PSO 1”, the cohesive energy is higher than the reference value, while “PSO 2” is slightly lower due to the less repulsive nature of the potential. On the other hand, as already shown, the cohesive energy from the short-range potential is much lower than the reference by ~ 4 eV.

One can suggest that the improvement can be achieved by making new electronic parameters. We also fitted the new orbital confining potential based on the HCP Zr band structure as in the work done by Nishimura, using different initial guess for the W , a and r_0

but it also turned out that in order to achieve acceptable $E - V$ curve compared to the DFT, the repulsive also has to be long enough as on our “PSO 1” and “PSO 2” case, and the hump in the repulsive potential still presents while short range repulsive potential will roughly yield similar quality with our short range potential. Simultaneous optimization of electronic and repulsive parameter was also performed. However it can only make the fitness value worse for either the band structure (electronic) or the $E - V$ curve (repulsive). Probably, for our Zr case, we need to explicitly treat more electrons for the basis function (e.g. semicore electrons) or include the multipole interactions in the Hamiltonian to improve the SCC part [198], in order to get an acceptable $E - V$ curve with short-range potential, but to the current status of DFTB, such a scheme is probably still a proposal.

That is not the case that even though that the new electronic set is able to produce a long-range repulsive potential that can produce the acceptable $E - V$ curve and the structures are stable with the symmetry breaking. Remember that we would like to use the DFTB method and our parameter for simulation of YSZ system. In that system, one of the important quantities that we would like to address is the oxygen migration barrier energy. In a preliminary works, we already created the Zr - O repulsive potential based on long-range Zr - Zr potential. It turned out that the resulting Zr - O repulsive yield mostly attractive potential i.e. value below zero in the Zr - O working distances, despite the similarity of the $E - V$ curve of the ZrO_2 phases compared to the DFT $E - V$ reference curve and accurate energy ordering and difference [199]. This is due to the nonzero Zr - Zr interactions in the ZrO_2 reference systems that force the Zr - O potential to be more negative in order to cope with the fitness of reference energy. This has the consequences that the oxygen migration barrier in ZrO_2 will be negative that is somehow unphysical. If we used the Zr - Zr potential

that has the cutoff radius of less than 7 bohr, we will eventually managed to obtain short-range Zr – O repulsive, that can not only yield positive oxygen migration barrier, but also the E – V curve and the geometry are in excellent agreement with the DFT reference. Based on this, as for our effort to find good Zr – Zr parameter set, we propose the current electronic parameter sets combined with the short-range repulsive potential for the parameter extension in the simulation of YSZ SOFC systems, either “poly” or “PSO 3”.

The long-range repulsive potential can be applicable for other purposes, for example, the MD simulation to elucidate the elastic properties or phase transition of pristine bulk Zr, where the accurate description of energy ordering and bulk modulus are mandatory. Such a purpose is beyond our work interest.

5.5 Summary

We have developed a number of sets of DFTB2 repulsive potentials for Zr – Zr element pair using the electronic parameter developed by Nishimura et al. The repulsive potentials were created from energy versus volume (E – V) profiles that had been generated from planewave DFT calculations using the Perdew-Burke-Ernzerhof (PBE) functional. We created two distinct potential: long-range and short-range using polynomial fitting and particle swarm optimization (PSO) algorithm. The repulsive potentials along with the fixed electronic parameter were tested to the all experimentally exist bulk phase of Zr, namely HCP, BCC and ω phase.

We found that for our case, the long-range repulsive potential will have excellent agreement with the reference E – V profile from the three phases; on the other hand, the HCP phase geometry generated using the long-range repulsive potentials is prone to symmetry breaking due to the presence of fake minimum in the potential energy surface which is the

consequences of having the long-range potential, while BCC and ω phase are stable to geometry deformation. The short-range repulsive potentials, on the other hand, give rather poor agreement with the reference $E - V$ profile, however they give fairly reasonable geometries for all of three phases and are stable with respect to symmetry breaking.

Apart from the disadvantages from the short-range repulsive potential, based on the discussions, we propose to using the short-range repulsive potential, either the polynomial fitted or PSO generated for further development of repulsive potential for the YSZ based SOFC systems where the oxygen migration barrier is an important quantity and the Zr – Zr interaction should not interfere with the Zr – O interactions.

Chapter 6 Summary and Outlook

In this thesis, we have performed extensive calculations using methods commonly employed in computational chemistry involving many chemical and physical systems and their benchmarks for developing the density-functional tight-binding (DFTB) parameters. The summary is as follows.

In Chapter 3, we addressed the effects of several popular density functional theory (DFT) exchange-correlation functionals to the binding energy and dissociation limit of atomic fluorine attack on coronene from the potential energy curves (PECs). It turned out that pure DFT functionals predict the largest binding energy while hybrid DFT functionals predict lower binding energy than pure DFT functional. Similar trend occurs for the dissociation limit. Coronene-F total energies at long separation do not converge to the sum of separate coronene molecular and fluorine atom calculated using pure DFT functionals. Addition of Hartree-Fock exchange (HFX) to the functional either by hybrid or range separated scheme will cause the energy convergence closer to the correct dissociation limit. We modified the C – F repulsive potential based on the formation energy curve of the reference high-level G2MS data. We managed to obtain improved PEC compared to older pbc-0-3 parameter. The geometry and binding energy of coronene-F calculated using the new C-F potential are remarkably acceptable compared to the reference data.

In Chapter 4, we proposed a reaction mechanism of atomic oxygen adsorption on coronene. The reaction involves an intersystem crossing (ISC) due to the ability of the system to be either in triplet and singlet state. The entrance channel of oxygen adsorption is via the “top” carbon atom sites in coronene followed by migration to the stable “bridge” site. In the same chapter, the PECs of atomic nitrogen on coronene were examined. There is a similar

trend for binding energy with respect to the DFT functional employed where pure DFT functional (PBE) predicts the lowest binding energy while hybrid DFT functional (B3LYP) predict higher binding energy than pure DFT functional. On the other hand, the dissociation limit of the coronene-N system converges to the sum of separate coronene molecular and nitrogen atom calculated using both type of functionals in contrast with the results from coronene-F and coronene-O. It is noteworthy to mention that the increasing of atomic electronegativity is proportional to the self-interaction error (SIE) experienced in DFT functionals.

We also evaluated the existing DFTB parameters in Chapter 3 and Chapter 4. In general, the currently available DFTB parameters need to be adjusted in order to fulfill the applicability for molecular dynamic (MD) simulations of atomic attacks on graphene/graphitic surfaces based on their PECs. The DFTB method also experiences similar trend of SIE as in the DFT functionals.

Chapter 5 presents the novel development of Zr – Zr DFTB2 repulsive potential. Many schemes of Zr – Zr parameters are presented. We created long-range and short-range Zr - Zr potential for the applications in simulation of solid-state systems. We came to conclusion that the short-range Zr – Zr repulsive potential is more suitable for the future applications.

We are in the initial stage of creating Zr - O, Y - Y, Y – O and Y – Zr pair potential for the complete DFTB parameters for the Ytria-Stabilized Zirconia (YSZ) systems. The details will be reported in the future.

References

- [1] Schrödinger, E. *Phys. Rev.* **1926**, *28*, 1049.
- [2] Dirac, P. A. M. *Proc. R. Soc. London. Ser. A* **1928**, *117*, 610.
- [3] Moore, G. E. *Electronics* **1965**, *86*, 82.
- [4] Elstner, M.; Porezag, D.; Jungnickel, G.; Elsner, J.; Haugk, M.; Frauenheim, T.; Suhai, S.; Seifert, G. *Phys. Rev. B* **1998**, *58*, 7260.
- [5] Porezag, D.; Frauenheim, T.; Köhler, T.; Seifert, G.; Kaschner, R. *Phys. Rev. B* **1995**, *51*, 12947.
- [6] Gaus, M.; Cui, Q.; Elstner, M. *J. Chem. Theory Comput.* **2012**, *7*, 931.
- [7] Geim, A. K.; Novoselov, K. S. *Nat. Mater.* **2007**, *6*, 183.
- [8] Malavasi, L.; Fisher, C. a J.; Islam, M. S. *Chem. Soc. Rev.* **2010**, *39*, 4370.
- [9] Cao, X. Q.; Vassen, R.; Stoever, D. J. *Eur. Ceram. Soc.* **2004**, *24*, 1.
- [10] Zhang, Y.; Chen, C.; Lin, X.; Li, D.; Chen, X.; Zhan, Y.; Zheng, Q. *Int. J. Hydrogen Energy* **2014**, *39*, 3746.
- [11] Lashtabeg, A.; Skinner, S. J. *J. Mater. Chem.* **2006**, *16*, 3161.
- [12] Szabo, A.; Ostlund, N. S. *Modern Quantum Chemistry: Introduction to Advanced Electronic Structure Theory*; 1989.
- [13] Møller, C.; Plesset, M. S. *Phys. Rev.* **1934**, *46*, 618.
- [14] Sherrill, C. D.; Schaefer, H. F. *Adv. Quantum Chem.* **1999**, *34*, 143.
- [15] Bartlett, R. J.; Musial, M. *Rev. Mod. Phys.* **2007**, *79*, 291.
- [16] Hohenberg, P.; Kohn, W. *Phys. Rev.* **1964**, *136*, B864.
- [17] Kohn, W.; Sham, L. J. *Phys. Rev.* **1965**, *140*, A1133.
- [18] Dirac, P. A. M. *Math. Proc. Cambridge Philos. Soc.* **1930**, *26*, 376.

- [19] Vosko, S. H.; Wilk, L.; Nusair, M. *Can. J. Phys.* **1980**, *58*, 1200.
- [20] Perdew, J. P.; Zunger, A. *Phys. Rev. B* **1981**, *23*, 5048.
- [21] Becke, A. D. *Phys. Rev. A* **1988**, *38*, 3098.
- [22] Lee, C.; Yang, W.; Parr, R. G. *Phys. Rev. B* **1988**, *37*, 785.
- [23] Perdew, J. P. *Phys. Rev. B* **1986**, *33*, 8822.
- [24] Perdew, J. P.; Burke, K.; Ernzerhof, M. *Phys. Rev. Lett.* **1996**, *77*, 3865.
- [25] Perdew, J. P.; Burke, K.; Ernzerhof, M. *Phys. Rev. Lett.* **1997**, *78*, 1396.
- [26] Becke, A. D. *J. Chem. Phys.* **1993**, *98*, 5648.
- [27] Mori-Sánchez, P.; Cohen, A. J.; Yang, W. *J. Chem. Phys.* **2006**, *125*.
- [28] Baer, R.; Livshits, E.; Salzner, U. *Annu. Rev. Phys. Chem.* **2010**, *61*, 85.
- [29] Vydrov, O. A.; Scuseria, G. E. *J. Chem. Phys.* **2006**, *125*, 234109/1.
- [30] Vydrov, O. A.; Scuseria, G. E.; Perdew, J. P. *J. Chem. Phys.* **2007**, *126*, 154109/1.
- [31] Iikura, H.; Tsuneda, T.; Yanai, T.; Hirao, K. *J. Chem. Phys.* **2001**, *115*, 3540.
- [32] Yanai, T.; Tew, D. P.; Handy, N. C. *Chem. Phys. Lett.* **2004**, *393*, 51.
- [33] Car, R.; Parrinello, M. *Phys. Rev. Lett.* **1985**, *55*, 2471.
- [34] Koskinen, P.; Mäkinen, V. *Comput. Mater. Sci.* **2009**, *47*, 237.
- [35] Köhler, C. *Univ. Paderborn* **2003**, *PhD Thesis*.
- [36] Köhler, C.; Seifert, G.; Frauenheim, T. *Chem. Phys.* **2005**, *309*, 23.
- [37] Hourahine, B.; Sanna, S.; Aradi, B.; Köhler, C.; Niehaus, T.; Frauenheim, T. *J. Phys. Chem. A* **2007**, *111*, 5671.
- [38] Niehaus, T. A.; Sala, F. Della. *Phys. Status Solidi B* **2012**, *249*, 237.
- [39] Lutsker, V.; Aradi, B.; Niehaus, T. A. *J. Chem. Phys.* **2015**, *143*, 184107/1.
- [40] Janak, J. F. *Phys. Rev. B* **1978**, *18*, 7165.

- [41] Wahiduzzaman, M.; Oliveira, A. F.; Philipsen, P.; Zhechkov, L.; Lenthe, E. Van; Heine, T. *J. Chem. Theory Comput.* **2013**, *9*, 4006.
- [42] Woods, R. D.; Saxon, D. S. *Phys. Rev.* **1954**, *95*, 577.
- [43] Witek, H. A.; Köhler, C.; Frauenheim, T.; Morokuma, K.; Elstner, M. *J. Phys. Chem. A* **2007**, *111*, 5712.
- [44] Slater, J. C.; Koster, G. F. *Phys. Rev.* **1954**, *94*, 1498.
- [45] Elstner, M. *Theor. Chem. Acc.* **2006**, *116*, 316.
- [46] Niehaus, T. A.; Elstner, M.; Frauenheim, T.; Suhai, S. *J. Mol. Struct. THEOCHEM* **2001**, *541*, 185.
- [47] Zheng, G.; Witek, H. A.; Bobadova-Parvanova, P.; Irle, S.; Musaev, D. G.; Prabhakar, R.; Morokuma, K.; Lundberg, M.; Elstner, M.; Kohler, C.; Frauenheim, T. *J. Chem. Theory Comput.* **2007**, *3*, 1349.
- [48] Kubař, T.; Bodrog, Z.; Gaus, M.; Köhler, C.; Aradi, B.; Frauenheim, T.; Elstner, M. *J. Chem. Theory Comput.* **2013**, *9*, 2939.
- [49] Grundkötter-Stock, B.; Bezugly, V.; Kunstmann, J.; Cuniberti, G.; Frauenheim, T.; Niehaus, T. A. *J. Chem. Theory Comput.* **2012**, *8*, 1153.
- [50] Szücs, B.; Hajnal, Z.; Frauenheim, T.; González, C.; Ortega, J.; Pérez, R.; Flores, F. *Appl. Surf. Sci.* **2003**, *212-213*, 861.
- [51] Szucs, B.; Hajnal, Z.; Scholz, R.; Sanna, S.; Frauenheim, T.; Szücs, B. *Appl. Surf. Sci.* **2004**, *234*, 173.
- [52] Simdyankin, S. I.; Elliott, S. R.; Hajnal, Z.; Niehaus, T. A.; Frauenheim, T. *Phys. Rev. B - Condens. Matter Mater. Phys.* **2004**, *69*, 1.
- [53] Simdyankin, S. I.; Niehaus, T. A.; Natarajan, G.; Frauenheim, T.; Elliott, S. R. *Phys.*

- Rev. Lett.* **2005**, *94*, 1.
- [54] Moreira, N. H.; Dolgonos, G.; Aradi, B.; Rosa, A. L.; Frauenheim, T. *J. Chem. Theory Comput.* **2009**, *5*, 605.
- [55] Dolgonos, G.; Aradi, B.; Moreira, N. H.; Frauenheim, T. *J. Chem. Theory Comput.* **2010**, *6*, 266.
- [56] Fihey, A.; Hettich, C.; Touzeau, J.; Maurel, F.; Perrier, A.; Köhler, C.; Aradi, B.; Frauenheim, T. *J. Comput. Chem.* **2015**, *36*, 2075.
- [57] Köhler, C.; Frauenheim, T. *Surf. Sci.* **2006**, *600*, 453.
- [58] Kohler, C.; Hajnal, Z.; Deak, P.; Frauenheim, T.; Suhai, S. *Phys. Rev. B* **2001**, *64*, 085333.
- [59] Sieck, A.; Frauenheim, T.; Jackson, K. A. *Phys. Status Solidi Basic Res.* **2003**, *240*, 537.
- [60] Sanna, S.; Hourahine, B.; Gerstmann, U.; Frauenheim, T. *Phys. Rev. B - Condens. Matter Mater. Phys.* **2007**, *76*, 1.
- [61] Markov, S.; Aradi, B.; Yam, C. Y.; Xie, H.; Frauenheim, T.; Chen, G. *IEEE Trans. Electron Devices* **2015**, *62*, 696.
- [62] Markov, S.; Penazzi, G.; Kwok, Y.; Pecchia, A.; Aradi, B.; Frauenheim, T.; Chen, G. *IEEE Electron Device Lett.* **2015**, *36*, 1076.
- [63] Frenzel, J.; Oliveira, A. F.; Jardillie, N.; Heine, T.; Seifert, G. *Semi-relativistic, self-consistent charge Slater-Koster tables for density-functional based tight-binding (DFTB) for materials science simulations.*
- [64] Sarkar, S.; Pal, S.; Sarkar, P.; Rosa, A. L.; Frauenheim, T. *J. Chem. Theory Comput.* **2011**, *7*, 2262.

- [65] Saha, S.; Pal, S.; Sarkar, P.; Rosa, A. L.; Frauenheim, T. *J. Comput. Chem.* **2012**, *33*, 1165.
- [66] Hellström, M.; Jorner, K.; Bryngelsson, M.; Huber, S. E.; Kullgren, J.; Frauenheim, T.; Broqvist, P. *J. Phys. Chem. C* **2013**, *117*, 17004.
- [67] Oliveira, A. F.; Philipsen, P.; Heine, T. *J. Chem. Theory Comput.* **2015**, *11*, 5209.
- [68] Liu, X.; Wahiduzzaman, M.; Oliveira, A. F.; Heine, T.; Salahub, D. R. *Theor. Chem. Acc.* **2016**, *135*, 168.
- [69] Nishimura, Y. Development of the Density Functional Tight Binding Method and Its Application in Computational Nanomaterial Science. Ph.D. thesis, Nagoya University, 2013.
- [70] Kennedy, J.; Eberhart, R. *Proc. IEEE Int. Conf. Neural Networks* **1995**, *4*, 1942.
- [71] Chou, C.-P.; Nishimura, Y.; Fan, C.-C.; Mazur, G.; Irle, S.; Witek, H. A. *J. Chem. Theory Comput.* **2016**, *12*, 53.
- [72] Kita, Y.; Watanabe, N.; Fujii, Y. *J. Am. Chem. Soc.* **1979**, *101*, 3832.
- [73] Ruff, O.; Bretschneider, O. *Zeitschrift für Anorg. und Allg. Chemie* **1934**, *217*, 1.
- [74] Watanabe, N.; Nakajima, T.; Touhara, H. *Graphite Fluorides*, 1st ed.; Elsevier B.V.: Amsterdam, 1988.
- [75] Kroto, H. W.; Heath, J. R.; O'Brien, S. C.; Curl, R. F.; Smalley, R. E. *Nature* **1985**, *318*, 162.
- [76] Iijima, S. *Nature* **1991**, *354*, 56.
- [77] Selig, H.; Lifshitz, C.; Peres, T.; Fischer, J. E.; Smith, A. B. I.; McGhie, A. R.; Romanow, W. J.; McCauley, J. P. *J. Am. Chem. Soc.* **1991**, *113*, 5475.
- [78] Mickelson, E. T.; Huffman, C. B.; Rinzler, A. G.; Smalley, R. E.; Hauge, R. H.;

- Margrave, J. L. *Chem. Phys. Lett.* **1998**, *296*, 188.
- [79] Hayashi, T.; Terrones, M.; Scheu, C.; Kim, Y. A.; Rühle, M.; Nakajima, T.; Endo, M. *Nano Lett.* **2002**, *2*, 491.
- [80] Peng, H.; Gu, Z.; Yang, J.; Zimmerman, J. L.; Willis, P. A.; Bronikowski, M. J.; Smalley, R. E.; Hauge, R. H.; Margrave, J. L. *Nano Lett.* **2001**, *1*, 625.
- [81] Root, M. J. *Nano Lett.* **2002**, *2*, 541.
- [82] Nair, R. R.; Ren, W.; Jalil, R.; Riaz, I.; Kravets, V. G.; Britnell, L.; Blake, P.; Schedin, F.; Mayorov, A. S.; Yuan, S.; Katsnelson, M. I.; Cheng, H. M.; Strupinski, W.; Bulusheva, L. G.; Okotrub, A. V.; Grigorieva, I. V.; Grigorenko, A. N.; Novoselov, K. S.; Geim, A. K. *Small* **2010**, *6*, 2877.
- [83] Cheng, S. H.; Zou, K.; Okino, F.; Gutierrez, H. R.; Gupta, A.; Shen, N.; Eklund, P. C.; Sofo, J. O.; Zhu, J. *Phys. Rev. B* **2010**, *81*, 205435/1.
- [84] Robinson, J. T.; Burgess, J. S.; Junkermeier, C. E.; Badescu, S. C.; Reinecke, T. L.; Perkins, F. K.; Zalalutdniov, M. K.; Baldwin, J. W.; Culbertson, J. C.; Sheehan, P. E.; Snow, E. S. *Nano Lett.* **2010**, *10*, 3001.
- [85] Jeon, K. J.; Lee, Z.; Pollak, E.; Moreschini, L.; Bostwick, A.; Park, C. M.; Mendelsberg, R.; Radmilovic, V.; Kosteckii, R.; Richardson, T. J.; Rotenberg, E. *ACS Nano* **2011**, *5*, 1042.
- [86] Withers, F.; Russo, S.; Dubois, M.; Craciun, M. F. *Nano Res. Lett.* **2011**, *6*, 526.
- [87] Walter, A. L.; Sahin, H.; Jeon, K.; Bostwick, A.; Horzum, S.; Koch, R.; Speck, F.; Ostler, M.; Nagel, P.; Merz, M.; Schuppler, S.; Moreschini, L.; Chang, Y. J.; Seyller, T.; Peeters, F. M.; Horn, K.; Rotenberg, E. *ACS Nano* **2014**, *8*, 7801.
- [88] Withers, F.; Bointon, T. H.; Dubois, M.; Russo, S.; Craciun, M. F. *Nano Lett.* **2011**, *11*,

- 3912.
- [89] Gao, X.; Wang, Y.; Liu, X.; Chan, T.-L.; Irle, S.; Zhao, Y.; Zhang, S. B. *Phys. Chem. Chem. Phys.* **2011**, *13*, 19449.
- [90] Karlický, F.; Otyepka, M. *Ann. Phys.* **2014**, *526*, 408.
- [91] Karlický, F.; Otyepka, M. *J. Chem. Theory Comput.* **2013**, *9*, 4155.
- [92] Zbořil, R.; Karlický, F.; Bourlinos, A. B.; Steriotis, T. A.; Stubos, A. K.; Georgakilas, V.; Šafařová, K.; Jančík, D.; Trapalis, C.; Otyepka, M. *Small* **2010**, *6*, 2885.
- [93] Gong, P.; Wang, Z.; Li, Z.; Mi, Y.; Sun, J.; Niu, L.; Wang, H.; Wang, J.; Yang, S. *RSC Adv.* **2013**, *3*, 6327.
- [94] Zhao, F.-G.; Zhao, G.; Liu, X.-H.; Ge, C.-W.; Wang, J.-T.; Li, B.-L.; Wang, Q.-G.; Li, W.-S.; Chen, Q.-Y. *J. Mater. Chem. A* **2014**, *2*, 8782.
- [95] Tahara, K.; Iwasaki, T.; Matsutani, A.; Hatano, M. *Appl. Phys. Lett.* **2012**, *101*, 163105/1.
- [96] Ho, K. I.; Liao, J. H.; Huang, C. H.; Hsu, C. L.; Zhang, W.; Lu, A. Y.; Li, L. J.; Lai, C. S.; Su, C. Y. *Small* **2014**, *10*, 989.
- [97] Lee, W. H.; Suk, J. W.; Chou, H.; Lee, J.; Hao, Y.; Wu, Y.; Piner, R.; Akinwande, D.; Kim, K. S.; Ruoff, R. S. *Nano Lett.* **2012**, *12*, 2374.
- [98] Sahin, H.; Topsakal, M.; Ciraci, S. *Phys. Rev. B* **2011**, *83*, 115432/1.
- [99] Boukhvalov, D. W.; Katsnelson, M. I. *Nano Lett.* **2008**, *8*, 4374.
- [100] Boukhvalov, D. W.; Son, Y. W. *ChemPhysChem* **2012**, *13*, 1463.
- [101] Contreras, C. N.; Cocolletzi, H. H.; Anota, E. C. *J. Mol. Model.* **2011**, *17*, 2093.
- [102] Enyashin, A. N.; Ivanovskii, A. L. *Chem. Phys. Lett.* **2013**, *576*, 44.
- [103] Hsing, C. R.; Wei, C. M.; Chou, M. Y. *J. Phys. Condens. Matter* **2012**, *24*, 395002/1.

- [104] Medeiros, P. V. C.; Mascarenhas, A. J. S.; de Brito Mota, F.; de Castilho, C. M. C. *Nanotechnology* **2010**, *21*, 485701/1.
- [105] Osuna, S.; Torrent-Sucarrat, M.; Solà, M.; Geerlings, P.; Ewels, C. P.; Lier, G. Van. *J. Phys. Chem. C* **2010**, *114*, 3340.
- [106] Ribas, M. A.; Singh, A. K.; Sorokin, P. B.; Yakobson, B. I. *Nano Res.* **2011**, *4*, 143.
- [107] Wang, S.; Xuezhai, K.; Zhang, W.; Gong, W.; Huai, P.; Zhang, W.; Zhu, Z. *Appl. Surf. Sci.* **2014**, *292*, 488.
- [108] Wu, M.; Tse, J. S.; Jiang, J. Z. *J. Phys. Chem. Lett.* **2010**, *1*, 1394.
- [109] Wu, M.; Cao, C.; Jiang, J. Z. *Nanotechnology* **2010**, *21*, 505202/1.
- [110] Santos, H.; Henrard, L. *J. Phys. Chem. C* **2014**, *118*, 27074.
- [111] Dubecký, M.; Otyepková, E.; Lazar, P.; Karlický, F.; Petr, M.; Čépe, K.; Banáš, P.; Zbořil, R.; Otyepka, M. *J. Phys. Chem. Lett.* **2015**, 1430.
- [112] Junkermeier, C. E.; Badescu, S. C.; Reinecke, T. L. *arXiv:1302.6878* **2013**.
- [113] Lee, S.; Jang, S.; Park, K.; Jang, E. C.; Kim, J.; Neuhauser, D.; Lee, S. *J. Phys. Chem. C* **2013**, *117*, 5407.
- [114] Bulat, F. A.; Burgess, J. S.; Matis, B. R.; Baldwin, J. W.; MacAveiu, L.; Murray, J. S.; Politzer, P. *J. Phys. Chem. A* **2012**, *116*, 8644.
- [115] Nijamudheen, A.; Datta, A. *J. Phys. Chem. A* **2013**, *117*, 8506.
- [116] Adamo, C.; Barone, V. *J. Chem. Phys.* **1999**, *110*, 6158.
- [117] Huzak, M.; Deleuze, M. S.; Hajgat, B. *J. Chem. Phys.* **2011**, *135*, 104704/1.
- [118] Lee, T. J.; Head-Gordon, M.; Rendell, A. P. *Chem. Phys. Lett.* **1995**, *243*, 402.
- [119] Froese, R. D. J.; Humbel, S.; Svensson, M.; Morokuma, K. *J. Phys. Chem. A* **1997**, *101*, 227.

- [120] Grimme, S. *J. Chem. Phys.* **2003**, *118*, 9095.
- [121] Halkier, A.; Helgaker, T.; Jørgensen, P.; Klopper, W.; Koch, H.; Olsen, J.; Wilson, A. K. *Chem. Phys. Lett.* **1998**, *286*, 243.
- [122] Halkier, A.; Helgaker, T.; Jørgensen, P.; Klopper, W.; Olsen, J. *Chem. Phys. Lett.* **1999**, *302*, 437.
- [123] Frisch, M. J.; Trucks, G. W.; Schlegel, H. B.; Scuseria, G. E.; Robb, M. A.; Cheeseman, J. R.; Scalmani, G.; Barone, V.; Mennucci, B.; Petersson, G. A.; Nakatsuji, H.; Caricato, M.; Li, X.; Hratchian, H. P.; Izmaylov, A. F.; Bloino, J.; Zheng, G.; Sonnenberg, J. L.; Hada, M.; Ehara, M.; Toyota, K.; Fukuda, R.; Hasegawa, J.; Ishida, M.; Nakajima, T.; Honda, Y.; Kitao, O.; Nakai, H.; Vreven, T.; Montgomery Jr., J. A.; Peralta, J. E.; Ogliaro, F.; Bearpark, M.; Heyd, J. J.; Brothers, E.; Kudin, K. N.; Staroverov, V. N.; Kobayashi, R.; Normand, J.; Raghavachari, K.; Rendell, A.; Burant, J. C.; Iyengar, S. S.; Tomasi, J.; Cossi, M.; Rega, N.; Millam, J. M.; Klene, M.; Knox, J. E.; Cross, J. B.; Bakken, V.; Adamo, C.; Jaramillo, J.; Gomperts, R.; Stratmann, R. E.; Yazyev, O.; Austin, A. J.; Cammi, R.; Pomelli, C.; Ochterski, J. W.; Martin, R. L.; Morokuma, K.; Zakrzewski, V. G.; Voth, G. A.; Salvador, P.; Dannenberg, J. J.; Dapprich, S.; Daniels, A. D.; Farkas, Ö.; Foresman, J. B.; Ortiz, J. V.; Cioslowski, J.; Fox, D. J. Gaussian-09 Revision C.01.
- [124] Werner, H.-J.; Knowles, P. J.; Knizia, G.; Manby, F. R.; Schütz, M.; Celani, P.; Györffy, W.; Kats, D.; Korona, T.; Lindh, R.; Mitrushenkov, A.; Rauhut, G.; Shamasundar, K. R.; Adler, T. B.; Amos, R. D.; Bernhardsson, A.; Berning, A.; Cooper, D. L.; Deegan, M. J. O.; Dobbyn, A. J.; Eckert, F.; Goll, E.; Hampel, C.; Hesselmann, A.; Hetzer, G.; Hrenar, T.; Jansen, G.; Köppl, C.; Liu, Y.; Lloyd, A. W.;

- Mata, R. A.; May, A. J.; McNicholas, S. J.; Meyer, W.; Mura, M. E.; Nicklass, A.; O'Neill, D. P.; Palmieri, P.; Peng, D.; Pflüger, K.; Pitzer, R.; Reiher, M.; Shiozaki, T.; Stoll, H.; Stone, A. J.; Tarroni, R.; Thorsteinsson, T.; Wang, M. MOLPRO 2012.1.
- [125] Aradi, B.; Hourahine, B.; Frauenheim, T. *J. Phys. Chem. A* **2007**, *111*, 5678.
- [126] Kubillus, M.; Gaus, M.; Jan, R.; Elstner, M. *J. Chem. Theory Comput.* **2015**, *11*, 332.
- [127] Jiang, D. E.; Sumpter, B. G.; Dai, S. *J. Chem. Phys.* **2007**, *126*, 134701/1.
- [128] Wang, Y.; Qian, H.-J.; Morokuma, K.; Irle, S. *J. Phys. Chem. A* **2012**, *116*, 7154.
- [129] Casolo, S.; Løvvik, O. M.; Martinazzo, R.; Tantardini, G. F. *J. Chem. Phys.* **2009**, *130*, 054704/1.
- [130] Paupitz, R.; Autreto, P. A. S.; Legoas, S. B.; Srinivasan, S. G.; van Duin, A. C. T.; Galvão, D. S. *Nanotechnology* **2013**, *24*, 035706/1.
- [131] Reed, A. E.; Curtiss, L. A.; Weinhold, F. *Chem. Rev.* **1988**, *88*, 899.
- [132] Lide, D. R. *CRC Handbook of Chemistry and Physics*, 84th ed.; CRC Press: Boca Raton, FL, 2003.
- [133] Zhang, Y.; Yang, W. *J. Chem. Phys.* **1998**, *109*, 2604.
- [134] Boese, A. D.; Martin, J. M. L. *J. Chem. Phys.* **2004**, *121*, 3405.
- [135] Johnson, E. R.; Salamone, M.; Bietti, M.; DiLabio, G. A. *J. Phys. Chem. A* **2013**, *117*, 947.
- [136] Schröder, D.; Loos, J.; Schwarz, H.; Thissen, R.; Preda, D. V.; Scott, L. T.; Caraiman, D.; Frach, M. V.; Böhme, D. K. *Helv. Chim. Acta* **2001**, *84*, 1625.
- [137] Blondel, C.; Cacciani, P.; Delsart, C.; Trainham, R. *Phys. Rev. A* **1989**, *40*, 3698.
- [138] Boys, S. F.; Bernardi, F. *Mol. Phys.* **1970**, *19*, 553.
- [139] Cohen, A. J.; Mori-Sánchez, P.; Yang, W. *Science* **2008**, *321*, 792.

- [140] Janak, J. F. *Phys. Rev. B* **1978**, *18*, 7165.
- [141] Perdew, J. P.; Parr, R. G.; Levy, M.; Balduz, J. L. *Phys. Rev. Lett.* **1982**, *49*, 1691.
- [142] Lundberg, M.; Nishimoto, Y.; Irle, S. *Int. J. Quantum Chem.* **2012**, *112*, 1701.
- [143] Petukhov, A. G.; Mazin, I. I.; Chioncel, L.; Lichtenstein, A. I. *Phys. Rev. B* **2003**, *67*, 153106.
- [144] Bodrog, Z.; Aradi, B.; Frauenheim, T. *J. Chem. Theory Comput.* **2011**, *7*, 2654.
- [145] Dreyer, D. R.; Park, S.; Bielawski, C. W.; Ruoff, R. S. *Chem. Soc. Rev.* **2010**, *39*, 228.
- [146] Wang, S.; Ang, P. K.; Wang, Z.; Tang, A. L. L.; Thong, J. T. L.; Loh, K. P. *Nano Lett.* **2010**, *10*, 92.
- [147] Becerril, H. A.; Mao, J.; Liu, Z.; Stoltenberg, R. M.; Bao, Z.; Chen, Y. *ACS Nano* **2008**, *2*, 463.
- [148] Matyba, P.; Yamaguchi, H.; Eda, G.; Chhowalla, M.; Edman, L.; Robinson, N. D. *ACS Nano* **2010**, *4*, 637.
- [149] Lu, Y.; Lo, S.; Lin, J.; Zhang, W.; Lu, J.; Liu, F.; Tseng, C.-M.; Lee, Y.-H.; Liang, C.-T.; Li, L.-J. *ACS Nano* **2013**, *7*, 6522.
- [150] Usachov, D.; Vilkov, O.; Grüneis, A.; Haberer, D.; Fedorov, A.; Adamchuk, V. K.; Preobrajenski, A. B.; Dudin, P.; Barinov, A.; Oehzelt, M.; Laubschat, C.; Vyalikh, D. *Nano Lett.* **2011**, *11*, 5401.
- [151] Wang, H.; Maiyalagan, T.; Wang, X. *ACS Catal.* **2012**, *2*, 781.
- [152] Stankovich, S.; Dikin, D. A.; Piner, R. D.; Kohlhaas, K. A.; Kleinhammes, A.; Jia, Y.; Wu, Y.; Nguyen, S. T.; Ruoff, R. S. *Carbon N. Y.* **2007**, *45*, 1558.
- [153] Hummers, W. S.; Offeman, R. E. *J. Am. Chem. Soc.* **1958**, *80*, 1339.
- [154] Schniepp, H. C.; Li, J. L.; McAllister, M. J.; Sai, H.; Herrera-Alonson, M.; Adamson,

- D. H.; Prud'homme, R. K.; Car, R.; Seville, D. A.; Aksay, I. A. *J. Phys. Chem. B* **2006**, *110*, 8535.
- [155] Szabo, T.; Berkesi, O.; Forgo, P.; Josepovits, K.; Sanakis, Y.; Petridis, D.; Dekany, I. *Chem. Mater.* **2006**, *18*, 2740.
- [156] Gao, W.; Alemany, L. B.; Ci, L.; Ajayan, P. M. *Nat. Chem.* **2009**, *1*, 403.
- [157] Li, X.; Wang, H.; Robinson, J. T.; Sanchez, H.; Diankov, G.; Dai, H. *J. Am. Chem. Soc.* **2009**, *131*, 15939.
- [158] Barinov, A.; Malciog, O. B.; Fabris, S.; Gregoratti, L.; Dalmiglio, M.; Kiskinova, M.; Baris, O.; Sun, T. *J. Phys. Chem. C* **2009**, *113*, 9009.
- [159] Nourbakhsh, A.; Cantoro, M.; Klekachev, A. V.; Pourtois, G.; Vosch, T.; Hofkens, J.; van der Veen, M. H.; Heyns, M. M.; De Gendt, S.; Sels, B. F. *J. Phys. Chem. C* **2011**, *115*, 16619.
- [160] Amirhasan, N.; Cantoro, M.; Vosch, T.; Pourtois, G.; Clemente, F.; van der Veen, M. H.; Hofkens, J.; Heyns, M. M.; De Gendt, S.; F, S. B. *Nanotechnology* **2010**, *21*, 435203.
- [161] Hossain, M. Z.; Johns, J. E.; Bevan, K. H.; Karmel, H. J.; Liang, Y. T.; Yoshimoto, S.; Mukai, K.; Koitaya, T.; Yoshinobu, J.; Kawai, M.; Lear, A. M.; Kesmodel, L. L.; Tait, S. L.; Hersam, M. C. *Nat. Chem.* **2012**, *4*, 305.
- [162] Vinogradov, N. a.; Schulte, K.; Ng, M. L.; Mikkelsen, A.; Lundgren, E.; Martensson, N.; Preobrajenski, A. B. *J. Phys. Chem. C* **2011**, *115*, 9568.
- [163] Goverapet Srinivasan, S.; van Duin, A. C. T. *J. Phys. Chem. A* **2011**, *115*, 13269.
- [164] Paci, J. T.; Upadhyaya, H. P.; Zhang, J.; Schatz, G. C.; Minton, T. K. *J. Phys. Chem. A* **2009**, *113*, 4677.

- [165] Morón, V.; Martin-Gondre, L.; Crespos, C.; Larregaray, P.; Gamallo, P.; Sayós, R. *Comput. Theor. Chem.* **2012**, *990*, 132.
- [166] Isborn, C. M.; Li, X.; Tully, J. C. *J. Chem. Phys.* **2007**, *126*, 134307.
- [167] Rani, B.; Dharamvir, K. *Int. J. Quantum Chem.* **2014**, *114*, 1619.
- [168] Ma, Y.; Foster, A. S.; Krasheninnikov, A. V.; Nieminen, R. M. *Phys. Rev. B - Condens. Matter Mater. Phys.* **2005**, *72*, 1.
- [169] Tachikawa, H.; Iyama, T.; Kawabata, H. *Jpn. J. Appl. Phys.* **2013**, *52*.
- [170] Fu, B.; Han, Y.; Bowman, J. M.; Leonori, F.; Balucani, N. *J. Chem. Phys.* **2012**, *137*, 22A532.
- [171] Fu, B.; Han, Y.-C.; Bowman, J. M.; Angelucci, L.; Balucani, N.; Leonori, F.; Casavecchia, P. *Proc. Natl. Acad. Sci.* **2012**, *109*, 9733.
- [172] Hu, W.; Lendvay, G.; Maiti, B.; Schatz, G. C. *J. Phys. Chem. A* **2008**, *112*, 2093.
- [173] Paris, A.; Verbitskiy, N.; Nefedov, A.; Wang, Y.; Fedorov, A.; Haberer, D.; Oehzelt, M.; Petaccia, L.; Usachov, D.; Vyalikh, D.; Sachdev, H.; Wöll, C.; Knupfer, M.; Büchner, B.; Calliari, L.; Yashina, L.; Irle, S.; Grüneis, A. *Adv. Funct. Mater.* **2013**, *23*, 1628.
- [174] Blöchl, P. E. *Phys. Rev. B* **1994**, *50*, 17953.
- [175] Gaus, M.; Chou, C. P.; Witek, H.; Elstner, M. *J. Phys. Chem. A* **2009**, *113*, 11866.
- [176] Xia, H.; Duclos, S.; Ruoff, A.; Vohra, Y. *Phys. Rev. Lett.* **1990**, *64*, 204.
- [177] Zhao, Y.; Zhang, J.; Pantea, C.; Qian, J.; Daemen, L. L.; Rigg, P. A.; Hixson, R. S.; Gray, G. T.; Yang, Y.; Wang, L.; Wang, Y.; Uchida, T. *Phys. Rev. B - Condens. Matter Mater. Phys.* **2005**, *71*, 1.
- [178] Zhang, J.; Zhao, Y.; Pantea, C.; Qian, J.; Daemen, L. L.; Rigg, P. A.; Hixson, R. S.;

- Greeff, C. W.; Gray, G. T.; Yang, Y.; Wang, L.; Wang, Y.; Uchida, T. *J. Phys. Chem. Solids* **2005**, *66*, 1213.
- [179] Kresse, G.; Hafner, J. *Phys. Rev. B* **1993**, *47*, 558.
- [180] Kresse, G.; Hafner, J. *Phys. Rev. B* **1994**, *49*, 14251.
- [181] Kresse, G.; Furthmüller, J. *Comput. Mater. Sci.* **1996**, *6*, 15.
- [182] Kresse, G.; Furthmüller, J. *Phys. Rev. B* **1996**, *54*, 11169.
- [183] Pack, J. D.; Monkhorst, H. J. *Phys. Rev. B* **1977**, *16*, 1748.
- [184] DFTB+ www.dftb-plus.info.
- [185] Francis, G. P.; Payne, M. C. *J. Phys. Condens. Matter* **1990**, *2*, 4395.
- [186] Birch, F. *Phys. Rev.* **1947**, *71*, 809.
- [187] Zhang, S.; Zhu, Y.; Zhang, X.; Zhang, S.; Qi, L.; Liu, R. *Comput. Mater. Sci.* **2010**, *50*, 179.
- [188] Hao, Y.-J.; Zhang, L.; Chen, X. R.; Li, Y.-H.; He, H.-L. *J. Phys. Condens. Matter* **2008**, *20*, 235230.
- [189] Greeff, C. W. *Model. Simul. Mater. Sci. Eng.* **2005**, *13*, 1015.
- [190] Olinger, B.; Jamieson, J. C. *High Temp. - High Press.* **1973**, *5*, 123.
- [191] Schimka, L.; Gaudoin, R.; Klimeš, J.; Marsman, M.; Kresse, G. *Phys. Rev. B - Condens. Matter Mater. Phys.* **2013**, *87*, 1.
- [192] Kittel, C. *Introduction to Solid State Physics*, 8th ed.
- [193] Jomard, G.; Magaud, L.; Pasturel, A. *Philos. Mag. B* **1998**, *77*, 67.
- [194] Aguayo, A.; Murrieta, G.; de Coss, R. *Phys. Rev. B* **2002**, *65*, 092106.
- [195] Vaidya, S. N.; Kennedy, G. C. *J. Phys. Chem. Solids* **1972**, *33*, 1377.
- [196] Heiming, A.; Petry, W.; Trampenau, J.; Alba, M.; Herzig, C.; Schober, H. R.; Vogl, G.

- Phys. Rev. B* **1991**, *43*, 10948.
- [197] Hao, Y.-J. Y.; Zhang, L.; Chen, X. X.-R.; Cai, L. L.-C.; Wu, Q.; Alfe, D.; Alfè, D.
Phys. Rev. B **2008**, *78*, 2.
- [198] Bodrog, Z. Improvements to the Density-Functional Tight-Binding method: new, efficient parametrization schemes and prospects of a more precise self-consistency.
Ph.D. thesis, Universität Bremen, 2012, Vol. PhD Thesis.
- [199] Hutama, A. S.; Aradi, B.; Chou, C.-P.; Witek, H. A.; Frauenheim, T.; Fisher, C. A. J.; Irle, S. *AMTC Lett.* **2016**, *5*.

Appendix

A Zr electronic parameters

1. Confining potential parameters

The orbital and density confining potential parameters used in this thesis is listed in Table A.1. They were reoptimized from Nishimura's electronic parameter shown in his thesis.¹

Table A.1 Confining potential parameters for Zr

	Orbital			Density		
	W	a	r_0	W	a	r_0
Zr	1.352	46.749	3.895	0.000	49.847	49.059

2. Spin coupling constant for Zr

The $W_{ll'}$ for spin-polarized atomic calculations was computed using Bremen version of atomic code ONECENT under zeroth-order regular approximation (ZORA)² and PBE scheme. The $W_{ll'}$ is shown in Table A.2.

Table A.2 Spin coupling constant for Zr.

$W_{ll'}$	s	p	d
s	-0.0115	-0.010	-0.006
p	-0.010	-0.014	-0.003
d	-0.006	-0.003	-0.0105

¹ Nishimura, Y. *Nagoya Univ. 2013, PhD Thesis.*

² van Lenthe, E.; Ehlers, A.; Baerends, E. *J. Chem. Phys.* **1999**, *110*, 8943.

3. Bulk Zr band structures

Band structures of bulk Zr presented below were calculated using the optimized geometry from PBE-PAW level of theory. This is to show that the fitting of electronic parameters from band structure using the PSO based automated DFTB parameter tool will yield a perfect fitness (<0.001) between the reference band structure especially for the low lying states while the transferability to other phases are remarkably acceptable. The computational details are similar as in the works presented in Chapter 5.

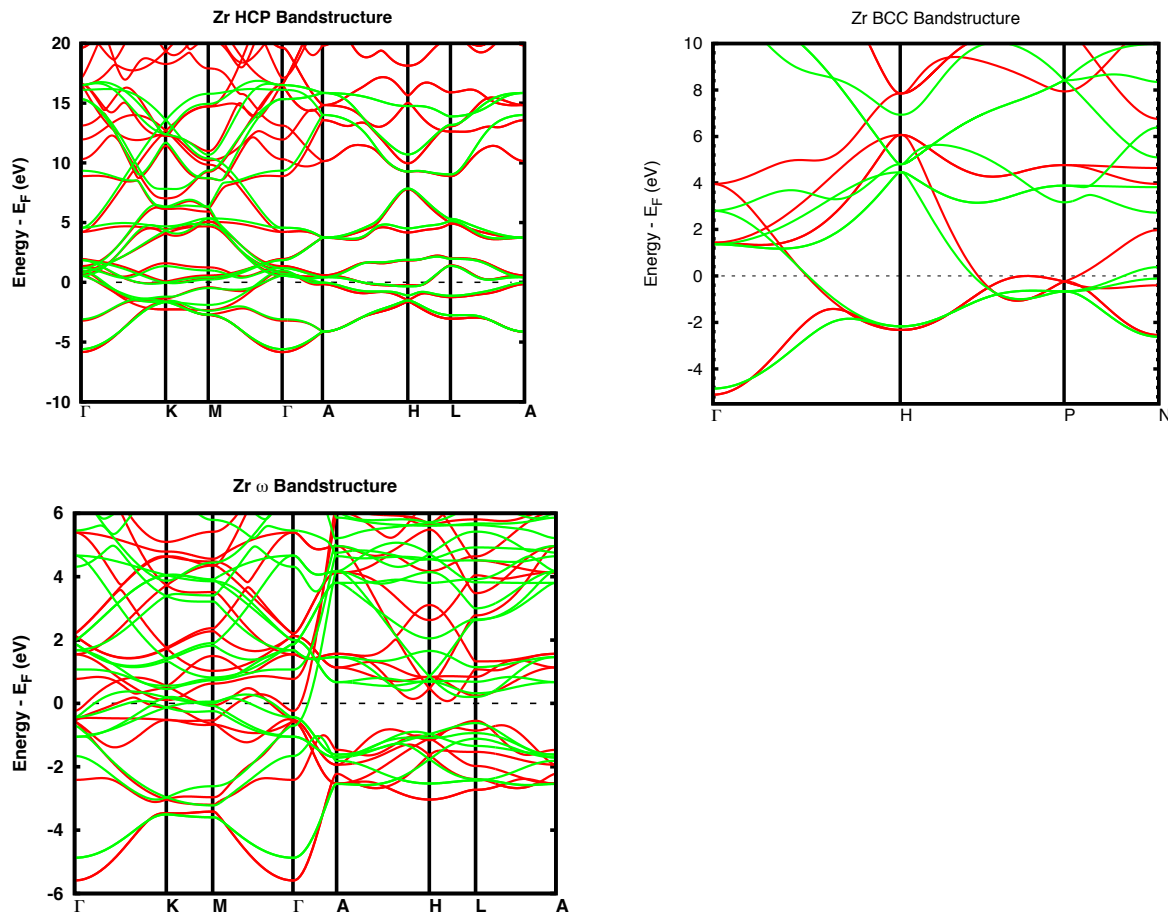


Figure A.1 Band structures of all bulk phases of Zr considered in this work. Red curves represent the PBE-PAW band structure and green curves represent the DFTB2 band structure. Band energies are shifted with respect to Fermi energy (E_F).

Acknowledgements

I am extremely grateful to my supervisor, Prof. Stephan Irle, for his continuing support, guidance and patience during my study at Nagoya University.

Most of the results presented in this thesis may not be available without the contributions from my collaborators. I would like to acknowledge Prof. Thomas Frauenheim and Dr. Balint Aradi from Bremen Centre for Computational Material Science, Universität Bremen who firstly introduced the details and techniques for DFTB parameterizations. I also acknowledge Prof. Henryk Witek and Dr. Chien-pin Chou from National Chiao Tung University, Taiwan for providing the automatic DFTB parameters code and Dr. Yoshifumi Nishimura for providing the electronic parameters. I acknowledged Dr. Craig Fisher from Japan Fine Ceramic Centre, Nagoya for introducing the SOFCs project, an interesting, yet extremely challenging project, and for the comments, suggestions and discussions along the projects.

I would also like to thank the Quantum Chemistry Group members, Assoc. Prof. Daisuke Yokogawa, Assist. Prof. Yuh Hijikata, Dr. Yoshio Nishimoto, Dr. Kosuke Usui, Dr. Arifin, Hayashi-san, Quan, Ka-Hung, Asri, former and current postdocs, students and visitors for making the Quantum Chemistry Group in Nagoya University a more interesting place.

I am greatly indebted to Lembaga Pengelolaan Dana Pendidikan (Endowment Fund for Education), Ministry of Finance Republic of Indonesia who supports financially my graduate study.

Final word, I would like to thank my entire family for the countless supports.

List of Publications

Chapter 3

Hutama, A. S.; Hijikata, Y.; Irle, S. “Coupled Cluster and Density Functional Studies of Atomic Fluorine Chemisorption on Coronene as Model Systems for Graphene Fluorination”, *J. Phys. Chem. C* **2017**, *121*, 14888.

Chapter 4

Hutama, A. S.; Hijikata, Y.; Irle, S. “Density Functional Studies of Atomic Oxygen and Nitrogen Interactions with Coronene as Model Systems for Graphene Functionalizations”, *in preparation*.

Chapter 5

Hutama, A. S.; Aradi, B.; Chou, C-P.; Witek, H.A.; Nishimura, Y.; Fisher, C. A. J.; Frauenheim, Th.; Irle, S. ”Density-Functional Tight-Binding Repulsive Potentials for Zr – Zr Interactions in Solid State Systems”, *in preparation*.